12-2017

Electrochemical Hydrogen Separation via the Solid Acid Electrolyte Cesium Dihydrogen Phosphate

David Leon Wilson
University of Tennessee, Knoxville, dwilso34@vols.utk.edu

To the Graduate Council:

I am submitting herewith a dissertation written by David Leon Wilson entitled "Electrochemical Hydrogen Separation via the Solid Acid Electrolyte Cesium Dihydrogen Phosphate." I have examined the final electronic copy of this dissertation for form and content and recommend that it be accepted in partial fulfillment of the requirements for the degree of Doctor of Philosophy, with a major in Chemical Engineering.

Thomas A. Zawodzinski, Major Professor

We have read this dissertation and recommend its acceptance:

Robert M. Counce, John Z. Guo, Gerd Duscher

Accepted for the Council:
Carolyn R. Hodges

Vice Provost and Dean of the Graduate School

(Original signatures are on file with official student records.)

Electrochemical Hydrogen Separation via the Solid Acid Electrolyte Cesium Dihydrogen Phosphate

A Dissertation Presented for the
Doctor of Philosophy
Degree
The University of Tennessee, Knoxville

David Leon Wilson III
December 2017

ACKNOWLEDGEMENTS

I would first like to thank Dr. Thomas Zawodzinski for providing me with such a great opportunity to work in this research group. I would also like to thank Dr. Alex Papandrew for his knowledge and help throughout my first four years in graduate school. The example that was set by Dr. Papandrew has really helped me grow and mature as a researcher and as a person. Words cannot express my gratitude to Dr. Papandrew for all of the time and energy invested into my advancement as a scientist. I would like to thank my committee members, Dr. Robert Counce, Dr. Gerd Duscher, and Dr. Jon Guo for their suggestions and advice on my research. I would also like to thank Dr. Ramez Elgammal for his significant guidance in the last year of my graduate career. Dr. Gabriel Goenaga has been a great influence as well and has helped me throughout my career at the University of Tennessee. I also would like to thank the TN-SCORE program of the National Science Foundation for their financial support of this work (EPS-1004083). I would not be here without the support of my fellow graduate students and our research group. I would also not be the man I am today without the love and support of my parents, David and Teresa Wilson, and my sisters, Beth and Jennifer.

ABSTRACT

Abundant, inexpensive, high purity molecular hydrogen as a medium for energy distribution is potentially enabling for adoption of alternative electricity generation schemes. Steam reforming of natural gas remains the dominant method of producing large amounts of hydrogen. However, this process also creates by-products, most notably, carbon monoxide and carbon dioxide. Separation to ultra-high purity hydrogen from these syngas reformate streams by traditional methods, such as pressure swing absorption, has its disadvantages including long cycle times, contamination and a large equipment footprint. Alternative methods of hydrogen separation, such as electrochemical pumping, are a viable alternative to this separation dilemma due to their relative simplicity and potential efficiency.

The solid-state proton conductor cesium dihydrogen phosphate has shown potential in electrochemical hydrogen separation devices operating on reformed hydrocarbons. In this work, we have synthesized a suite of nanoparticles, including Pt, Pd, Ru, Ni and Cu, supported on carbon for implementation in solid acid electrodes. We evaluate these materials at an intermediate temperature of 250 degrees Celsius for the hydrogen oxidation and reduction reaction, as well the electrooxidation of carbon monoxide. Functionally graded anodes are fabricated to balance CO conversion activity with hydrogen oxidation. These re-engineered anodes are implemented in conjunction with Ni-

based cathodes to demonstrate efficient hydrogen separation using ultra low loadings of Pt from syngas-like inputs.

PREFACE

My advisor, Dr. Zawodzinski, who has his background in electrochemistry has had a major influence on this dissertation. As a result, the terminology and nomenclature found within this work may be native to one in that field.

TABLE OF CONTENTS

LIST OF TABLES

LIST OF FIGURES

CHAPTER 1

INTRODUCTION

Hydrogen Production

To generate H_2, various methods are explored depending on the molecular precursor from which hydrogen is to be extracted. While there are many methods of hydrogen production, a few of note are biological, direct solar water splitting, electrolysis, and thermochemical. Biological processes are numerous but the most common are microbial biomass conversion and photobiological. These processes, while at the early stages, offer a potential sustainable, low-carbon hydrogen production method. However, their output is modest at best. Direct solar water splitting processes and water electrolysis use water and energy to split water into hydrogen and oxygen. Direct solar water splitting uses light as an energy source using semiconductor materials in a photoelectrochemical process[1]. Water electrolysis uses electricity as an energy source to split water into hydrogen and oxygen. Water electrolysis remains very energy intensive in its current iteration[2–6]. Though these methods offer a "green" option since they are low in carbon emissions or even carbon free, the current state of the technologies and their economics keep them from being widely applied in the hydrogen production field.

Thermochemical processes are the most prominent means of present day hydrogen production. The most common techniques are solar thermochemical hydrogen, biomass gasification, coal gasification and partial oxidation of oil and natural gas reformation (or steam methane reformation). The cleanest and most sustainable of the thermochemical processes is solar thermochemical hydrogen

production or solar water thermolysis. This involves the decomposition of water normally over cerium oxide catalysts at temperatures of over 2000K[1,7]. However, most thermochemical processes uses other chemical precursors. H_2S has been used in order to produce hydrogen and sulfur at temperatures ranging from 1030K to 1600K[8–10]. Other hydrogen rich precursors have been used including NH_3BH_3 as a molecular precursor to H_2[11].

Biomass, coal, oil and natural gas all use carbon-based precursors, creating CO and CO_2 as by-products during their respective decomposition reactions. Biomass consists of a variety of renewable organics including crops such as switchgrass or crop residue used to produce hydrogen. One drawback to biomass is the complexity and variety of the composition of the input material. Gaseous products normally include H_2, CH_4, CO, CO_2, and various others depending on the biomass. The CO can then be combined with water in the water-gas shift reaction (WGS) in order to increase the efficiency[12–14] Biomass is still in early development and is not a widely used hydrogen production method. Fossil based hydrocarbons presently offer the most inexpensive means of molecular hydrogen production. According to the Department of Energy, as of 2009, 96% of the world's hydrogen was produced from various thermochemical processes. Of these 48% is derived from steam reforming of methane, 30% is derived from partial oxidation of oil and 18% is derived from coal gasification. Partial oxidation of oil occurs via the oxidation of more "traditional" petroleum fossil fuels under less than one to one stoichiometric conditions. This allows

substantial hydrogen to be released from the hydrocarbons, but due to the lack of oxygen, cannot fully combust to create water. This hydrogen can then be separated and used for other purposes.

Coal gasification is a technique used to produce a variety of products including syngas by the reaction seen below:

$$\mathrm{CH_{0.8}} + \mathrm{H_2O} + O_2 \rightarrow CO_2 + \mathrm{CO} + \mathrm{H_2} + \mathrm{impurities} \quad (1\text{-}1)$$

After the separation of impurities, the stream mixture is called synthesis gas and can be further processed into hydrogen-rich liquid fuels and chemical or the hydrogen produced directly from the process can be used.

Steam reforming of natural gas is the dominant method of hydrogen production[15]. A recent increase in the availability of natural gas[16] in the United States has presented increased economic opportunities for conversion of methane and methane-derived molecules to hydrogen. Methane conversion to hydrogen fuel is described by the chemical reactions: Initial reforming reaction:

$$\mathrm{CH_4} + \mathrm{H_2O} \rightarrow \mathrm{CO} + 3\mathrm{H_2} \quad (1\text{-}2)$$

Water-gas shift reaction (WGS):

$$\mathrm{CO} + \mathrm{H_2O} \rightarrow \mathrm{CO_2} + \mathrm{H_2} \quad (1\text{-}3)$$

Steam-methane reforming (SMR):

$$\mathrm{CH_4} + 2\mathrm{H_2O} \rightarrow \mathrm{CO_2} + 4\mathrm{H_2} \quad (1\text{-}4)$$

Methane can also be converted to liquid methanol to increase its transportability and hydrogen fuel density. Methanol can then be reformed as needed to hydrogen via the reactions below:

$$CH_3OH + H_2O \rightarrow CO_2 + 3H_2 \quad (1\text{-}5)$$

$$CH_3OH \rightarrow CO + 2H_2 \quad (1\text{-}6)$$

Steam reforming of methane and its derivatives produces byproducts, including, CO and CO_2 which must be removed in order to purify to hydrogen fuel.

Hydrogen Separation

Presently, hydrogen fuel can be separated from via three major processes: pressure swing adsorption, fractional cryogenic distillation or membrane separation. Pressure swing adsorption and fractional cryogenic distillation are the two most popular commercially available methods[17]. Separation to ultra-high purity hydrogen from these reformate streams by these two traditional methods has its disadvantages. These include long cycle times, contamination and a large equipment footprint[18]. Membrane based separation hold advantages over these methods due to low energy consumption, scalable investment cost, and system effectiveness. The most common membrane based hydrogen separation is based on metallic membranes such as Pd[19] or Pd-alloy[20–22]. Diffusion through these membranes is based on the concentration gradient and can be described by Fick's first law of diffusion. However, mechanically

stability, expense, and slow rates of diffusion have limited their effectiveness in large scale applications.

An alternative to diffusion-based membrane separation is electrochemical separation. Electrochemical hydrogen separation devices are advantageous relative to diffusion based membranes because of their shorter response time for the increase or decrease in demand for hydrogen, more efficient use of precious metals, and potential applications for simultaneous electrochemical compression. Unlike diffusion based membranes, the hydrogen is oxidized and transported as protons through the membrane to a counter electrode at which the protons are reduced to evolve pure hydrogen gas. Multiple proton-conducting electrolytes have been proposed for this application, including perfluorinated sulfonic acid (PFSA) polymers operating at low temperatures (~80 °C)[2,23], Phosphoric acid and phosphoric acid-doped polybenzidazole (PBI) at intermediate temperatures (~180 °C)[24,25], and proton-conducting oxide membranes at higher temperatures (>500 °C)[26].

An intermediate temperature range (150°C to 300°C) is uniquely favorable, due to the increased resistance of hydrogen oxidation catalysts (typically platinum) to poisoning in this temperature range,[27–30] a thermal match to the optimal methanol reforming temperature of 240-260°C,[31] and the ability to use a conventional low-cost materials set for stack and system components that is obviated at higher temperatures. A relatively new proton conducting material

exists in this advantageous temperature range known as cesium dihydrogen phosphate.

Cesium Dihydrogen Phosphate as an Electrochemical Membrane

Multiple electrolytes have been proposed for this task including perfluorinated sulfonic acid membranes (PFSA) for low temperatures, phosphoric acid and phosphoric acid-doped polybenzidazole (PBI) for intermediate temperatures, and proton-conducting oxide membranes at higher temperatures. The intermediate temperature range (150°C to 300°C) offers the best range of hydrogen separation from methanol reformate due to the optimal methanol reformation temperature of 240-260 °C[32]. A graph of proton conductivities of electrolytes function at low to intermediate temperature is shown in Figure 1-1.

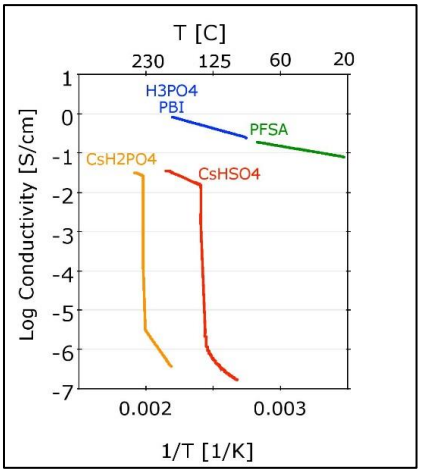

Figure 1-1 Various proton conducting membrane materials from room temperature to intermediate temperatures.

The solid-state proton conductor cesium dihydrogen phosphate (CsH_2PO_4 or CDP) has shown potential in electrochemical devices operating on fuels such as reformed natural gas or methanol. CDP undergoes a solid-solid phase transition at 228 °C and an associated increase in proton conductivity of more than three orders of magnitude (8.5×10^{-5} S cm^{-1} at 223 °C to 2.5×10^{-2} S cm^{-1} at 250 °C)[33]. This "super protonic" phase's stability is subject to the partial pressure of water[34,35]. The application of CDP in fuel cells has been a major interest since their developmental inception. These systems have been shown to tolerate reformate streams in H_2-air cells containing CO, H_2S, NH_3, CH_3OH, C_3H_8 and CH_4 of 20%, 100ppm, 100 ppm, 5%, 3% and 5% respectively, retaining 90-95% of pure H_2 performance[36]. Solid acid fuel cells operated using methanol and an integrated steam reformer have also shown similar results. They have also showed encouraging results when operating on alcohol fuels[37].

In addition to showing promise as intermediate temperature fuel cells, recent investigations have shown promise in the application of hydrogen separation and compression[38]. However, these earlier studies were performed using simulated reformate feeds and typically used Pt as the hydrogen evolution and oxidation catalyst. However, in one study, a Ni catalyst was used as a hydrogen evolution catalyst to replace Pt on the cathode[39]. In another study Ru was used as an oxidation catalyst under simulated reformate[36]. Previous work using methanol as a fuel in solid acid fuel cells (SAFCs) has shown that an

integrated reformer with proper heat management would prove advantageous to efficient system operation over two separate processes[37].

Hydrogen Separation Electrocatalysts

The majority of relevant electrocatalysts today utilize materials designed to be used as nanoscale particle coatings. With reactions occurring on the surface of the catalysts, this approach maximizes the real surface area for a given volume or geometric surface area. This leads to a higher catalytic utilization which leads to a reduction of costs. For some relatively abundant metals like Ni and Fe the cost reduction may seem unwarranted, but considering that most highly active electrocatalysts are composed of expensive and rare metals including Pt, Ru and Pd, this optimization must be achieved for large scale production. The price of Pt, Pd and Ru prices can be seen in Figure 1-2.

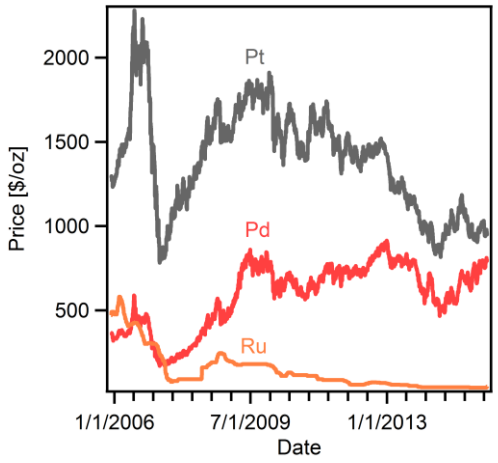

Figure 1-2 Metal prices of Pt/Pd/Ru since 2006

The leading choice for this process are structures referred to as supported catalysts. These involve an electron conducting support on which the catalyst nanoparticles will be placed. These nanoparticles are normally hemispherical in shape.

For the CDP based hydrogen separation electrocatalyst, a novel chemical vapor deposition (CVD) method is used to create nanoparticles on various supports using metal acetylacetonate. The most common technique is to flow the precursor vapor over a substrate that is at a higher temperature than the incoming vapor. However, we have selected to use a packed, mixed bed technique that allows for a much simpler design, but inhibits temperature controllability. While the exact mechanism in our current setup is still unknown, we will turn to the literature for insight on the nanoparticle formation. The CVD process can be summarized by two different mechanism for particle synthesis. These are known as nucleation and growth. Based off the rate of these two processes, the particle size can vary greatly. For nucleation, three steps will be considered based on a stable gas-phase precursor molecule. In the first step we consider the molecule physisorbs to the surface. The second step involves chemisorption. The third step is reaction to the metal atom on the surface. For the growth case, we consider two different processes. One is autocatalytic of properties, thus allowing for a direct reaction with another precursor molecule. The other is surface migration to form larger metal particles. These two mechanisms are effected by three main reaction variables: Gas phase, solid

phase, and temperature. For the gas phase, this includes the precursor vapor as well as any other gas selected to potentially aid in the reaction. The solid phase includes the support structure, including any physisorbtion from a supporting reaction vapor. For the temperature, this includes the ramp rate, as well as final temperature. While generalities exist for any procedure, each metal acac is a separate case.

We will first consider the case that yields the most consistent results, which involves using Pt acetylacetonate ($Pt(acac)_2$) to form Pt nanoparticles. $Pt(acac)_2$ has been used as a precursor for many different reaction schemes to make Pt nanoparticles[40–43]. We will consider each of the parameters (temperature, gas and solid) in order to determine the potential effects on nucleation and growth. For vapor decomposition, $Pt(acac)_2$ has been reported to thermalize around 510K[44]. However this is variable due to the gas phase and solid phase interactions as well. Higher temperatures lead to considerable carbon impurities of up to 50mass%C[45]. Slow temperature ramp rates (5°C/min) from room temperature to 210°C have shown to give the best results for small, uniform nanoparticles[46].

The gas phase interacts with the precursor vapor by either reacting with the precursor in the vapor phase, or by modifying the surface coverage of the solid phase. For $Pt(acac)_2$, hydrogen, oxygen, nitrogen, and water have been investigated. Hydrogen lowers the activation energy, but also increases the amount of carbon impurity[47,48]. Oxygen decreases the amount of carbon impurity

by reacting with the residual carbon[48]. Water lowers the activation energy slightly from oxygen[47] and with proper temperature control reduces the carbon impurity to 1% for nanoparticles[49]. The surface of the support is also effected by the gas phase. One notable example is the autocatalytic effect of the atmosphere for Pt deposited is hydrogen[42] or an inert gas like nitrogen or argon[50]. Hydrogen leads to larger grain sizes compared to the inert atmosphere.

For our deposition of Pt, we decided to use a N_2/H_2O atmosphere at a ratio of 0.3/0.4 bar respectively, with a ramp rate of 5°C and a final temperature of 210°C. For the reaction, it has been suggested that the first step is $Pt(acac)_2$ physisorbtion to the surface. Next chemisorption will proceed by ligand exchange with surface hydroxyls. This then leaves an acacH, a protonated acac and a Pt-O bond. The loss of the second acac proceeds rapidly yielding a Pt^{II} oxo-type intermediate species. The reduction step to Pt^0 occurs via a two-electron process with the oxidation of the acacH[46]. We suggest the water aids in decreasing the activation energy as shown in other cases[47] as well as potentially assisting in limiting Pt diffusion, giving a higher density of nucleation and a smaller average crystallite size.

The CVD technique implemented in CDP catalyst synthesis does not involve expensive instrumentation normally required of the process[41,51]. The deposition is support sensitive and the same method can be used to create conformal coatings[46] as well as nanotubes[52]. Bimetallic and alloyed nanotubes can also be formed using the same technique for various catalytic reactions[53–57].

Although these techniques have been applied to the optimization of oxygen reduction reaction and alkaline electrochemical reactions, very little effort has been placed into the hydrogen oxidation reaction and the hydrogen evolution reaction for hydrogen separation systems.

Cell Fabrication

In order to fabricate a cell, electrode mixtures must be synthesized for the membrane-electrode assembly. The composite electrocatalyst powders were synthesized by dry-grinding the fine CDP with the various metal/carbon catalyst and naphthalene (a fugitive binder). These mixtures kept the mass ratio of CDP, naphthalene and carbon to 3: 1: 0.4 (mass) allowing for variation of the electrode catalyst mass without modifying the electrode thickness. Hydrogen pump membrane-electrode assemblies (MEAs) were then fabricated using these electrocatalysts by lamination of active layers in a 2.85 cm^2 diameter hardened steel die. Stainless steel mesh was used for current collector and PTFE tape for a sealant. Each MEA had a membrane thickness of approximately 75 to 85 microns. The mass of a given electrode varied between 22 to 28 mg dependent on the metal loading on the carbon support. In each cell, the hydrogen evolution electrode was laminated at 125 MPa while the hydrogen oxidation electrode was laminated at 25 MPa. The cell assembly was installed in a stainless steel fixture for testing. The overall cell summary is observable in Figure 1-3.

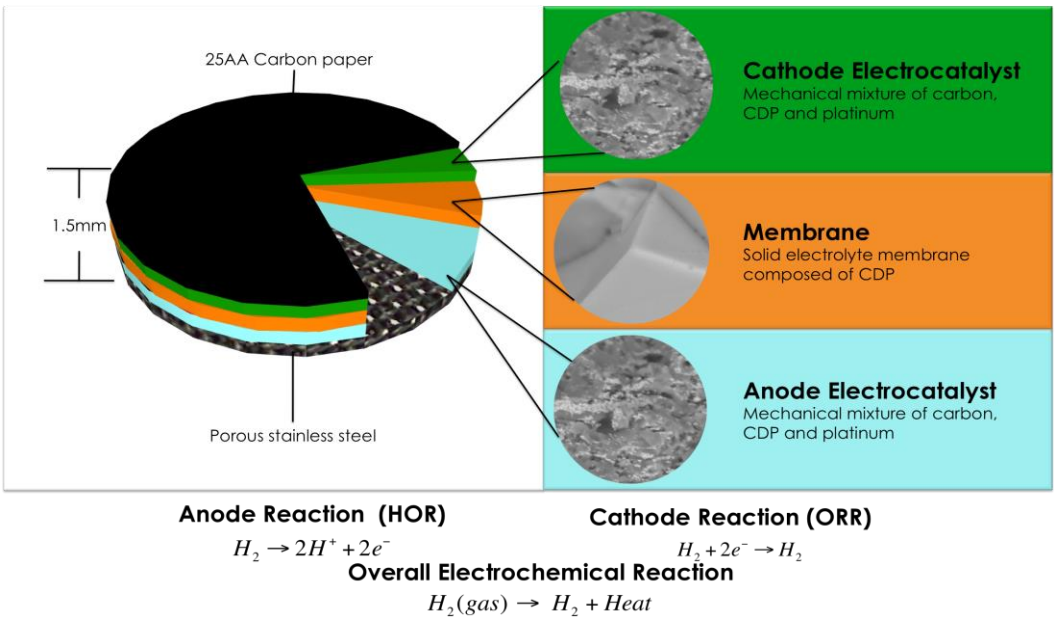

Figure 1-3 Cell summary for solid acid hydrogen separation devices

At testing temperatures, a humidified gas stream (approximately 0.35 bar) must be supplied in order to stabilize the CDP and inhibit the dehydration reaction[58].

In Situ Electrochemical Techniques

In order for an electrochemical reaction to take place, there are several necessary components: anode and cathode, electrolyte, and external connection between electrodes. The anode and cathode are where the electrochemical reactions occur. Oxidation results in the loss of electrons from the electroactive material and occurs at the anode. A reduction reaction consumes electrons and occurs at the cathode. In the case of an electrochemical H_2/H_2 hydrogen pump, the reactions are described below:

$$\text{Anode: } H_2 \rightarrow 2H^+ + 2e^- \quad (1\text{-}7)$$

$$\text{Cathode: } 2H^+ + 2e^- \rightarrow H_2 \quad (1\text{-}8)$$

The main function of the electrolyte is to conduct ions from one electrode to the other. Electrolytes also have to be electrically insulating to properly separate the electrical charge and ensure that the electrons flow through the external circuit.

A properly designed electrochemical cell will have a measureable open-circuit cell potential described in volts. Ideally, this voltage is described by the Nernst potential and is a function of both temperature and pressure. The Nernst potential is described below:

$$E = E^o - \frac{RT}{nF} \ln\left[\frac{C_{Ox}}{C_{Red}}\right] \quad (1\text{-}9)$$

Where E is the cell potential, E° is the standard cell potential (zero in the case of hydrogen), R is the universal gas constant, T is the temperature in Kelvin, n is the number of moles of electron transferred, and C is the chemical concentration. For a gas system, this concentration is described in partial pressures of the active species. For a standard H_2/H_2 hydrogen pump with equal pressures, the Nernst potential is zero. However, when operating using fuel or fuel reformate this potential will change based on the partial pressures of the hydrogen in each electrode.

When deviating from the open-circuit potential, a current will begin to flow. Normalizing the current response to geometric area and measuring at multiple cell potentials will describe a cell voltage-current relationship commonly referred

to as a polarization curve. We adopt this as a primary figure of merit for the devices that are the subject of this thesis. A polarization curve for a solid acid CDP based, Pt/Pt, H_2/H_2 cell operating at 250°C can be seen below in Figure 1-4.

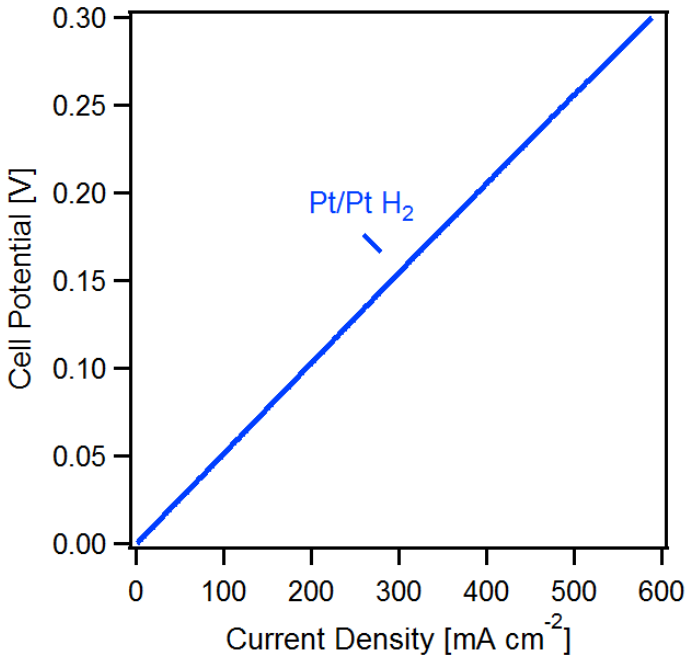

Figure 1-4 Symmetric hydrogen polarization curve at 250 °C with 75 °C dew point.

A simple equation to define the cell potential as a departure from ideal voltage is described below:

$$E_{cell} = E°(T,P) - \eta_{a,a} - |\eta_{a,c}| - \eta_r - \eta_{m,a} - |\eta_{m,c}| - \eta_x \qquad (1\text{-}10)$$

Where E_{cell} is the cell potential, E°(T,P) is the theoretical equilibrium open-circuit potential of the cell calculated from the Nernst potential. The activation overpotentials at the anode and cathode are represented by $\eta_{a,a}$ and $\eta_{a,c}$ respectively. Crossover losses are represented by η_x. Ohmic polarization is represented by η_r. concentration losses are represented by $\eta_{m,a}$ and $\eta_{m,c}$ for anode and cathode respectively. These inefficiencies lead to the generation of heat at a rate defined by:

$$P_H = P_{H,rev} + P_{H,irr} \tag{1-11}$$

Where P_H is the "waste" heat power density, $P_{H,rev}$ is the reversible heat generation and $P_{H,irr}$ is the irreversible heat generation. The reversible heat generation is described below:

$$P_{H,rev} = -i\frac{T\Delta S}{nF} \tag{1-12}$$

Where i is the current density, T is the temperature in Kelvin, n is the number of moles of electrons transferred and S is the entropy of reaction. This entropic term is commonly referred to as the Peltier heating. The irreversible heat generation is defined below:

$$P_{H,irr} = i\left(\eta_{a,a} + |\eta_{a,c}| + \eta_r + \eta_{m,a} + |\eta_{m,c}| + \eta_x\right) \tag{1-13}$$

Where i is the current density, the activation overpotentials at the anode and cathode are represented by $\eta_{a,a}$ and $\eta_{a,c}$ respectively, crossover and other losses are represented by η_x, ohmic polarization is represented by η_r, and concentration losses are represented by $\eta_{m,a}$ and $\eta_{m,c}$ for anode and cathode respectively. In order to better understand electrochemical hydrogen separation

systems, a more detailed look into these overpotentials are required. One extremely advantageous method for analysis of electrochemical systems is impedance spectroscopy.

Electrochemical impedance spectroscopy (EIS) is a technique commonly used for delineating some polarizations. This technique involves the application of an alternating-current (AC) signal of varying frequencies over the electrochemical reaction interface. This causes the electrode-electrolyte to oscillate with the same applied frequency. EIS data can be utilized to gain a wealth of information on the ohmic, charge transfer, and mass transfer resistances by using equivalent circuit or a first-principles-based modeling approach. The electric field of EIS is described below:

$$\mathrm{E(t)} = \mathrm{E_0} + \mathrm{e^{j\omega t}} \tag{1-14}$$

Where E(t) is the AC electric field at any time t, ω is the angular frequency, with amplitude $\mathrm{E_0}$. The term j is used to represent the square root of negative one. The current response is defined by:

$$\mathrm{I(t)} = \mathrm{I_0} + \mathrm{e^{j(\omega t+\phi)}} \tag{1-15}$$

Where I(t) is the current at any time t, $\mathrm{I_0}$is the current amplitude, ω is the angular frequency and ϕ is the phase shift. By applying these to Ohm's law

$$\mathrm{E(t)} = \mathrm{I(t)} * \mathrm{Z} \tag{1-16}$$

A new term Z is defined as the complex impedance characteristics. This impedance term has two different components.

$$\mathrm{Z} = \mathrm{Z'} + \mathrm{jZ''} \tag{1-17}$$

Where Z' represents the real component and Z'' represents the imaginary component. Using EIS, the overpotentials described in (1-10) can begin to be described using equivalent circuits elements. These elements must be selected intelligently to best describe the physical nature of the processes they represent. Term by term representation of the equivalent circuit models will be described below.

Activation Losses

The activation overpotentials at the electrodes represented by $\eta_{a,a}$ and $\eta_{a,c}$ physically represent the voltage loss required to initiate the reaction. Between the electrode and the electrolyte there exists a structure referred to as the electrical double layer. At the electrode and the electrolyte surface there is an accumulation of charge. This accumulation of charge is only broken when the voltage exceeds the difference required to drive the charge transfer, thus leading to the electrochemical reaction. This discontinuity of charge physically leads to capacitor like effects. For equivalent circuit analysis, an electrode can be modeled as a resistance-capacitance (RC) circuit where the resistance and capacitator are in parallel.

Real material EIS spectra rarely display perfect RC circuit behavior. In order to better represent the electrode in circuit models, a new circuit element, the constant phase element, is introduced to replace the capacitor. The constant phase element is defined below:

$$Z_{CPE} = \frac{1}{Q(j\omega)^a} \quad (1\text{-}18)$$

Where Q has units of capacitance, ω is the angular frequency, and a varies between 0 and 1. When a is equal to 0, the CPE reduces to a pure resistor and when a is equal to 1, the CPE displays an ideal capacitator response. This is represented in Figure 1-5.

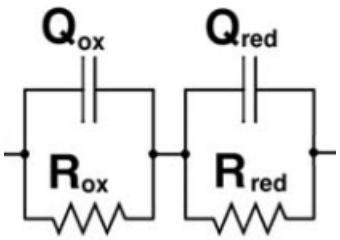

Figure 1-5 Circuit model for electrodes in solid acids

Where Q represents the CPE and R represents the charge transfer resistance. The subscripts “ox” and “red” represents the oxidation and reduction electrodes respectively.

Polarization Kinetic Losses

In order to determine the kinetic polarization losses, a model must be used to evaluate the electrodes. A general expression derived to express the kinetic activation potential of a given electrode is the Butler-Volmer (BV) model. The BV describes an electrochemical model that is limited by the charge transfer of the electron as the rate determining step. Other models are required to describe

systems with another limiting step or reactions that compete in parallel. The BV model for both electrodes is defined below:

$$i = i_o\left[e^{a_a F\eta/RT} - e^{-a_c F\eta/RT}\right] \quad (1\text{-}19)$$

Where i is the current, i_o is the exchange current, a_a and a_c are the anodic and cathodic transfer coefficients, respectively, η is the overpotential, R is the universal gas constant and T is the Kelvin temperature. In the case of a rate-limiting electron transfer step for the HOR/HER, (1-19) is equivalent to:

$$i = i_o\left[e^{\beta F\eta/RT} - e^{-(1-\beta)F\eta/RT}\right] \quad (1\text{-}20)$$

Where the transfer coefficients have been replaced by the symmetry factor, β, which for a completely symmetric activation barrier takes a value of 0.5. By varying i_o and β as free parameters, a least-squares fitting can be used to fit polarization curves. When the effective anodic transfer coefficient approaches zero, the low field approximation can be used as described in equation (1-21).

$$i = i_o * \frac{\eta F}{RT} \quad (1\text{-}21)$$

Where, i is the current i_o is the exchange current density η is the over potential, F is the Faraday's constant, R is the universal gas constant and T is the temperature in Kelvin. However, a very educated upper and lower bound must be made to normalize the exchange current density. Determining the exact tri-phase boundary for solid acid environments remain an open problem but estimates can be made based between the physical surface area and the electrochemical surface area (ECSA) found in aqueous electrochemical tests[38].

Ohmic Losses

The next major losses are the internal ohmic losses represented by η_r. This behavior is linear and can be defined by the summation of all contact and ionic resistances. The ohmic polarization is represented as

$$\eta_r = I\left(\sum_{k=1}^{n} r_k\right) \quad (1\text{-}22)$$

Where I is the current, r_k is the resistance of individual cell components. Using EIS, the total ohmic resistance ($\sum_{k=1}^{n} r_k$) is represented by the high-frequency resistance (HFR), which is defined as the intercept with the real axis in the high-frequency region of the impedance arc. This is represented by the circuit element in Figure 1-6.

Figure 1-6 Circuit model for ohmic resistance in solid acid devices

The ionic resistance of the electrolyte represents the majority of the ohmic resistance. The resistance is also a function of the geometry of the conducting material. In order to describe the intrinsic property of a material, the resistivity shall be used. The resistivity is related to the resistance through the cross-sectional area and the linear path of ionic travel. The conductivity, the inverse of the resistivity, is another common term to describe the effectiveness of ion

transport. The conductivity also represents the intrinsic property of a material. For solid acid CDP systems, only the super-protonic phase is desirable for operations. This region can be seen in Figure 1-7. The conductivity in this region is dependent on the temperature of operation and follow an Arrhenius relationship.

$$\sigma = A_o e^{-\left(\frac{E_a}{kT}\right)} \tag{1-23}$$

Where E_a is the activation energy, k is the Boltzmann constant, and T is the Kelvin temperature.

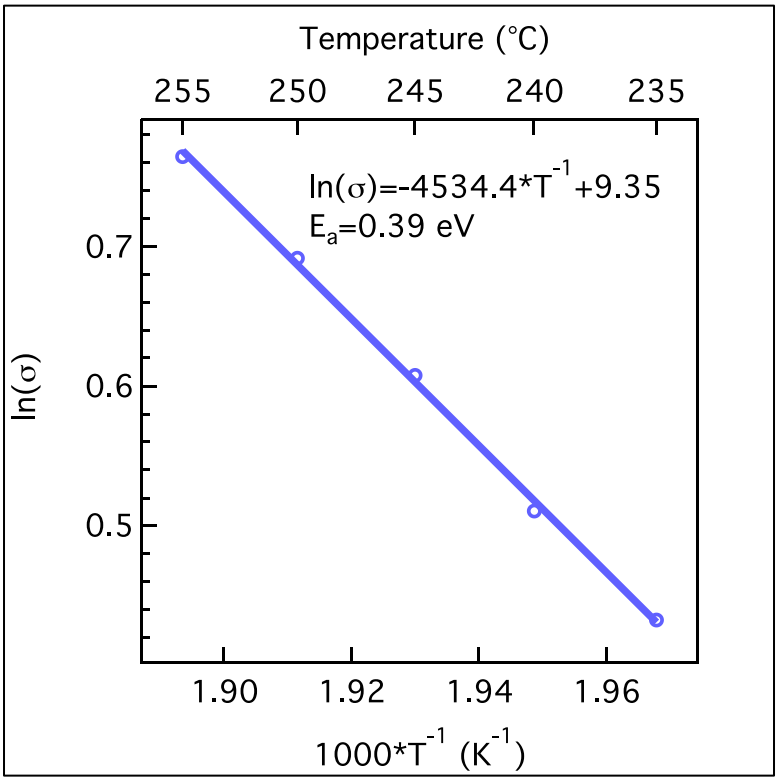

Figure 1-7 Measured proton conductivity of cesium dihydrogen phosphate

This relationship, with an understanding the geometry of the cell, can be used to make further analysis of the system, such as temperature changes based on a conductivity difference.

Polarization Mass Transport Losses

During electrochemical reactions, a reduction in the reactant surface concentration reduces the thermodynamic voltage from the Nernst equation and the exchange current density from the BV equation. Restriction of the rate of transport within the porous electrode can occur for a variety of reasons including gas-phase diffusion limitation, accumulation of inert species, and surface blockage by poisoning. The diffusion of hydrogen is rapid, but in very dilute streams containing other species, mass transport of hydrogen to the electrode becomes an issue. This gas-phase diffusion limitation and the accumulation of inert species can be modeled in EIS analysis by introducing a new circuit element called the finite-length Warburg diffusion element. The complex impedance represented by the Warburg element is described below:

$$Z = \frac{R_d \tanh\left(\sqrt{j\omega\tau}\right)}{\left(\sqrt{j\omega\tau}\right)} \qquad (1\text{-}24)$$

Where R_d is a resistance and τ is a time constant. Catalyst surface blockage by poisoning has to be represented using a different model. In order to model this, a modification of the BV relationship can be made in order to describe the more complex phenomena of catalyst blocking. Natural gas derivatives, such as syngas, contain impurities including CO and H_2S. For the particular case of CO

adsorption, a new function θ can be introduce to help describe this phenomenon. This function is based on the relative CO coverage of the electrocatalyst. A first-order case of (1-θ) is derived for room-temperature systems which assumes negligible CO desorption. This seems unlikely for the elevated temperatures of 250 °C in which CDP based electrolytes operate and, indeed, electrochemical peaks for CO oxidation are not observed in these systems. A second-order case $(1-\theta)^2$ assumes two adjacent Pt sites are required for hydrogen adsorption, which may not be justified if hydrogen dissociative adsorption is not rate limiting step. This modification to the BV equation is seen below:

$$i = (1-\theta)^n i_o \left[e^{\beta F \eta / RT} - e^{-(1-\beta) F \eta / RT} \right] \quad (1\text{-}25)$$

Where:

$$(1-\theta)^n = \frac{R_{I,H_2}}{R_{X,H_2}} \quad (1\text{-}26)$$

Where R_{I,H_2} represents the charge transfer resistance for the HOR in an anode feed diluted with an inert species and R_{X,H_2} is the same concentration with the inert replaced with CO. The n represents the mode of CO absorption. For low-overpotentials, an approximation can be used to simplify calculations:

$$i = (1-\theta)^n i_o \frac{\eta F}{RT} \quad (1\text{-}27)$$

Other Polarization Losses

The polarization losses represented by the chemical crossover and electrical shorts can be modeled as well, however a properly designed system will minimize these losses to almost negligible values. Due to our experimental

setup, another equivalent circuit element must be added to account for the inductance generated. Inductance is of highest influence at very high frequencies in the EIS spectra and is a result of the stainless steel test fixture. This is represented in the circuit by the diagram below:

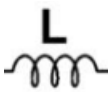

Figure 1-8 Induction parameter for modeling the stainless steel test fixture in solid acid devices

By combining all these elements an equivalent circuit is modeled to represent the solid acid hydrogen separation system. For systems with 100% H_2 concentration

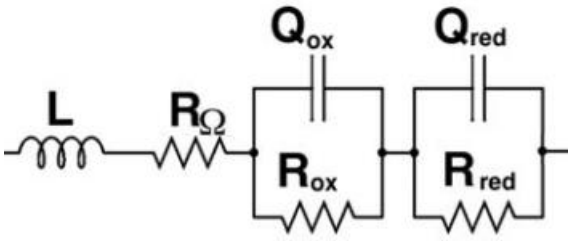

Figure 1-9 Solid acid circuit model for hydrogen separation devices

For systems with diffused hydrogen input, like our reformate streams the Warburg element is added:

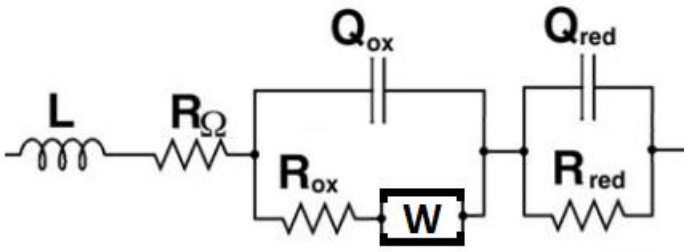

Figure 1-10 Solid acid circuit model for hydrogen separation devices with mass limitations in one electrode

These circuit models are used in order to model EIS spectra in solid acid systems.

X-ray Diffraction

X-ray diffraction is an essential technique for analyzing long-range order of crystalline solids. The analysis of XRD is described by the Bragg equation (1-28).

$$n\lambda = 2d\sin\theta \qquad (1\text{-}28)$$

Where λ is the wavelength of the x-ray, θ is the angle between the incident ray and the surface of the crystal, and d is the spacing between the layers of atoms. When the incident rays that make the Bragg angles are only slightly different from theta, we find that destructive interference is not complete. This leads to an increasing of the width of a diffraction peak with the decreasing of the crystal size. The exact treatment of this yields the Scherrer formula.

$$t = \frac{0.9\lambda}{B\cos\theta} \quad (1\text{-}29)$$

Where t is the particle size of very small crystals, λ is the wavelength of the x-ray, and B is the full width half maximum of a diffraction peak.

Gas Chromatography-Mass Spectrometry (GCMS)

Gas chromatography-mass spectrometry is an essential technique for measuring composition of gases as well as volatile liquids. As hinted by the name, there are two components: the gas chromatographer and the mass spectrometer. The gas chromatograph utilizes a capillary column as well as various chemical phases in order to increase or decrease the retention time of various molecules. The mass spectrometers job is to capture, ionize, accelerate, deflect and detect the ionized molecules. This is achieved by breaking each molecule into ionized fragments and analyzing the mass-to-charge ratio. The number counts detected based off the mass-to-charge ration can then be used to determine the gas stream composition.

Transient Plane Source

The transient plane source method is a useful technique for determining the thermal conductivities of solids. In its most general form, two similar pellets are placed on either side of a sensor. Then a thermal pulse is generated and the temperature response is measured. This measured temperature is then fit to an equation based off the shape factor of the sensor and the sample. For our case, the equation of fit is shown in equation (1-30)

$$T(\tau) = \frac{P}{r\lambda\pi^{\frac{3}{2}}} D(\tau) \tag{1-30}$$

Where P is the power per unit, r is the radius of the sensor, λ is the thermal conductivity, $D(\tau)$ is the shape function.

CHAPTER 2

SUPPORTED CATALYST FOR SOLID ACID ELECTROCHEMICAL HYDROGEN SEPARATION

Abstract

The solid-state proton conductor cesium dihydrogen phosphate (CsH2PO4 or CDP) has shown potential in electrochemical devices operating on fuels such as reformed NG or methanol. CDP undergoes a solid-solid phase transition at 228 °C and an associated increase in proton conductivity of more than three orders of magnitude (8.5 x 10-5 S cm^{-1} at 223 °C to 2.5 x 10-2 S cm^{-1} at 250 °C). These systems have been shown to tolerate reformate streams in H_2-air cells containing CO, H_2S, NH_3, CH_3OH, C_3H_8 and CH_4 of 20%, 100ppm, 100 ppm, 5%, 3% and 5% respectively, retaining 90-95% of pure H2 performance[58]. Solid acid fuel cells operated using methanol and an integrated steam reformer have also shown similar results[37]. Recently, we showed that this material can also be used in an electrochemical hydrogen separation system using similar reformate streams[36]. In the majority of these earlier studies, platinum was used as the catalyst for both the hydrogen reduction and oxidation reactions. We have also demonstrated that unsupported nickel is an effective hydrogen evolution catalyst in solid acid hydrogen pump devices[39]. Here, we have synthesized a suite of carbon-supported catalysts (Pt, Pd, Ru, Ni and Cu) for implementation in electrodes. We evaluate these materials as hydrogen oxidation and evolution catalysts in CDP-based devices.

Introduction

The efficiency and cost of hydrogen oxidation catalyst are of paramount importance to any potential hydrogen economy. Typically in fuel cells, the HOR reaction can be practically ignored. This is true for solid acid fuel cell systems where the charge transfer resistance for a Pt/Pt hydrogen/air cell is 2.2 Ω cm^2 and for the hydrogen oxidation reaction is 0.05 Ω cm^2. Platinum based catalyst are the most effective and stable catalyst for the hydrogen oxidation catalyst (HOR) and the hydrogen evolution reaction (HER) for acidic environments. However, due to the rarity and expense of Pt, other catalyst must be investigated to determine an effective substitute. The first step we will take will be examining the reaction mechanism.

The intrinsic kinetic rate of the hydrogen reaction, known as the exchange current density, i_o is defined as the rate at which the reaction proceeds at equilibrium. The mechanism for the HOR reaction on Pt in acidic environments is usually assumed to proceed by adsorption of molecular hydrogen, followed by dissociation, and finally a fast charge-transfer step.

$$H_2 \rightarrow 2H_{ad} \tag{2-1}$$

$$H_2 \rightarrow H^+ + H_{ad} + e^- \tag{2-2}$$

$$H_{ad} \rightarrow H^+ + e^- \tag{2-3}$$

These equations are referred to as the Tafel (2-1), Heyrovsky (2-2) and the Volmer (2-3).

While various studies have been performed on the HOR and HER reaction in low temperature aqueous environments[59–62] and phosphoric acid[25], very limited studies have been performed on solid acid systems. The presence of the electrolyte can have a major effect on the effects on the reactions. This is most notable for Ru based catalyst which are poor performance in low temperature acidic environments for HOR[63]. Hydrogen evolution reactions catalysis has also been studied in great detail for various catalyst including Ni, Cu, Ru, Pd and Pt[64]. However, as with the case of the HOR reaction, there have been very limited studies on non-aqueous environments.

A new class of proton conductor, cesium dihydrogen phosphate (CDP) allows for an effective hydrogen separation system at temperature ranges of 230-250°C. CDP based cells have already been implemented as a fuel cell on anode streams containing as much as 20% CO and as a hydrogen separation system on simulated reformate containing as much as 10% CO[36].

In this contribution, we investigate multiple catalyst for hydrogen separation including Pt, Pd, Ru, Cu, Ni, NiCu and RuNi electrodes for both HOR and HER reactions. Chemical vapor deposition was used to synthesize the catalyst on Vulcan XC72 carbon support. We normalized the performance to Pt electrodes for both the HOR and HER reaction due to the stability in solid acid systems. While the effective electrochemical surface area (ECSA) for solid acids is still an open problem, we bound our minimum surface area to the electrolyte

surface area of 2 m^2/g and by measured ECSA found in the Pt aqueous acid 45 m^2/g in order to compare to other literature cases[65].

Experimental Methods

CsH_2PO_4 was synthesized by reaction of $CsCO_3$ (Alfa Aesar, 99%) with H_3PO_4 (Alfa Aesar, 85%) followed by precipitation in methanol and drying. The as-synthesized CDP was low-energy ball-milled to reduce its initial particle size, yielding a fine particulate powder with a BET surface area of approximately 2 m^2/g. Carbon-supported metallic nanoparticles were synthesized as hydrogen oxidation and evolution catalysts. Platinum, Palladium, ruthenium, and nickel nanoparticles were deposited onto Vulcan XC-72R via a vapor-phase decomposition from their respective metal acetylacetonates $Pt(acac)_2$ (Strem Chemical), $Ru(acac)_3$ (Sigma-Aldrich), $Cu(acac)_2$ (Sigma-Aldrich), $Pd(acac)_2$ (Strem-chemical) and $Ni(acac)_2$ (Alfa Aesar). These reactions were carried out using a fixed bed wherein the crystalline solid precursors were mechanically mixed with the Vulcan XC-72R carbon, in a N_2-water vapor atmosphere at elevated temperatures via a method that we have demonstrated previously[36,46,52,56,66,67]. The ultimate deposition temperature varied for each species deposited, from 170°C (palladium), 210 °C (platinum) and 240 °C (ruthenium, nickel, and copper). The carbon-supported nickel and copper samples was further heat treated at 500°C under N_2 for 3 hours in flowing N_2.All

catalysts were characterized with using X-ray diffraction (XRD) (Philips X'Pert, l ¼ 0.1541874 nm). The position and width of diffraction peaks were obtained by fitting to Voight functions using IGOR Pro (Wavemetrics, Inc.). Ru catalysts were further analyzed by transmission electron microscopy (Zeiss Libra 200MC).

Composite electrocatalyst powders were synthesized by dry-grinding the fine CDP with the various metal/carbon catalyst and naphthalene (a fugitive binder). These mixtures kept the mass ratio of CDP, naphthalene and carbon to 3: 1: 0.4 (mass) allowing for variation of the electrode catalyst mass without modifying the electrode thickness. Hydrogen pump membrane-electrode assemblies (MEAs) were then fabricated using these electrocatalysts by lamination of active layers in a 2.85 cm^2 diameter hardened steel die. Stainless steel mesh was used for current collector and PTFE tape for a sealant. Each MEA had a membrane thickness of approximately 75 to 85 microns. The mass of a given electrode varied between 22 to 28 mg dependent on the metal loading on the carbon support. In each cell, the hydrogen evolution electrode was laminated at 125 MPa while the hydrogen oxidation electrode was laminated at 25 MPa. The cell assembly was installed in a stainless steel fixture for testing.

Prior to electrochemical testing, the cell assembly was heated to 150 °C in dry Ar. Both electrodes were then switched to a wet Ar purge at 75 °C dew point and heated to the testing temperature of 250 °C.

Electrochemical testing was conducted at 250 °C. At the start of the experiment, each electrode was supplied 30 sccm of humidified ultrahigh purity

hydrogen at a 75 °C dew point. Polarization curves were recorded at 1 hour intervals with a Bio-Logic VSP potentiostat by scanning the working electrode potential at 5 mV s^{-1} from the open circuit voltage (OCV) to -0.3 V then to 0.3 V of overpotential. Potentiostatic electrochemical impedance spectroscopy (PEIS) spectra were also recorded at -50 mV versus OCV in a frequency range from 200 kHz to 200 mHz with a single sine perturbation amplitude of 10 mV. Polarization curves free of the ohmic losses due to membrane resistance were derived by the subtraction of the current multiplied by the high frequency resistance measured at OCV. Cells were held at -50 mV for 1 hour between testing cycles.

Imaging of electrodes and chemical analysis was conducted with a Hitachi TM3000 SEM equipped with a Bruker Quantax EDS system operating at 15 kV.

Results and Discussion

Electrocatalysts are essential components for the solid acid hydrogen separation device and are separated into two electrodes separated by the membrane. For the hydrogen oxidation and evolution reaction, Pt and Pt alloys are generally considered to be the most active. Platinum itself is a rare and expensive metal, which hinders wide scale use for electrocatalysts. Various techniques have been implemented in order to maintain performance while reducing the amount of Pt used in electrodes. One of the most implemented tactics is reducing the particle size of the active catalyst to nanoparticles.

Nanostructured materials have an increased surface area to volume ratio which inherently increases the activity per mass. These nanoparticles are normally supported on a network of electron-conduction support, like carbon, which further increases the utilization of the catalysts. We have chosen to adopt this technique in order to fabricate high efficiency electrodes for the solid acid hydrogen separation system. Carbon-supported Pt nanoparticles were synthesized as hydrogen oxidation and evolution catalysts. Platinum nanoparticles were deposited onto Vulcan XC-72R via a vapor-phase decomposition from its respective metal acetylacetonate, $Pt(acac)_2$ These reactions were carried out using a fixed bed wherein the crystalline solid precursors were mechanically mixed with the Vulcan XC-72R carbon, in a N_2-water vapor atmosphere at elevated temperatures via a method that we have demonstrated previously[52,56,68]. The ultimate deposition temperature was 210 °C.

In order to evaluate the effectiveness of our deposition procedure, various characterization techniques were implemented. X-ray diffraction is one essential technique for analyzing long-range order of crystalline solids. The analysis of XRD is described by the Bragg equation described in (1-28).

When the incident rays that make the Bragg angles are only slightly different from theta, we find that destructive interference is not complete. This leads to an increasing of the width of a diffraction peak with the decreasing of the crystal size. The exact treatment of this yields the Scherrer formula (1-29). Cu Kα X-ray diffraction patterns for as-synthesized carbon-supported Pt are shown

in Figure 2-1. A mean particle size was computed using the Scherrer equation (1-29) and is found to be 3.3nm. This is in agreement with Pt nanoparticles synthesized using similar methods. We find for the Pt/C lattice parameter of 0.3916nm. This is in reasonable range of the tabulated value of 0.3923nm.

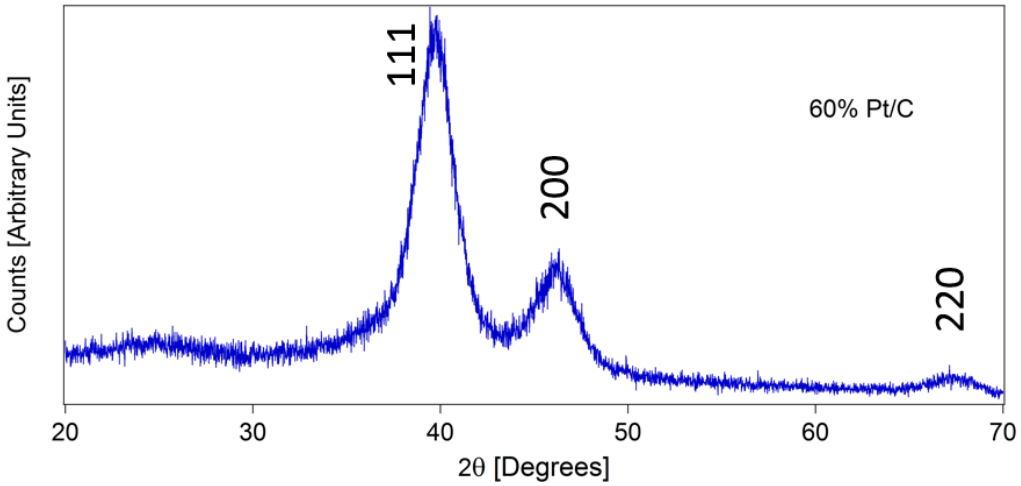

Figure 2-1 XRD pattern for vapor-grown 60% Pt/XC72

While platinum on carbon (Pt/C) is an efficient catalyst and electron carrier, an ion conducting network for protons must be created in order provide for the electrochemical reaction. In order to achieve this, the solid acid CDP was mixed in with the supported catalyst and a fugitive binder. This electrode mixture is then laminated on either side of the membrane. Figure 2-2 shows an SEM micrograph of an electrode formed using the supported catalysts with a total metal loading of 1.05 $mg_{Pt}cm^{-2}$. The CDP membrane can be seen at the top of

the screen while the voids in the electrode are due to the fugitive naphthalene which is used a binder. Figure 2-2b shows a higher magnification of the same electrode. The large 1 um CDP particles can be seen mixed with the carbon supported catalysts and does not display optimal mixing and dispersion.

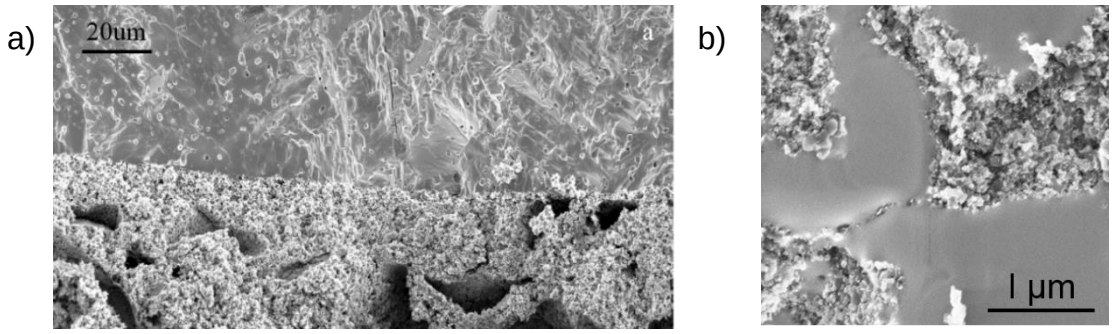

Figure 2-2 SEM micrographs of Pt/Pt electrodes post test

These cells are than loaded into a stainless steel test fixture and brought up under dry inert gases (either N_2 or Ar) to 150°C. At this temperature, the gases are humidified to around 0.35 bar (75°C dew point) in order to inhibit the CDP dehydration reaction as reported by the phase diagram[35]. At 250°C, these humidified purge gases are turned to H_2 in order to begin electrochemical hydrogen pumping. The first diagnostic test is electrochemical impedance spectroscopy performed at OCV. In order to normalize our results, these resistance values were multiplied by the geometric measured area that is exposed to membrane. A symmetric 1.05 mg/cm^2 (per electrode) Pt/Pt impedance arc is shown in Figure 2-3 at 250°C under a hydrogen anode and

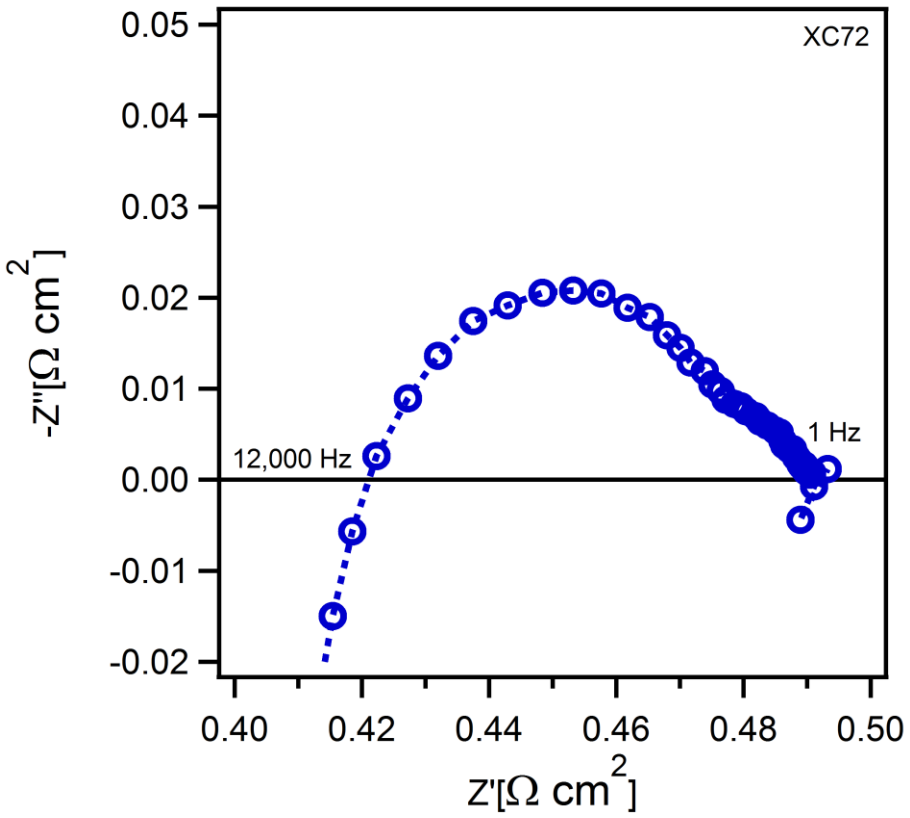

Figure 2-3 EIS spectra collected at OCV in hydrogen for Pt/Pt

hydrogen cathode feed at 75°C dew point. This dew point is required in order to maintain stable proton conduction at 250°C[35].

Due to the slight fabrication difference, there is always slight variation in the cell performance, notably the high frequency resistance (HFR). This is the resistance at the intercept of the higher frequency (in this case around 12,000 Hz) and accounts mostly for the membrane resistance, although all DC ohmic resistances are included in this measured value. By taking advantage of Ohm's law, we can multiply the measured HFR by the current in order to examine an IR-free system. The effect of the ohmic losses are most notable in Figure 2-4.

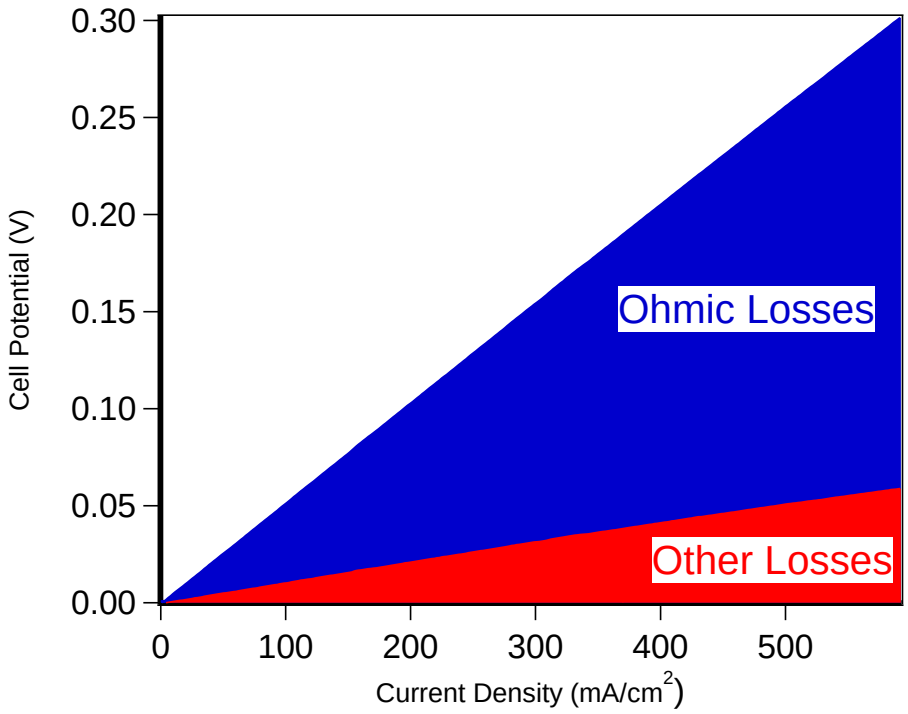

Figure 2-4 Polarization curves in hydrogen at 250 °C for Pt/Pt

The as-recorded and iR-free polarization curves for the Pt-Pt MEA acquired in pure H_2 at 250 °C are shown in Figure 2-5. The curves are symmetric and the dominant loss channel is ohmic, accounting for around 80% of the total losses in the cell. The majority of this resistance comes from the membrane. Relatively thick membranes are currently used in solid acid hydrogen pumps for consistency. These membrane have been shown to be reduced to 40 microns, but due to the large amount heat developed can lead to degradation. This will be discussed more in chapter 5.

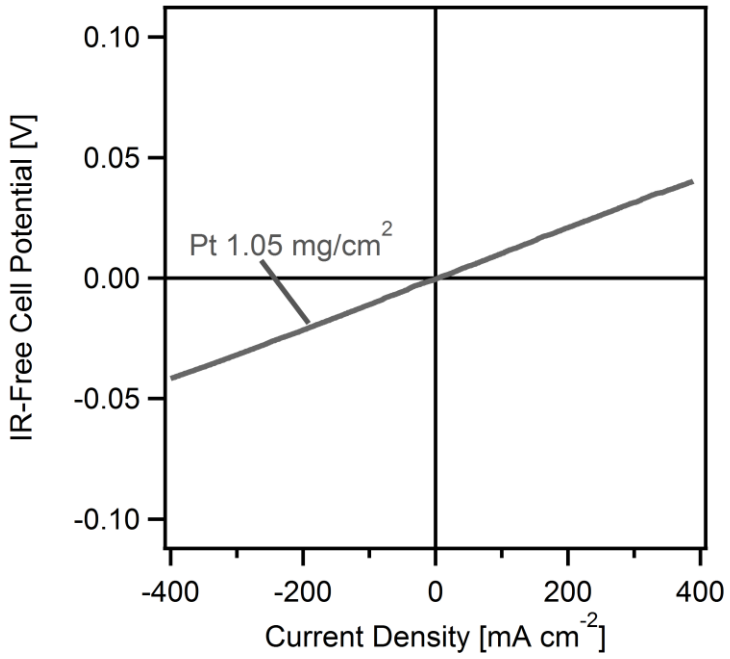

Figure 2-5 iR-free polarization curves acquired in hydrogen at 250 °C with 1.05mg/cm² electrodes for Pt/Pt

Figure 2-6 shows Tafel representations of iR-free polarization curves. Using the iR-free polarization curves at temperatures at 250 °C, we applied the Butler-Volmer equation (1-20). Allowing for i_o and ß to vary as free parameters, we applied a non-linear fitting to find the best fits for the polarization curves. A value of 0.49 was found for ß and a geometric exchange current density found was 452 mA/cm^2.

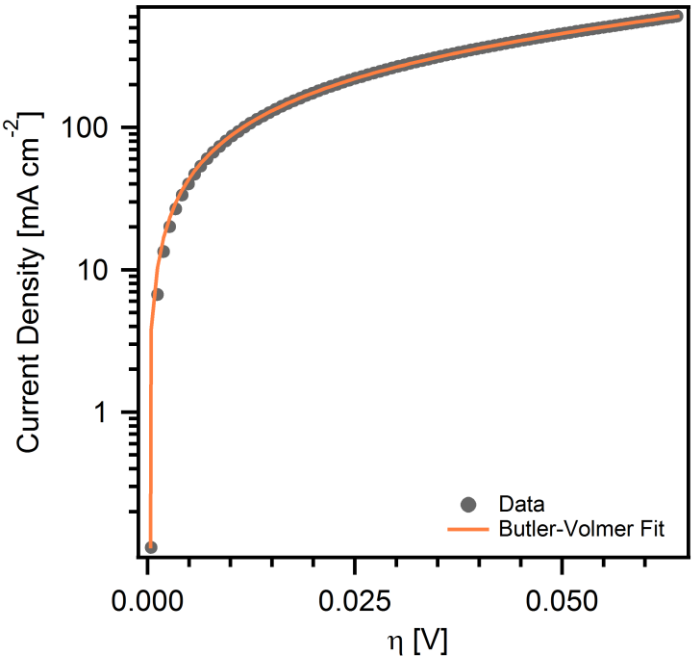

Figure 2-6 Tafel representation acquired in hydrogen at 250 °C with 1.05mg/cm² electrodes for Pt/Pt

While the geometric surface area is an effective parameter in for evaluation, it only normalizes by the 2d face of the electrode. Examining the

microstructure of the electrode membrane interface in higher magnification, Figure 2-7, we see that the electrode structure extends in the third dimension. Thus we must determine a more accurate way to measure the Pt active area of the electrode. This is commonly referred to as the electrochemical surface area (ECSA) and denotes the total area of the reaction. Unfortunately, the effective electrochemical surface area (ECSA) for solid acids is still an open problem. This does not limit us completely however, and we will bind our surface area by considering the maximum and minimum cases.

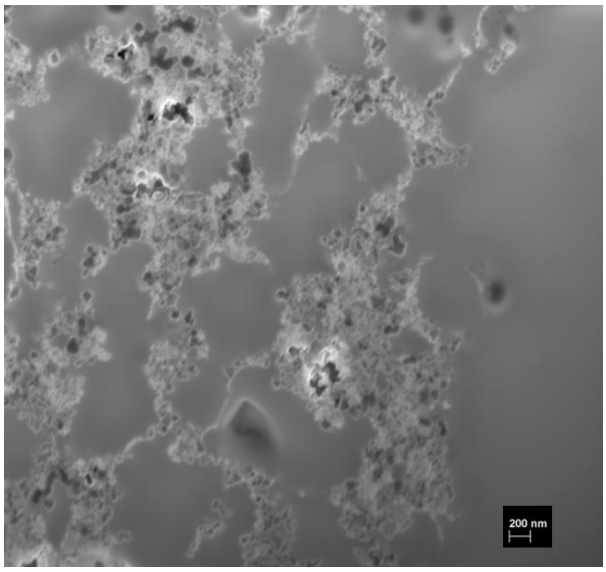

Figure 2-7 SEM micrographs of the electrode/membrane interface

In order to determine the maximum case, we must determine the surface area of the Pt nanoparticles on the carbon. Electrochemical characterization of the as-synthesized catalysts was carried out with cyclic voltammetry (CV) using a

glassy carbon working electrode, a gold wire counter electrode, and a $Hg/HgSO_4$ reference electrode in N_2-saturated 0.1M $HClO_4$ and was reported in this study[67]. The measured surface area was 45 m^2/g. For the minimum case, we bound our surface area to the electrolyte surface area in the electrode. In order to measure this surface area, we implemented BET, which is a technique based off of the Langmuir theory for monolayer adsorption. We measured the surface area to be 2 m^2/g.

Using these maximum and minimum surface areas we were able to determine a functional range for the exchange current density. The lower bound of the exchange current density based on the ECSA of Pt is 1.31 mA/cm^2 and for the upper bound based off of the electrolyte area is 29.48 mA/cm^2. A similar range is found for Pt in the literature[27,69–73]. Evaluation from the MEA structure in Figure 2-7 leads us to the suggestion that upper bound of 29.48 mA/cm^2 is closer to the true value. Although it is reasonable to assume that the CDP electrolyte is not in contact with all the Pt, which could also increase the exchange current density even higher to approach values that are reported in low temperature PEMFC cells. This general procedure is applied to all further catalyst studies. The 1.05 mg/cm^2 Pt supported on XC72 will act as the control case, and the basis for all of our supported catalysts.

Palladium is a slightly less expensive metal and resides closely to Pt in volcano plots of activity versus hydrogen bonding energy[64]. However in anodes, Pd typically shows worse performance[74,75]. Another issue for low temperature

anodes is the acidic liquid tends to compromise the stability of the Pd due to dissolution. Despite these issues, we decided to test Pd as a HOR and HER catalyst in solid acid hydrogen separation system. Palladium nanoparticles were deposited onto Vulcan XC-72R via a vapor-phase decomposition from their respective metal acetylacetonates $Pd(acac)_2$ These reactions were carried out using a fixed bed wherein the crystalline solid precursors were mechanically mixed with the Vulcan XC-72R carbon, in a N_2-water vapor atmosphere at elevated temperatures via a method that we have demonstrated in previous studies[52,56,68]. The ultimate deposition temperature was 180 °C.

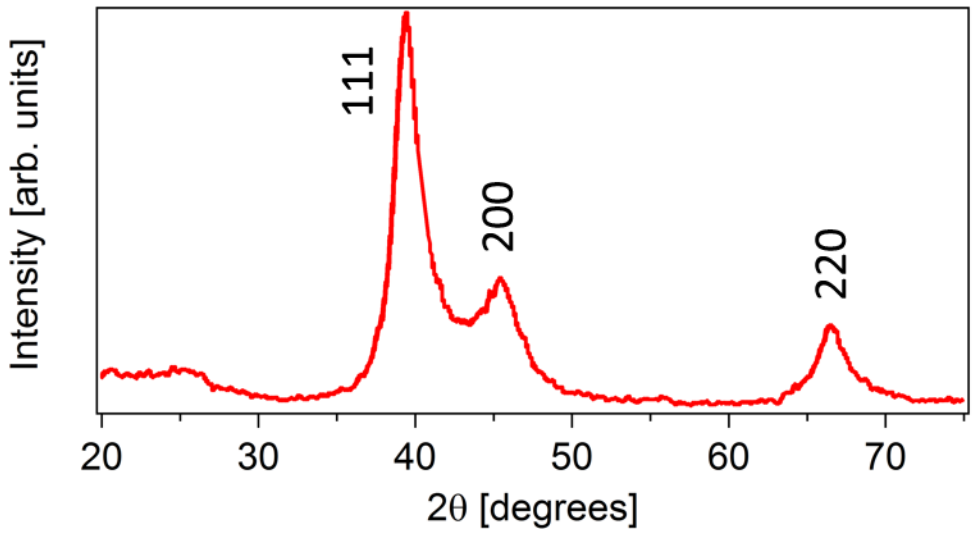

Figure 2-8 XRD pattern for vapor-grown 60% Pd/XC72

X-ray diffraction patterns for as-synthesized carbon-supported Pd have been previous reported[67]. We find for the Pd/C lattice parameter of 0.3965nm.

This is in slightly different than the tabulated value of 0.3892nm. Previous we have isolated this lattice expansion to the presence of interstitial carbon as a consequence of the metalorganic synthesis route[49]. Using the Scherrer relation (1-29) the particle size can be calculated to 4.3nm. These supported nanoparticles were then mechanically mixed with CDP and naphthalene in a similar fashion as the Pt electrodes. As-recorded and iR-free polarization curves for the Pt-Pd MEA acquired in pure H_2 at 250 °C are shown in Figure 2-9. A Pt/Pt control is also displayed for reference.

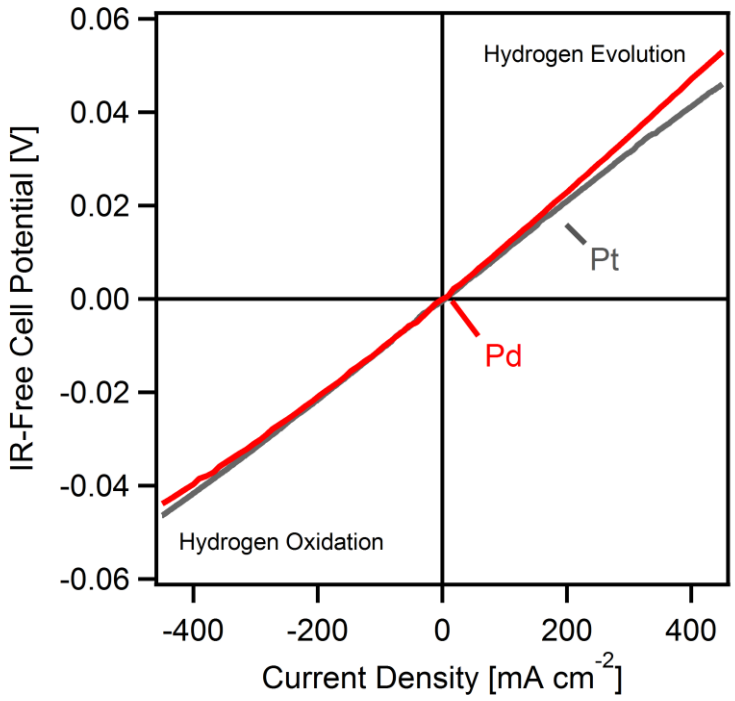

Figure 2-9 iR-free polarization curves acquired in hydrogen at 250 °C with 1.05mg/cm² electrodes for Pt/Pt and Pd/Pt

The curves are symmetric and the dominant loss channel is ohmic, accounting for around 80% of the total losses in the cell. Pd has a fairly linear response, however we note that as the current increases current starts to delineate. Contrary to Pt, Pd shows less symmetry to in the HOR vs HER reactions. While not by a large margin, Pd favors the HOR reaction to the HER reaction. Potential possibilities could include Pd ability to form Pd hydrides thus potentially increasing the anode reaction. This could also dampen Pd's ability to accept a proton on the cathode.

Figure 2-10 shows Tafel representations of iR-free polarization curves. Using the iR-free polarization curves at temperatures at 250 °C, we applied the Butler- Volmer equation (1-20). Allowing for i_o and ß to vary as free parameters, we applied a non-linear fitting to find the best fits for the polarization curves. A value of 0.4 was found for ß and a geometric exchange current density found was 407.5 mA/cm^2 for the hydrogen oxidation reaction and 0.415 for ß and 406.3 mA/cm^2 for the geometric exchange current density for the hydrogen evolution reaction. The area normalized current for Pd is 0.65-26.51 mA/cm^2, which lies within similar range to Pt. This is expected as Pt and Pd lie very close in the volcano plot for catalytic activity for the hydrogen reaction, however we must note the difference in performance from low temperature anodes. Pd has also been reported to be stable in CDP based hydrogen separation systems for over 100 hours at 0.1V overpotential[67]. We contribute this stability to the nature of the solid-gas electrode. However, Pd is not stable in fuel cell cathodes for solid acid

systems. This is contributed to the reactivity of Pd-oxides with the CDP electrolyte[49,57].

Ruthenium was selected as the next catalyst for the HOR and HER reaction in solid acid hydrogen separation devices. Although having similar scarcity to Pt, Ru is surprisingly 25 times less expensive. For low temperatures

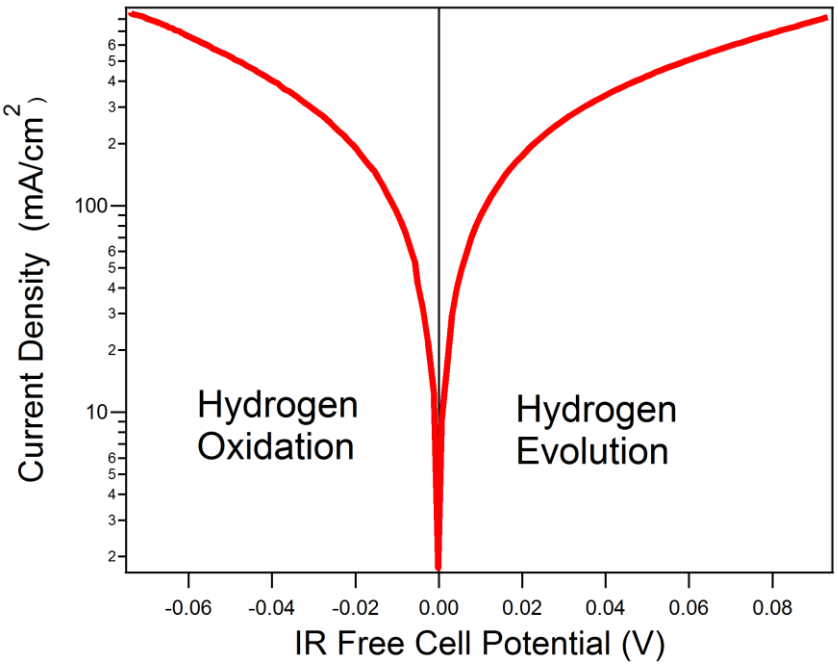

Figure 2-10 Tafel representation acquired in hydrogen at 250 °C with 1.05mg/cm² electrodes for Pd/Pt

in aqueous environments, Ru is a poor performer due to OH adsorbing to the catalyst for HOR and HER reactions. However, alloying Ru with Pt has shown an increase in performance as well as aiding in the removal of CO from the Pt

surface. Raising the temperature of the HOR reaction on pure Ru to 60°C from 25°C has also shown a large increase in performance. We hope that the removal of the aqueous solvent as well as the raising of the operational temperature to 250°C will lead to an effective HOR and HER catalyst in solid acid hydrogen separation devices. Ruthenium nanoparticles were deposited onto Vulcan XC-72R via a vapor-phase decomposition from its respective metal acetylacetonate, $Ru(acac)_3$ This reaction was carried out using a fixed bed wherein the crystalline solid precursors were mechanically mixed with the Vulcan XC-72R carbon, in a N_2-water vapor atmosphere at elevated temperatures via a method that we have demonstrated previously[52,56,68]. The ultimate deposition temperature was 240 °C. X-ray diffraction patterns for as-synthesized carbon-supported Ru are shown in Figure 2-11.

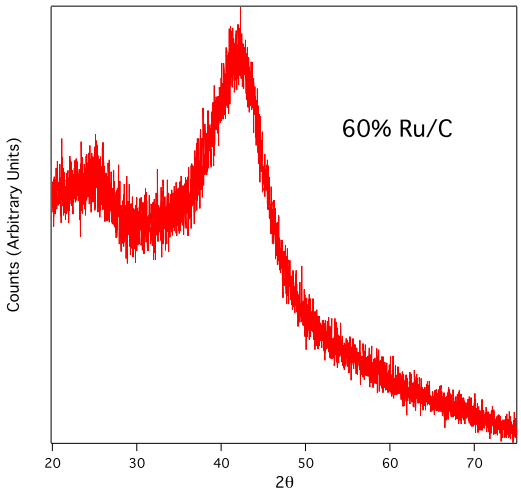

Figure 2-11 XRD pattern for vapor-grown 60% Ru/XC72

XRD is not a good indicator for measuring the particle size for Ru on XC72. In order to determine the particle size, TEM was used to measure the particles. This is depicted in Figure 2-12. All of the metal observed was present in contact with the carbon support. These supported nanoparticles were then mechanically mixed with CDP and naphthalene in a similar fashion as the Pt electrodes.

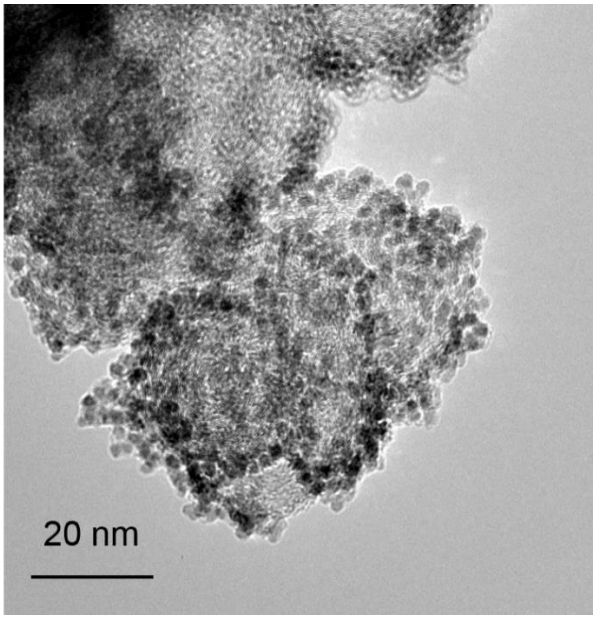

Figure 2-12 High resolution TEM micrographs of the Ru nanoparticles dispersed on Vulcan XC-72R

As-recorded and iR-free polarization curves for the Pt-Ru MEA acquired in pure H_2 at 250 °C are shown in Figure 2-13 for hydrogen oxidation and hydrogen evolution. The higher metal loading of 1.05 mg/cm^2 curves are relatively symmetric and the dominant loss channel is ohmic, accounting for around 70% of

the total losses in the cell. While Ru appears to have a linear trend, as the overpotential increases the slope increases. At 500 mV of cell overpotential the charge transfer resistance increases from 0.1 to 0.15 Ω cm^2. However the story is slightly different for the HER reaction. For the HER reaction, Ru remains linear for most of the curve. The disparity of the HOR/HER branches could possibly be explained by the difference in the M-H bond strength for Ru metal which resides on the side of the volcano plot known to absorb hydrogen less readily[64,76].

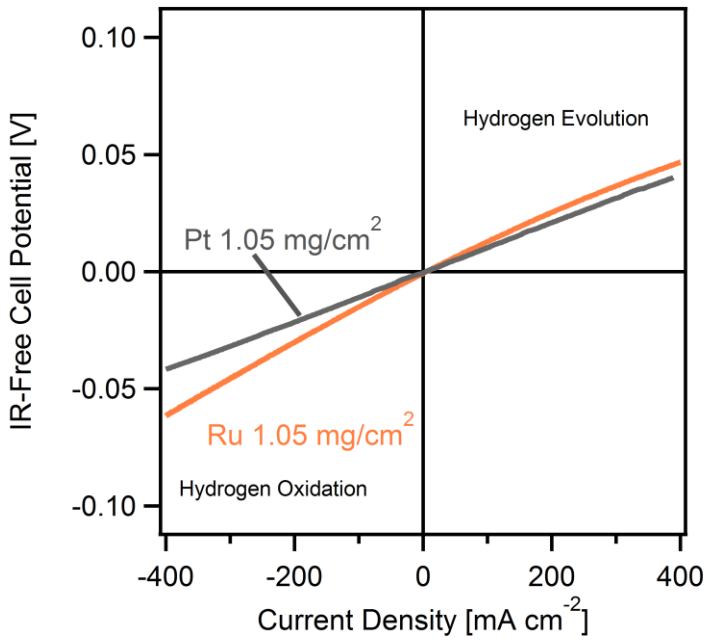

Figure 2-13 iR-free polarization curves acquired in hydrogen at 250 °C with 1.05mg/cm² electrodes for Pt/Pt and Ru/Pt

Figure 2-14 shows Tafel representations of iR-free polarization curves. Using the iR-free polarization curves at temperatures at 250 °C, we applied the Butler-

Volmer equation (1-20). Allowing for i_o and ß to vary as free parameters, we applied a non-linear fitting to find the best fits for the polarization curves. A value of 0.4 was found for ß and a geometric exchange current density found was 317.5 mA/cm^2 for the hydrogen oxidation reaction and 0.42 for ß and 319.8 mA/cm^2 for the geometric exchange current density for the hydrogen evolution reaction. This is a drastic difference between the low temperature aqueous cases[76].

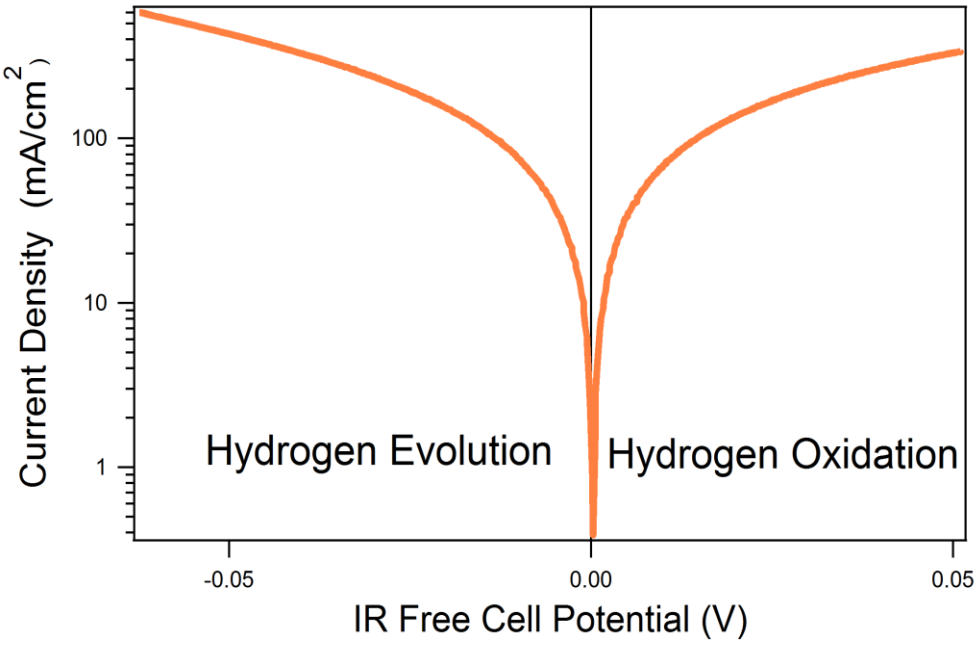

Figure 2-14 Tafel representation acquired in hydrogen at 250 °C with 1.05mg/cm² electrodes for Ru/Pt

Further investigation into the HOR reaction is conducted by deteremining the activation energy. This is done by determing the geometric exchange current

density at four temperatures: 230, 240, 250, and 260°C. By then assuming an Arrhenius relationship, the activation energy for the H_2 electrooxidation is determined. This is seen in Figure 2-15 by plotting the log of the geometric exchange current density vs 1/T. An activation energy of 32.8 kJ/mol is found. Low temperature studies of Ru and HOR electrooxidation in aqueous environments have found that Ru is a very poor HOR and HER catalyst due to the OH adsorption. DFT calculations for Ru (211) have shown similar results (35 kJ/mol) to ones collected in solid acid environments[77].

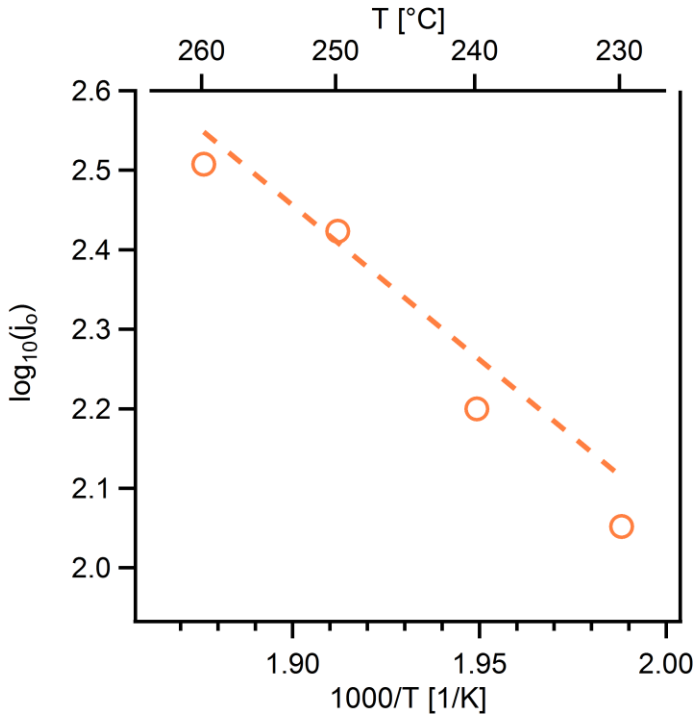

Figure 2-15 Exchange current density versus the inverse of temperature. Markers are the collected data points with the line details the linear fit

In order to further decrease the overall catalyst cost, we must branch our investigation into non-PGM catalysts. Copper is one such metal that has shown some minimal performance in low temperature environments. We hope that as a similar case to Pd and Ru that Cu will show better performance than its room temperature aqueous counterpart. Copper nanoparticles were deposited onto Vulcan XC-72R via a vapor-phase decomposition from its respective metal acetylacetonate, $Cu(acac)_2$ This reaction was carried out using a fixed bed wherein the crystalline solid precursors were mechanically mixed with the Vulcan XC-72R carbon, in a N_2-water vapor atmosphere at elevated temperatures via a method that we have demonstrated previously[52,56,68]. The ultimate deposition temperature was 240 °C. X-ray diffraction patterns for as-synthesized carbon-supported Cu are shown in Figure 2-16. Based off of the Cu(111) we calculate the d-spacing of 0.2088nm. Using the Scherrer relation the particle size can be calculated to 34.1nm. We note the shard difference between the relatively small particles of Pt, Pd, and Ru to the larger particles of Cu. We also find that Cu_2O is found in this XRD analysis. We expect all of the copper oxide to be reduced to copper metal in the hydrogen environment at operation conditions. However, this may not be the case. These supported nanoparticles were then mechanically mixed with CDP and naphthalene in a similar fashion as the Pt electrodes. These mixtures were then laminated as electrodes.

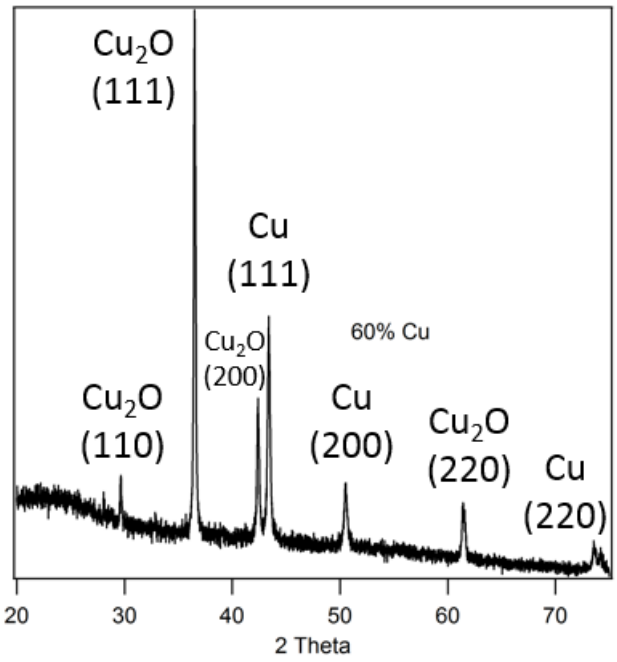

Figure 2-16 XRD pattern for vapor-grown 60% Cu/XC72

As-recorded and iR-free polarization curves for the Pt-Cu MEA acquired in pure H_2 at 250 °C are shown in Figure 2-17. The hydrogen oxidation of copper is seemingly nonexistent however an interesting cyclic feature is found in the higher over potentials.

Observation of the polarization curve shows that contrary to the PGM, Cu does not show a linear profile. These kinetics are highlighted in the EIS spectra showing the large increase in the charge transfer resistance in Figure 2-18. For HOR the current response is practically 0. This is expected as Cu does not readily absorb hydrogen which is a fundamental step to hydrogen oxidation[64,78,79].

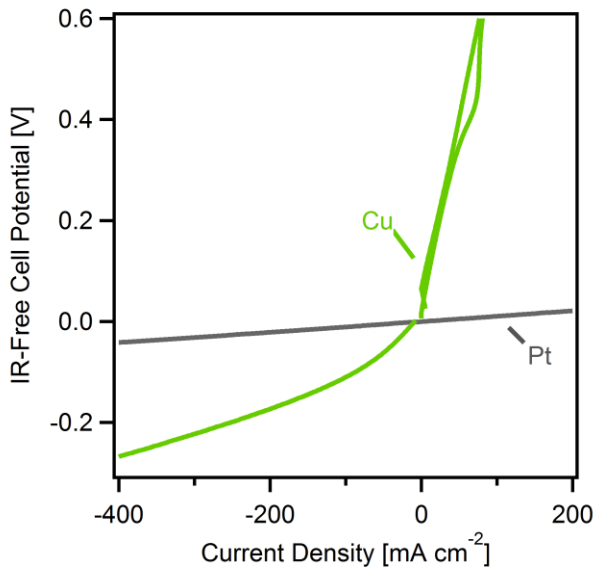

Figure 2-17 iR-free polarization curves acquired in hydrogen at 250 °C with 1.05mg/cm² electrodes for Pt/Pt and Cu/Pt

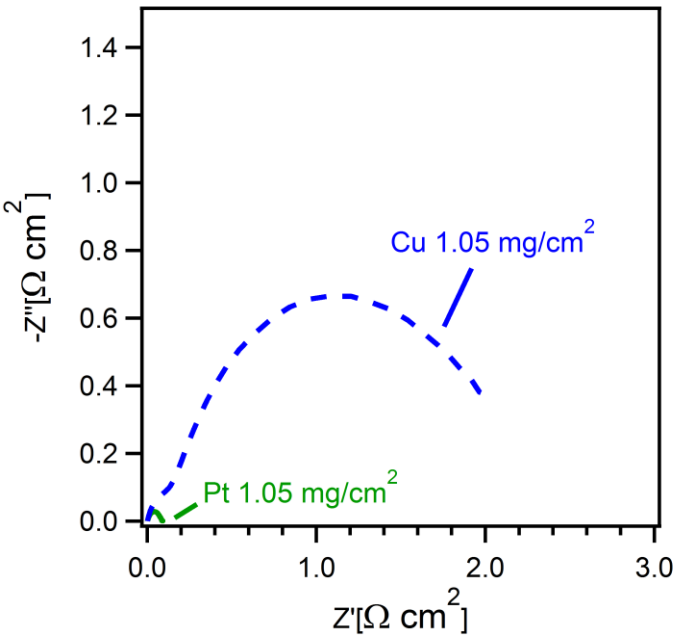

Figure 2-18 EIS spectra collected at 50 mV of over potential for Pt/Pt and Cu/Pt

Figure 2-19 shows Tafel representations of iR-free polarization curves. Using the iR-free polarization curves at temperatures at 250 °C, we applied a modified Butler-Volmer equation (1-21). Based on the hydrogen oxidation current, the effective anodic transfer coefficient for hydrogen oxidation approached 0. Using the low field approximation we estimate the geometric current density to be 18.7 mA/cm^2. This is based off the charge transfer coefficient found at OCV which is 2.5 Ω cm^2. This is drastically larger than the recorded value for all of the PGM metals that we have explored previously. The charge transfer resistance for Pt is 0.07 Ω cm^2 and is also depicted in Figure 2-18.

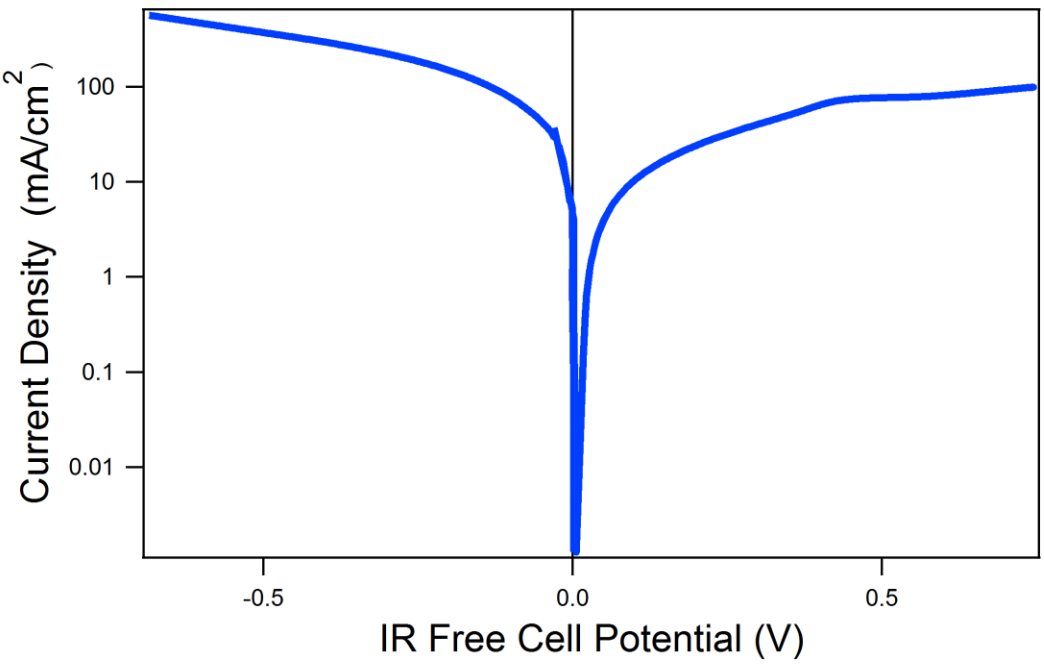

Figure 2-19 Tafel representation acquired in hydrogen at 250 °C with 1.05mg/cm² electrodes for Cu/Pt

Our next non-PGM selected for catalyst investigation is nickel. Previous studies have shown Ni to be effective for hydrogen evolution from CsH_2PO_4, however, these studies were conducted using unsupported Ni in the cathode with a net Ni loading of $3.5 mg_{Ni} cm^{-2}$ [39]. We hypothesized that a carbon-supported catalyst analogous to those that we have previously demonstrated could improve Ni dispersion and utilization and permit lower quantities of catalyst to be used. Ni nanoparticles were deposited onto Vulcan XC-72R via a vapor-phase decomposition from its respective metal acetylacetonate, $Ni(acac)_2$ This reaction was carried out using a fixed bed wherein the crystalline solid precursors were mechanically mixed with the Vulcan XC-72R carbon, in a N_2-water vapor atmosphere at elevated temperatures via a method that we have demonstrated previously[52,56,68]. The ultimate deposition temperature was 240 °C. These supported Ni nanoparticles were then subjected to a heat treatment at 500°C in N_2 for 3 hours in order to finish reacting all of the precursor. Figure 2-20 shows a Cu Ka XRD pattern and high resolution TEM images of the experimental carbon supported Ni after heat treatment at 500°C. The Ni nanoparticles show a d spacing of 2.049 Å which is consistent with the expected value of 2.035 Å. Figure 2-20b shows clear diffraction rings which are consistent with the reported values for FCC Ni. Figure 2-20c shows the XRD pattern obtained from the as-synthesized Ni nanoparticles on Vulcan XC72. Peak characteristics display FCC Ni metal with Scherrer analysis of this pattern showing a mean crystalline domain

size of 31 nm. D-spacing analysis using the Scherrer relationship shows a mean spacing of 2.034 Å also consistent with the expected value.

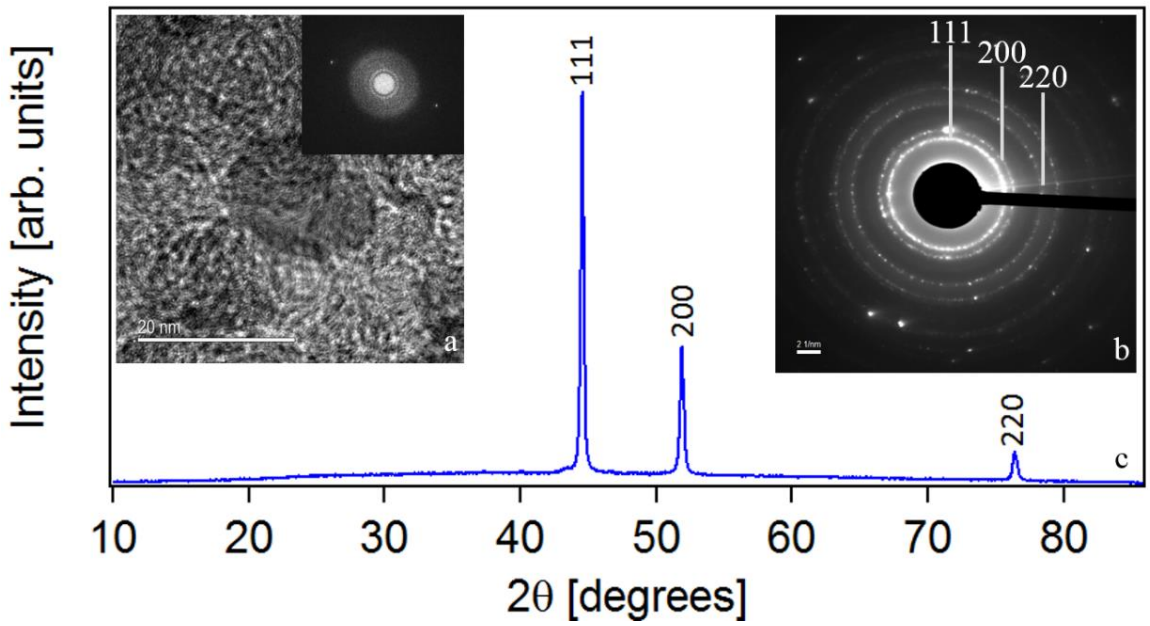

Figure 2-20 (a) High resolution TEM showing supported Ni nanoparticle with a d-spacing of 2.049 Å, consistent with the {111} (b) shows clear diffraction rings consistent with fcc Ni. (c) Shows XRD

As-recorded and iR-free polarization curves for the Pt-Ni MEA acquired in pure H_2 at 250 °C are shown in Figure 2-21 for hydrogen evolution. As-recorded and iR-free polarization curves for the Pt-Ni MEA acquired in pure H_2 at 250 °C are shown in Figure 2-22 for hydrogen oxidation. FCC Ni has practically no HOR activity. This asymmetry, in similar fashion to copper can be explained by the lack of hydrogen adsorption[64,78,80].

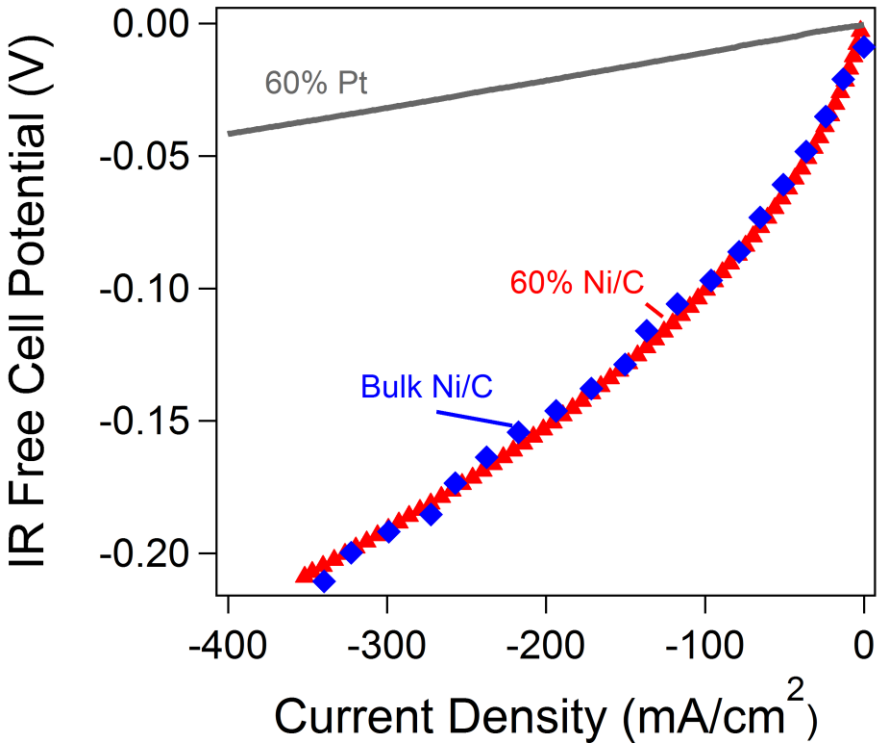

Figure 2-21 iR-free polarization curves acquired in hydrogen at 250 °C for HER with 1.05mg/cm² electrodes for Pt/Pt and Ni/Pt

A Tafel representation of supported Ni in shown in Figure 2-23 showing the disparity of the HOR and HER electrodes. Using the low field approximation we estimate the geometric exchange current density to be 27.3 mA/cm^2 for the FCC nickel.

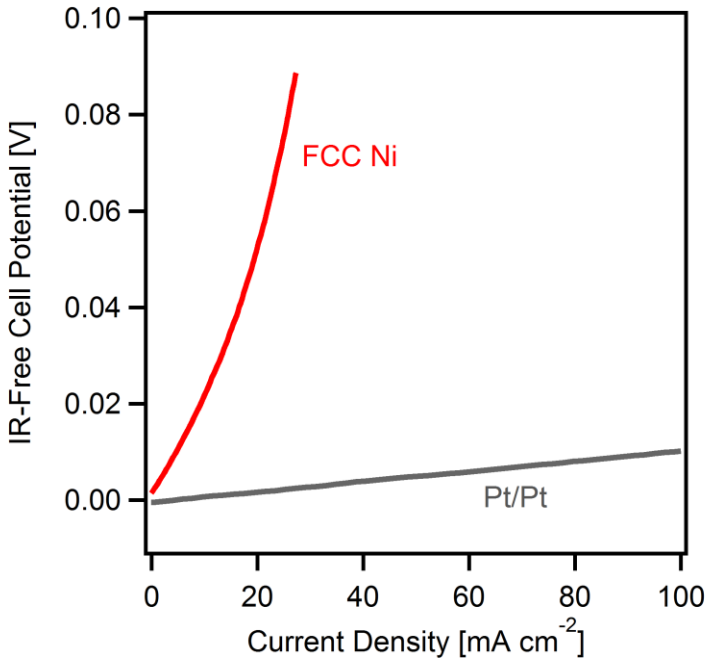

Figure 2-22 iR-free polarization curves acquired in hydrogen at 250 °C for HOR with 1.05mg/cm² electrodes for Pt/Pt and Ni/Pt

For Ni, the clear asymmetry in the rate of the HOR/HER could possibly indicate a different mechanism between the two. For the HOR reaction, the charge transfer resistance increases with over potential, possibly indicating

poisoning of binding sites or mass transport limitation. For the HER reaction, the charge transfer resistance decreases with overpotential.

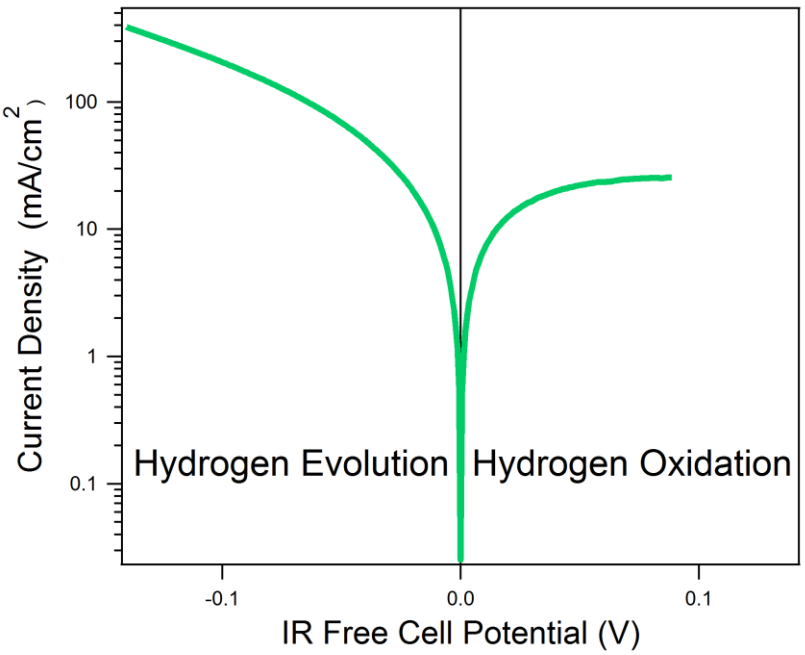

Figure 2-23 Tafel representation acquired in hydrogen at 250 °C with 1.05mg/cm² electrodes for Ni/Pt

For various catalytic reactions, metal alloys have been shown to increase performance. While copper and nickel have been investigated at low temperatures, there was no investigations into alloys of the two. Two cases of Cu and Ni alloys were investigated.

Cu and Ni nanoparticles were deposited onto Vulcan XC-72R via a vapor-phase decomposition from their respective metal acetylacetonates by simultaneous mixing These reactions were carried out using a fixed bed wherein

the crystalline solid precursors were mechanically mixed with the Vulcan XC-72R carbon, in a N_2-water vapor atmosphere at elevated temperatures via a method that we have demonstrated previously[52,56,68]. The ultimate deposition temperature was 240 °C. These supported nanoparticles were then subjected to a heat treatment at 500°C in N_2 for 3 hours in order to finish reacting all of the precursor. X-ray diffraction patterns for as-synthesized carbon-supported Ni/Cu are shown in Figure 2-24

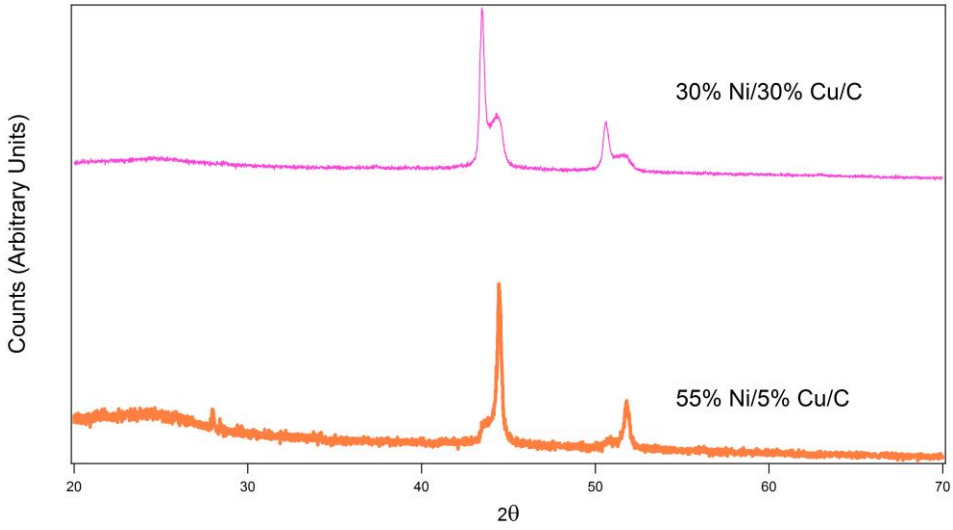

Figure 2-24 XRD pattern for vapor-grown 60% Ni and Cu onXC72

Using the Scherrer relation the particle size can be calculated to 29.1nm. Figure 2-25 shows HOR and HER polarization curves for Pt-Cu/Ni MEAs. In similar fashion to Cu and Ni, Cu/Ni has very limited HOR reaction. However the cyclic

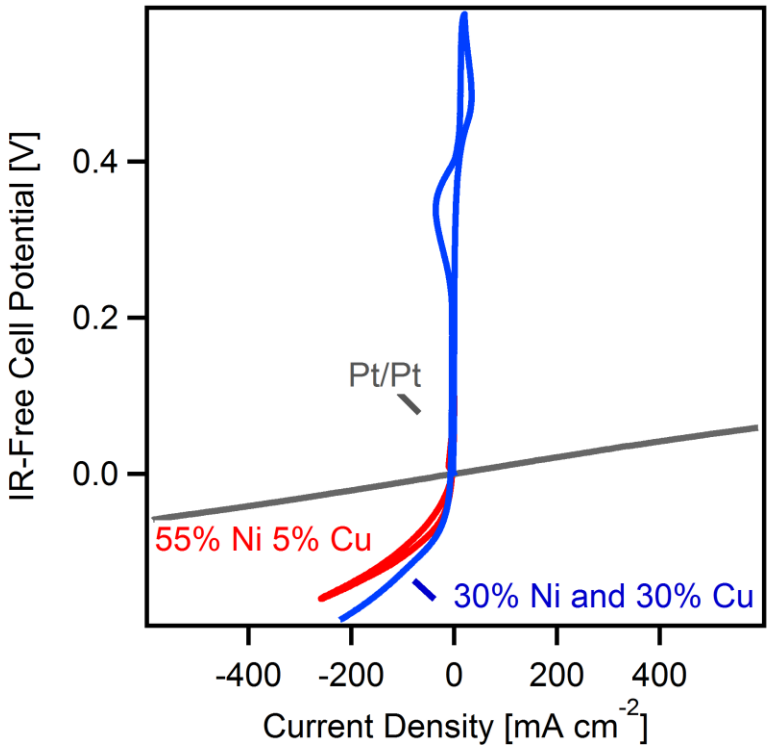

Figure 2-25 iR-free polarization curves acquired in hydrogen at 250 °C with 1.05mg/cm² electrodes for Pt/Pt and NiCu/Pt

feature shown in base copper still remains. The performance of both alloys are less than 60% Ni supported on the same carbon support.

Nickel was also combined with Ru in order to determine if any benefit, specifically to the HOR reaction could be achieved. Ni and Ru nanoparticles were deposited onto Vulcan XC-72R via a vapor-phase decomposition from their respective metal acetylacetonates This reaction was carried out using a fixed bed wherein the crystalline solid precursors were mechanically mixed with the Vulcan XC-72R carbon, in a N_2-water vapor atmosphere at elevated temperatures via a method that we have demonstrated previously[52,56,68]. The ultimate deposition temperature was 240 °C. X-ray diffraction patterns for as-synthesized carbon-supported Ni/Ru are shown in Figure 2-26.

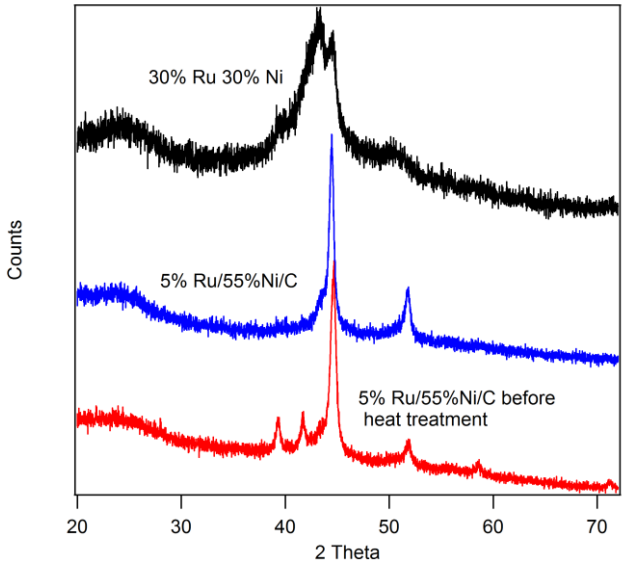

Figure 2-26 XRD pattern for vapor-grown 60% Ni and Ru on XC72

These supported Ru-Ni nanoparticles were then subjected to a heat treatment at 500°C in N_2 for 3 hours in order to finish reacting all of the precursor. Using the Scherrer relation the particle size can be calculated to 12.8nm for 30%Ru and 30% Ni. We do note the significantly smaller particle size associated with the use of Ru as well with Ni. Even at 5% Ru, the particle size decreases from 31nm to 19nm. This could have to do with the autocatalytic nature of the deposited Ru metal in aiding in decomposition of the metal organic precursor.

Figure 2-27 shows HER polarization curves for Pt-Ru/Ni MEAs. When these samples are compared to the Ru HER Figure 2-13 we see a minor increase in performance vs the 5% and the 30% Ru.

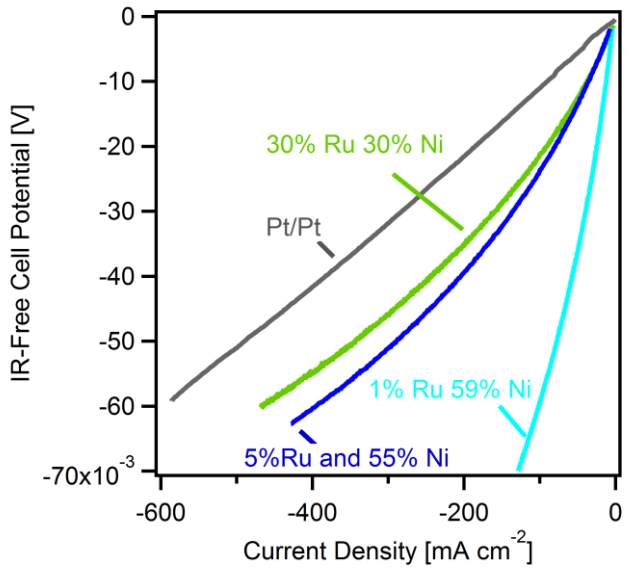

Figure 2-27 iR-free polarization curves acquired in hydrogen at 250 °C for HER with 1.05mg/cm² electrodes for Pt/Pt and RuNi/Pt

However, the addition of Ni to the electrode completely eliminates Ru HOR capabilities. This is depicted in Figure 2-28. Possibilities include alloying the Ru with Ni inhibits the absorption of hydrogen to the surface. Ni effectively poisons the HOR reaction surface in this temperature range.

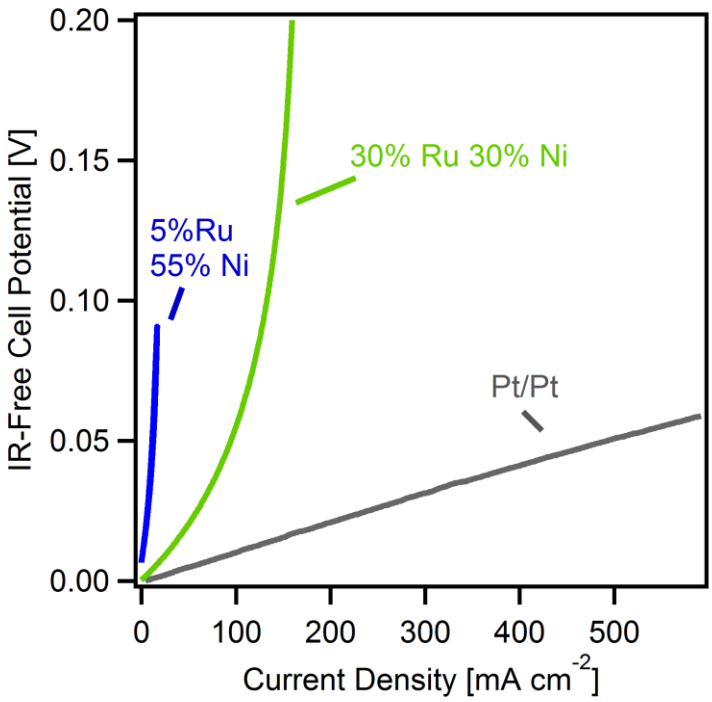

Figure 2-28 iR-free polarization curves acquired in hydrogen at 250 °C for HOR with 1.05mg/cm² electrodes for Pt/Pt and RuNi/Pt

While alloying always has the potential to increase the performance, in the case of HOR/HER electrodes for Ni, Cu and Ru, it is best to stick to the base metals in our current fabrication scheme. Although the degree of alloying was not 100%, we do not expect any further alloying to increase the performance.

Table 2-1 shows a summary of measured exchange current densities ranges for Pt, Pd, Ru, Cu, and Ni HER in solid acid systems compared to those measured in aqueous environments[64]. The lower bounds are bounded by the surface area of the electrolyte, while the upper bound is bounded by the ECSA as calculated in aqueous environments.

Table 2-1 Hydrogen evolution exchange current densities as reported for CDP systems at 250°C compared to the aqueous cases found in the literature

Sample	Literature $(mA/cm^2)_{metal}$	This Study $(mA/cm^2)_{metal}$
Pt	49.79	1.31-29.48
Pd	45.05	0.65-26.51
Ru	15.00	0.53-20.86
Cu	0.41	1.22-4.17
Ni FCC	5.25	1.78-6.09

Despite having the lowest performance, Cu shows the largest deviation from the reported literature values. For hydrogen oxidation, Pt remains superior but Pd and Ru shows surprising promise for an effective catalyst. For HER, Pd, Ru and Ni shows promise as a less expensive hydrogen evolution catalysts.

Conclusion

We have demonstrated a suite of carbon-supported catalysts (Pt, Pd, Ru, Ni and Cu) for implementation in electrodes for both the anode and the cathode. Though not nearly as active as Pt, Pd and Ru show promise for both the hydrogen oxidation catalyst as well as the evolution reaction. Nickel and copper are not active for hydrogen oxidation. Copper was not as active as nickel for hydrogen evolution, but showed a drastic increase in performance from previously reported values. We expect the performance can be further improved by optimization of the electrode microstructure and dispersion of the catalyst.

CHAPTER 3

SOLID ACID ELECTROLYTE MEMBRANES ENABLE PLATINUM-FREE ELECTROCHEMICAL SEPARATION OF HYDROGEN FROM REFORMED METHANOL

Abstract

We demonstrate a device for electrochemical hydrogen separation from reformed methanol using a proton-conducting CsH_2PO_4 membrane and platinum-free electrodes at an operational temperature of 250°C. Carbon-supported Ru and Ni catalyst were synthesized via vapor deposition and used as hydrogen oxidation and evolution catalysts, respectively. Methanol steam reforming proceeded with a commercial copper-based catalyst incorporated into the cell assembly. Devices free of Pt produced a hydrogen evolution current of 300 mA cm^{-2} at a cell voltage of 0.35 V.

Introduction

Recent increases in natural gas production in the United States have renewed interest in chemicals and fuels produced from methane. This includes hydrogen and methanol, both of which are principally derived from catalytic reforming of natural gas. Hydrogen is a crucial feedstock for the chemical industry, as well as a potential fuel for vehicular and stationary applications based on air-breathing fuel cells. A stumbling block to the widespread adoption of these fuel cell technologies has been the lack of a distribution network for gaseous hydrogen coupled with its low volumetric energy density. In contrast

with hydrogen gas, liquid fuels, including methanol, exhibit distinct advantages in volumetric energy density and ease of transport. Using methanol as a fuel has been heavily investigated, and considerable progress has been made in the area of proton-conducting direct methanol fuel cells (DMFCs), which directly electrooxidize methanol in conjunction with an air electrode to produce electrical power. The obstacles to the widespread use of low-temperature polymeric direct methanol cells are extensive, however, due to issues such as a low thermodynamic equilibrium voltage, surface adsorption of oxidation products on catalysts, and methanol crossover through ionomeric membranes.

An alternative approach to direct electrooxidation is the use of methanol molecules as chemical hydrogen carriers, relying on distributed catalytic reforming to produce hydrogen fuel on demand[81] for a given application. This process can proceed via multiple pathways in the presence of water, namely, the steam reforming (3.1), decomposition (3.2), and the water gas shift (3.3) reactions

$$CH_3OH + H_2O \rightarrow CO_2 + 3H_2 \quad \Delta H^o = 49.5\ kJ/mol \tag{3.1}$$

$$CH_3OH \rightarrow CO + 2H_2 \quad \Delta H^o = 90.2\ kJ/mol \tag{3.2}$$

$$CO + H_2O \rightarrow CO_2 + H_2 \quad \Delta H^o = -41\ kJ/mol \tag{3.3}$$

The most widely used methanol reforming catalysts are based on copper, typically $Cu/ZnO/Al_2O_3$[32,82–84] At lower temperatures, steam reforming (3.1) is

thermodynamically favored, but as the reforming temperature is increased decomposition (3.2) becomes more prevalent. Copper-based catalyst display high activity and low cost, however catalyst durability may be an issue[85]. Recent work on Pd/ZnO catalysts have shown greater hydrogen yields than Cu-based catalysts at moderate temperatures and an improved resistance to deactivation, though the presence of Pd may limit the reach of these materials.

In a reforming-based hydrogen production scheme, separation of hydrogen from the byproducts of the reforming reaction is a crucial element of the process. One relatively new method that has been proposed is electrochemical hydrogen separation. In this scheme, hydrogen is selectively oxidized at a gas-diffusion electrode exposed to a multicomponent gas stream, producing protons, which are electrochemically "pumped" across a proton-conducting membrane via an applied potential and subsequently evolved as gaseous hydrogen at the conjugate gas-diffusion electrode. Multiple proton-conducting electrolytes have been proposed for this application, including perfluorinated sulfonic acid (PFSA) polymers operating at low temperatures (~80 °C)[2,23], Phosphoric acid and phosphoric acid-doped polybenzidazole (PBI) at intermediate temperatures (~180 °C)[24,25], and proton-conducting oxide membranes at higher temperatures (>500 °C)[26]. In the case of methanol, the intermediate temperature range (150°C to 300 °C) is uniquely favorable, due to the increased resistance of hydrogen oxidation catalysts (typically platinum) to poisoning[27–30]. We also note a thermal match to the optimal methanol reforming

temperature of 240-260°C,[31] and the ability to use a conventional low-cost materials set for stack and system components that is obviated at higher temperatures.

Here we consider the crystalline solid-state proton conductor CsH_2PO_4 (CDP) as an electrolyte for hydrogen separation from reformed methanol. Operating at temperatures greater than 230 °C, CDP-based cells are perfectly matched to the optimal temperature range for methanol steam reforming, allowing the reforming catalyst to be directly integrated into the cell assembly. The first work to demonstrate this architecture used a fuel stream consisting of methanol and water vapor and a Pt anode catalyst coupled with a Pt-based air electrode for electricity production[37]. Later electricity-producing cells also demonstrated a tolerance to fuel streams containing as much as 20% CO[58] with Pt anode catalysts. Recently, we showed that CDP membranes can also be used for electrochemical hydrogen separation from reformate streams containing similar concentrations of contaminants[38].

The prospects for electrochemical hydrogen separation devices based on CDP are likely to remain limited if restricted to Pt-based electrodes, simply due to cost. Therefore we have sought non-platinum catalysts that are suitable replacements in the case of the hydrogen oxidation and evolution reactions. We found that unsupported nanoparticulate Ni is active for hydrogen evolution from CDP[39] and that carbon-supported elemental Ru can be substituted as a CO-tolerant hydrogen oxidation catalyst. In this article, we describe cells based on

carbon-supported Ru anodes and carbon-supported Ni cathodes to realize the production of pure hydrogen from reformed methanol in the absence of a Pt catalyst.

Experimental Methods

CsH_2PO_4 was synthesized by reaction of $CsCO_3$ (Alfa Aesar, 99%) with H_3PO_4 (Alfa Aesar, 85%) followed by precipitation in methanol and drying. The as-synthesized CDP was low-energy ball-milled to reduce its initial particle size, yielding a fine particulate powder with a BET surface area of approximately 2 m^2/g. Carbon-supported metallic nanoparticles were synthesized as hydrogen oxidation and evolution catalysts. Platinum, ruthenium, and nickel nanoparticles were deposited onto Vulcan XC-72R via a vapor-phase decomposition from their respective metal acetylacetonates $Pt(acac)_2$ (Strem Chemical), $Ru(acac)_3$ (Sigma-Aldrich), and $Ni(acac)_2$ (Alfa Aesar). These reactions were carried out using a fixed bed wherein the crystalline solid precursors were mechanically mixed with the Vulcan XC-72R carbon, in a N_2-water vapor atmosphere at elevated temperatures via a method that we have demonstrated previously[36,46,52,56,66,67]. The ultimate deposition temperature varied for each species deposited, from 210 °C (platinum) to 240 °C (ruthenium and nickel). The carbon-supported nickel sample was further heat treated at 500°C under N_2 for 3 hours in flowing N_2.All catalysts were characterized with using X-ray diffraction

(XRD) (Philips X'Pert, l ¼ 0.1541874 nm) and transmission electron microscopy (Zeiss Libra 200MC). The position and width of diffraction peaks were obtained by fitting to Voight functions using IGOR Pro (Wavemetrics, Inc.).

Composite electrocatalyst powders were synthesized by dry-grinding the fine CDP with the various metal/carbon catalyst and naphthalene (a fugitive binder). These mixtures kept the mass ratio of CDP, naphthalene and carbon to 3: 1: 0.4 (mass) allowing for variation of the electrode catalyst mass without modifying the electrode thickness. Hydrogen pump membrane-electrode assemblies (MEAs) were then fabricated using these electrocatalysts by lamination of active layers in a 2.85 cm^2 diameter hardened steel die. Stainless steel mesh was used for current collector and PTFE tape for a sealant. Each MEA had a membrane thickness of approximately 75 to 85 microns. The mass of a given electrode varied between 22 to 28 mg dependent on the metal loading on the carbon support. In each cell, the hydrogen evolution electrode was laminated at 125 MPa while the hydrogen oxidation electrode was laminated at 25 MPa. Control cells were fabricated using Pt catalysts on both electrodes; experimental cells were fabricated with a Ru-based anode and a Ni-based cathode with a metal loading of 1.05mg/cm^2.

A methanol reforming layer was fabricated by compressing a composite of 850 mg of coarsely pulverized $Cu/ZnO/Al_2O_3$ methanol reforming catalyst (HiFuel R120) and 150 mg of fine CDP between two pieces of Ni foam (INCO).

The cell assembly, consisting of the MEA and reforming layer, was installed in a stainless steel fixture for testing.

Prior to electrochemical testing, the cell assembly was heated to 150 °C in dry Ar, followed by a two hour treatment in 4% H_2/Ar mixture to reduce the methanol reforming catalyst. Both electrodes were then switched to a wet Ar purge at 75 °C dew point and heated to the testing temperature of 250 °C.

Electrochemical testing was conducted at 250 °C. At the start of the experiment, each electrode was supplied 30 sccm of humidified ultrahigh purity hydrogen at a 75 °C dew point. Polarization curves were recorded at 1 hour intervals with a Bio-Logic VSP potentiostat by scanning the working electrode potential at 5 mV s^{-1} from the open circuit voltage (OCV) to -0.3 V and then to 0.3V. Potentiostatic electrochemical impedance spectroscopy (PEIS) spectra were also recorded at -50 mV versus OCV in a frequency range from 200 kHz to 200 mHz with a single sine perturbation amplitude of 10 mV. Polarization curves free of the ohmic losses due to membrane resistance were derived by the subtraction of the current multiplied by the high frequency resistance measured at OCV. Cells were held at -50 mV for 1 hour between testing cycles. After 15 hours, humidified hydrogen on the anode was replaced with delivery of 6mL/hr of vaporized 1:1 methanol to water (volume) entrained in a carrier gas flow of 10 sccm of ultrahigh-purity argon. After 1 hour, electrochemical tests were conducted using the same electrochemical procedures. In situ gas chromatography-mass spectrometry (GC-MS) experiments were conducted by

directly flowing the anode outlet stream through a Nafion gas dryer then into the Shmidazu GCMS.

Imaging of electrodes and chemical analysis was conducted with a Hitachi TM3000 SEM equipped with a Bruker Quantax EDS system operating at 15 kV. These were supported on an Al stub using double sided carbon tape.

Results and Discussion

Syngas and natural gas reformate are two hydrogen rich fuel streams that are commonly made during industrial processes. Syngas can contain 30-60% carbon monoxide (CO), 25-30% hydrogen (H_2), 0-5% methane (CH_4), 5-15% carbon dioxide (CO_2), plus a lesser or greater amount of water vapor, smaller amounts of the sulfur compounds hydrogen sulfide (H_2S), carbonyl sulfide (COS), and finally some ammonia and other trace contaminants[86]. At these CO concentrations, further oxidative conversion of CO is desirable to boost hydrogen yield. Ru is capable of enhanced hydrogen production in CO-rich input streams. Previously, we attributed this result to a synergistic interaction of the water-gas shift (WGS) reaction and CO electrooxidation. In order to determine the reason for this enhanced performance, we consider separately the heterogeneous WGS and CO electrooxidation properties of Ru and other supported catalysts for optimizing electrode architectures for hydrogen separation from highly CO-enriched simulated syngas streams. Functionally graded anodes are fabricated

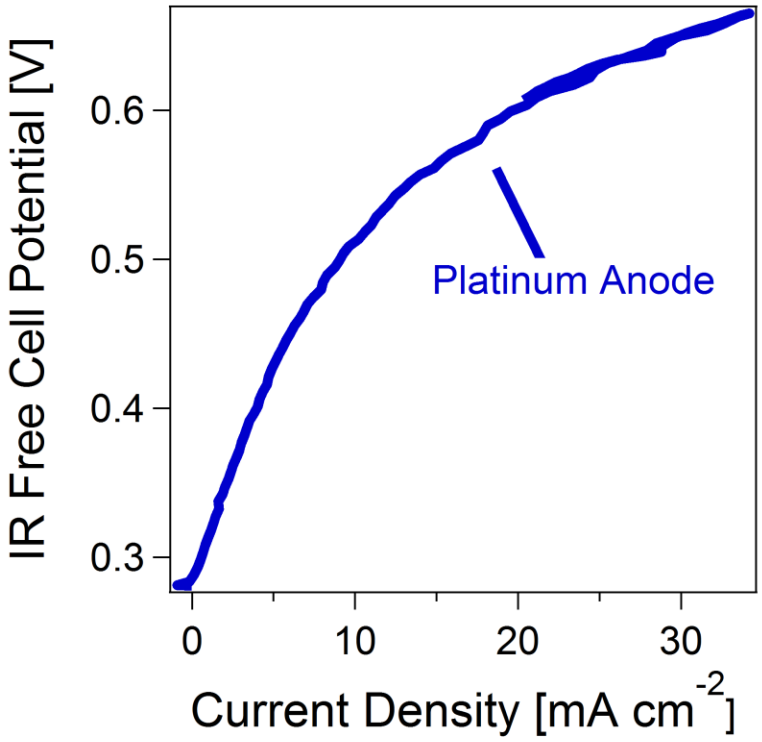

Figure 3-1 iR-free polarization curves acquired in 45% CO balance Ar at 250 °C with 1.05mg/cm² listed anode and 1.05mg/cm² Pt cathode

to balance CO conversion activity with hydrogen oxidation. Figure 3-1 is an IR-free polarization curve obtained at 250 °C under 45% CO, balance Ar anode stream. The cathode is a pure hydrogen input on a Pt electrode. Both gas inputs are hydrated to 75 °C dew point. By applying the Nernst equation (1-9) with the measured OCV, the partial pressure of hydrogen can be estimated for this anode. This anode's OCV is 281 mV which equates to 2.8e-4% of hydrogen being produced in the anode. Pt has negligible performance for CO electrooxidation as well as WGS.

In order to further investigate the effect of the Ru WGS reaction, a Ru layer with the exact same composition to a ruthenium anode is added to the microporous layer during cell fabrication. This layer is ionically separated from the anode in order to ensure that only the WGS reaction is occurring from the Ru nanoparticles. This is depicted in Figure 3-2

This new electrode's (electrode II) OCV is 141 mV, which equates to 1.4e-1% of hydrogen in the anode. The presence of Ru does have an effect as a WGS catalyst as demonstrated in the 3 orders of magnitude increase in the partial pressure of hydrogen. This is not surprising since Ru is known to be a fairly active WGS catalyst[87–90]. However, we notice that with our current setup for Ru on carbon that the water gas shift reaction is much lower than reported for Ru catalyst supported on ceramics.

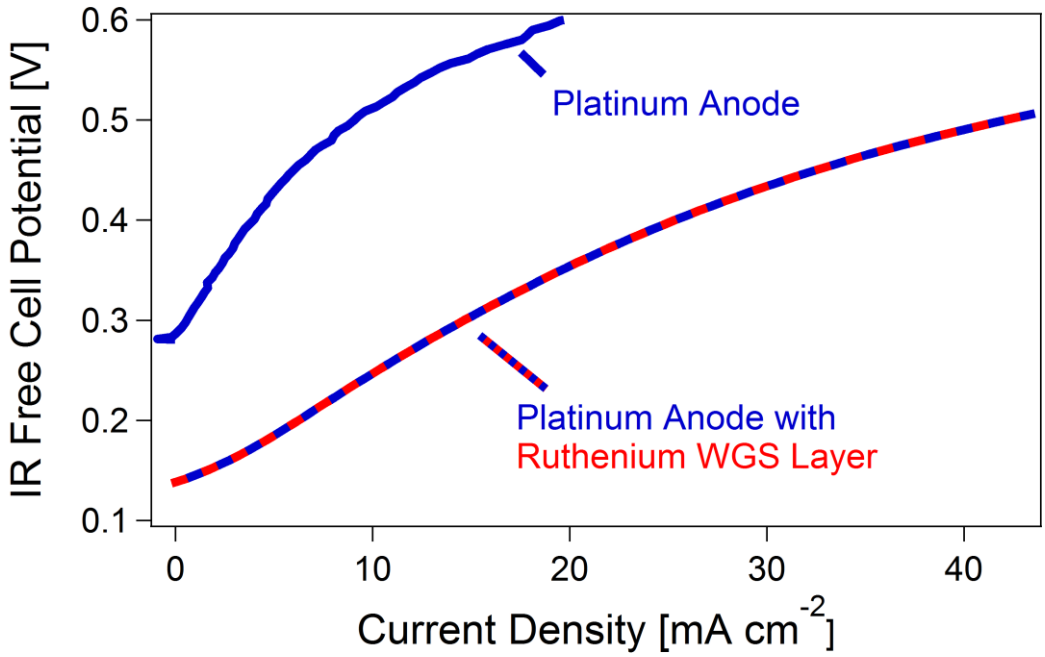

Figure 3-2 iR-free polarization curves acquired in 45% CO balance Ar at 250 °C with 1.05mg/cm² listed anode and 1.05mg/cm² Pt cathode

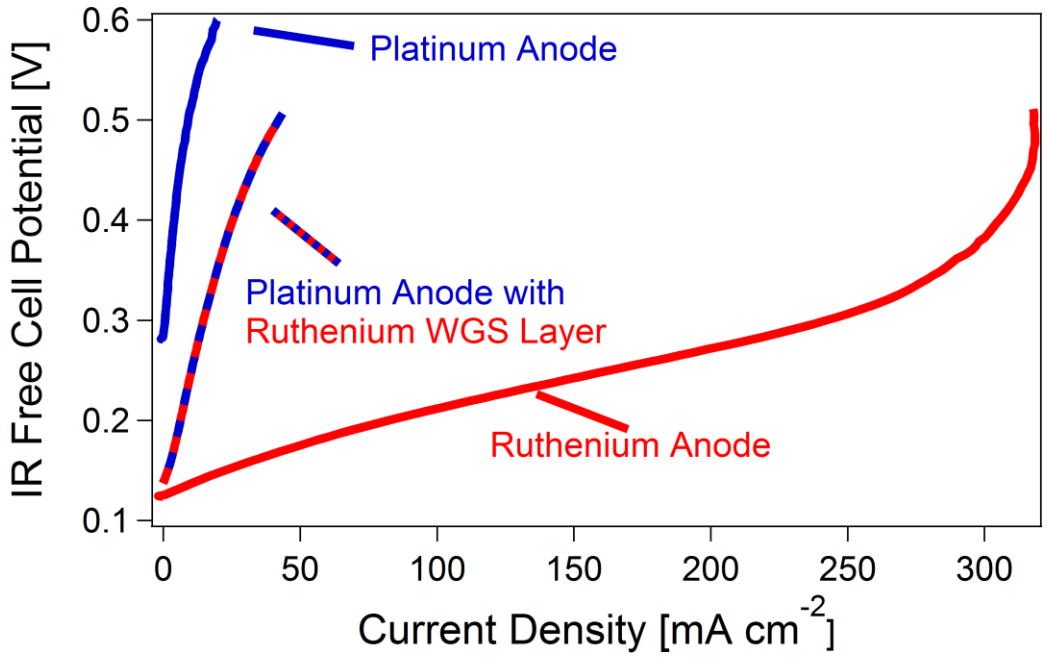

Figure 3-3 iR-free polarization curves acquired in 45% CO balance Ar at 250 °C with 1.05mg/cm² listed anode and 1.05mg/cm² Pt cathode

The last architecture investigated was ruthenium anode. The iR-free polarization curve can be observed in Figure 3-3. The Ru anode (electrode III) has an OCV of 125 mV, which equates to 2.7e-1% hydrogen in the anode. The difference between the OCV between electrode II and electrode III is attributed to the partial poisoning of the Pt electrode, leading to decrease of the absorbed H_2 to the electrode's surface. The large difference between the Pt anode and the Ru anode is immediately aware. Ru has been known to electrooxidize CO at lower temperatures, but it is commonly assisted by Pt[91–97]. Ru also assists Pt in low temperature acid aqueous electrooxidation of methanol[21,63,69,98–100] as well as

HOR in akaline[56]. The EIS spectra at 50mV of overpotential can be observed in Figure 3-4. By fitting our circuit model depicted in Figure 1-9 and using our Pt hydrogen evolution electrode parameters we can calculate the charge transfer resistance.

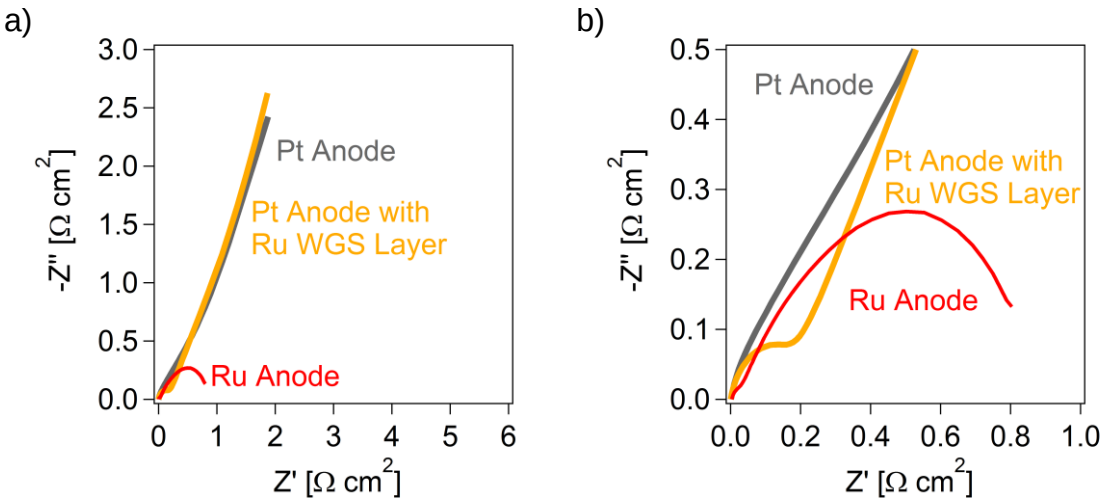

Figure 3-4 EIS spectra collected at 50mV of overpotential acquired in 45% CO balance Ar at 250 °C with 1.05mg/cm² listed anode and 1.05mg/cm² Pt cathode

Assuming an Arrhenius relationship, the activation energy for the CO electrooxidation is determined. This is seen in Figure 3-5 by plotting the log of the geometric exchange current density vs 1/T. An activation energy of 36.7 kJ/mol is found. Low temperature studies of Ru and CO electrooxidation have found lower activation energies of of 30 kJ/mol[63]. We attribute this increase of activation energy to the large decrease in the OH adsorbed onto the catalyst

surface. Note this is in drastic difference with the water gas shift reaction energy for Ru which has been reported as 77.9 and 121 kJ/mol.

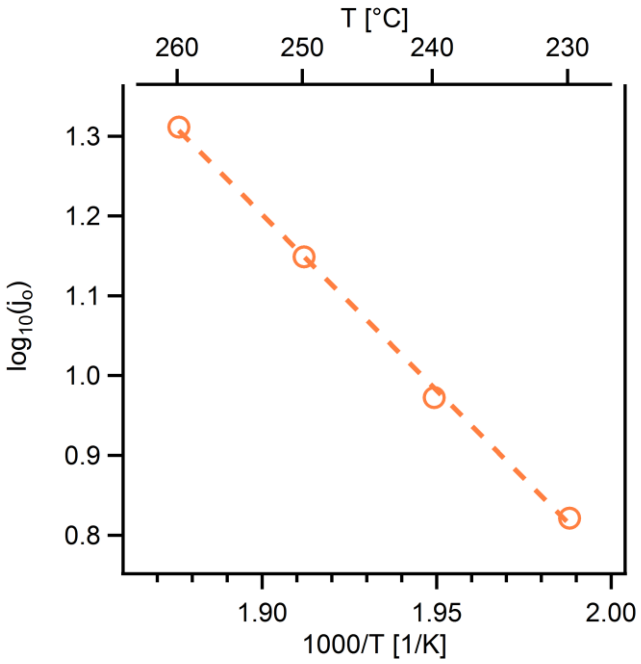

Figure 3-5 Exchange current density versus the inverse of temperature used to calculate the activation energy.

While the reaction mechanism the intermediate CO electrooxidation in solid acid electrolyte system is still undetermined, we suggest the reaction is similar to the low temperature aqueous electrooxidation reaction as opposed to the intermediate temperature water gas shift reaction. We suggest the difference in activation energy is the due to the low relative humidity point at the operational

temperature of 250°C and 75°C dew point. This significantly modifies the OH adsorbate surface coverage compared to the aqueous case.

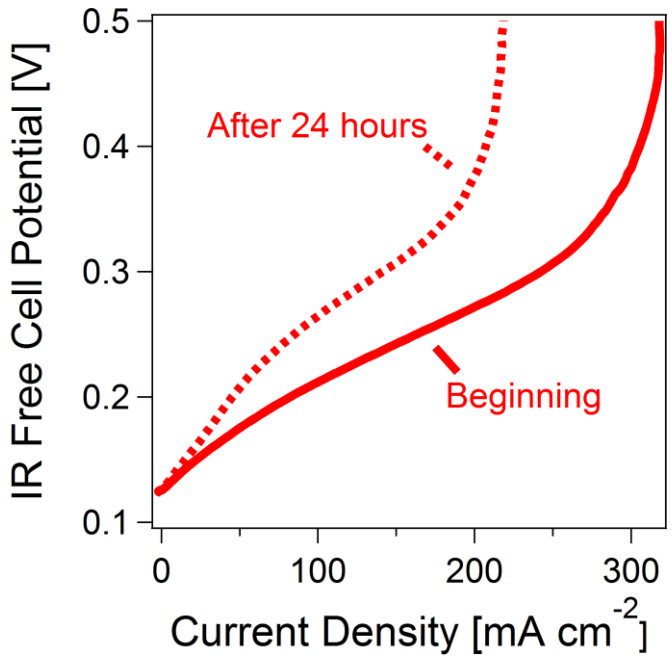

Figure 3-6 iR-free polarization curves acquired in 45% CO balance Ar at 250 °C with 1.05mg/cm² Ru anode and 1.05mg/cm² Pt cathode

Despite having initial high performance, the cell quickly deteriorates. The performance in Figure 3-6 has decreased by roughly 35% in the course of 24 hours. Further investigation of the electrode after testing shows that the performance decrease is linked to the oxidizing of the stainless steel support and test fixture by the formation of rust. Figure 3-7 depicts three cells run in hydrogen, 45% CO for 24 hours and 45% CO for 72 hours.

The reason for the creation of rust most likely stems from the carburization of the steel. This then allows the water to oxidizes with surface iron forming rust[101102]. These micron size particles on the stainless steel are then removed

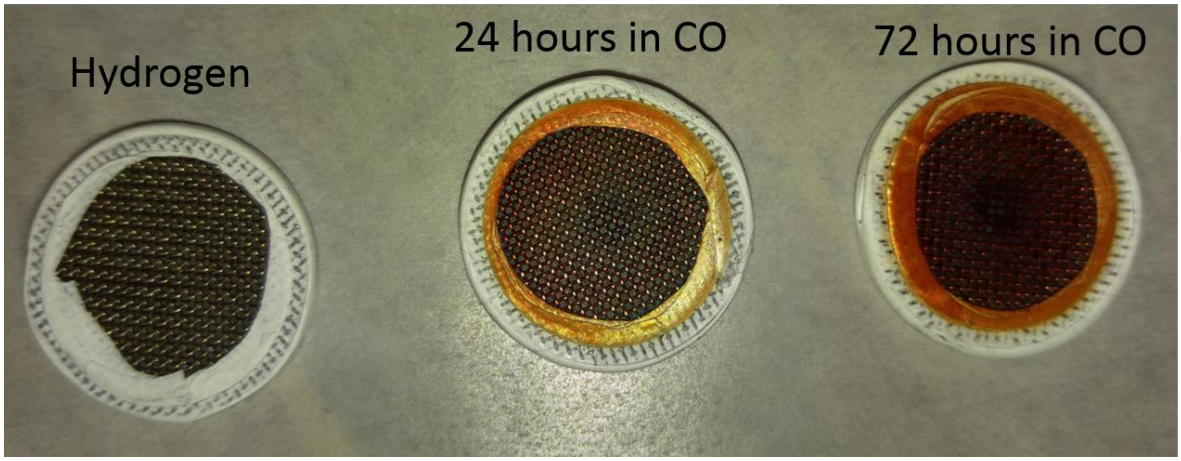

Figure 3-7 Hydrogen separation cells after testing at 250°C in 90% CO balance Ar

from the bulk stainless steel and are blown into the electrode. This clogs the electrode inhibiting gas diffusion as well as reacting with the CDP. This is clearly visible in the SEM image in Figure 3-8.

EDS spectra shows that there are large amounts of iron in the electrode. Iron is only found in our test fixture and as a mechanical support for our MEA structure. CDP has a high reactivity for metal oxides. This has been noted before with the Pd based catalyst used for a cathode catalyst in air fed SAFCs operating at 250°C[57]. Once these iron oxide particles are into our electrode,

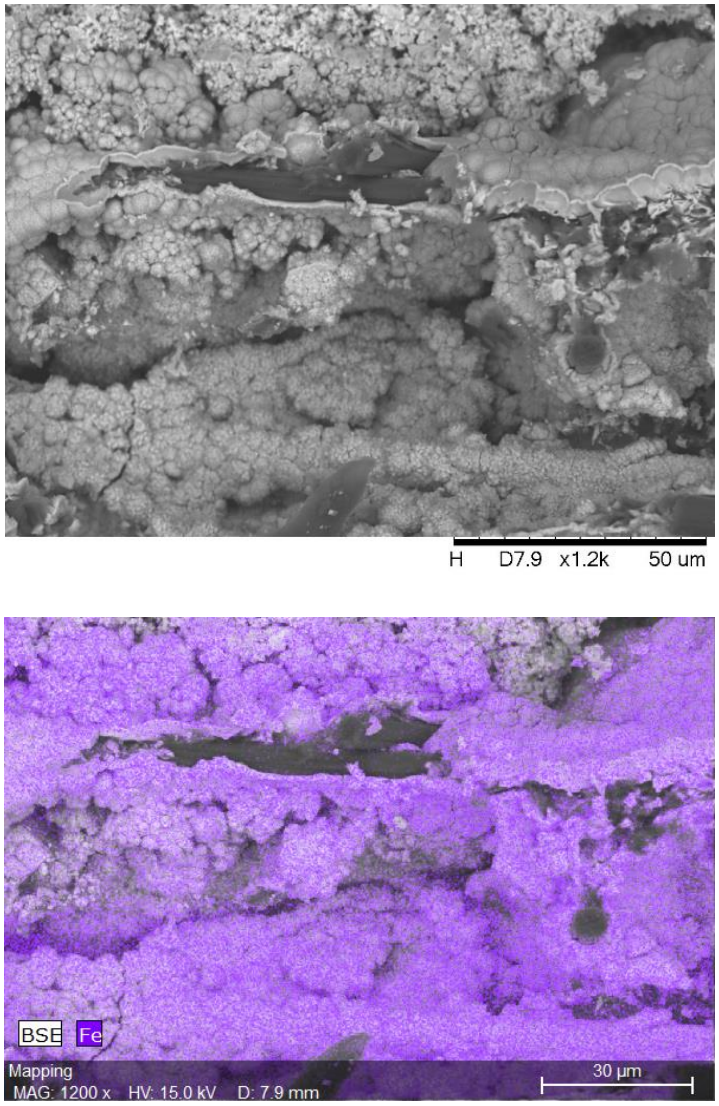

Figure 3-8 TOP: SEM micrographs of Ru anodes after hydrogen separation testing in 90% CO balance Ar at 250°C for 72 hours. BOTTOM: EDS spectra for Fe in the same electrode.

there is not an effective way to remove them. This leads to clogging of the pores in our electrode that is required for gas transport. Without effective gas transport, it is impossible to have stable electrochemical performance. This could also inhibit water transport, thus potentially leading to CDP dehydration.

In order to increase the stability, a thick layer of graphite coating was applied to the test fixture as well as the removal of the stainless steel support. The improvements were noticeable as observed in Figure 3-9.

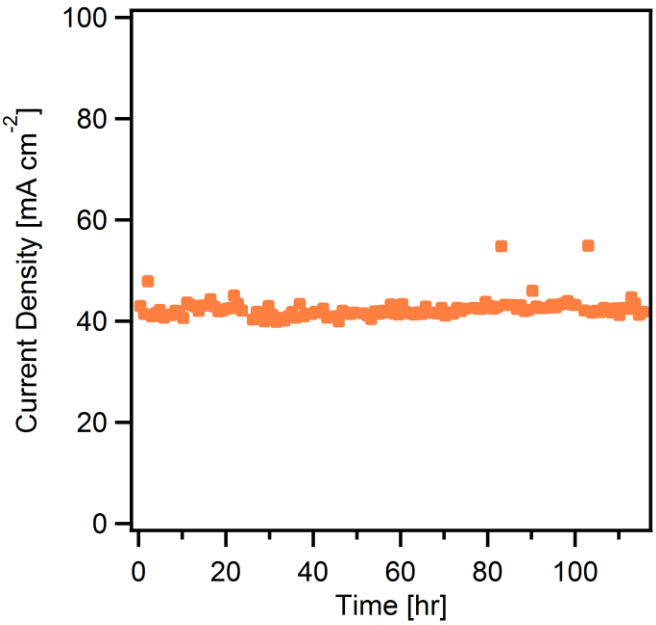

Figure 3-9 CA collected in 90% CO balance Ar at 250 °C with 1.05mg/cm² Ru anode and 1.05mg/cm² Pt cathode

Figure 3-9 was held at 50mV versus the OCV. The deviation from the baseline of 42 mA/cm^2 is due to liquid water vaporizing in the test fixture. This leads to an

unsteady supply of reagents to an electrode leading to deviation from the average behavior. After 115 hours, the current decreased by 1mA/cm^2. However, the cell rapidly deteriorated after 115 hours. This could of possibly been to an electrical short in the cell due to a water droplet.

Figure 3-10 shows iR-free polarization curves acquired at three different CO concentrations, 20%, 45% and 90% balance of Ar. Applying the low field approximation to the Butler-Volmer equation (1-21) we can calculate the geometric exchange current densities to be 41.7, 41.36 and 40.98 mA/cm^2 for 20%, 45% and 90% respectively.

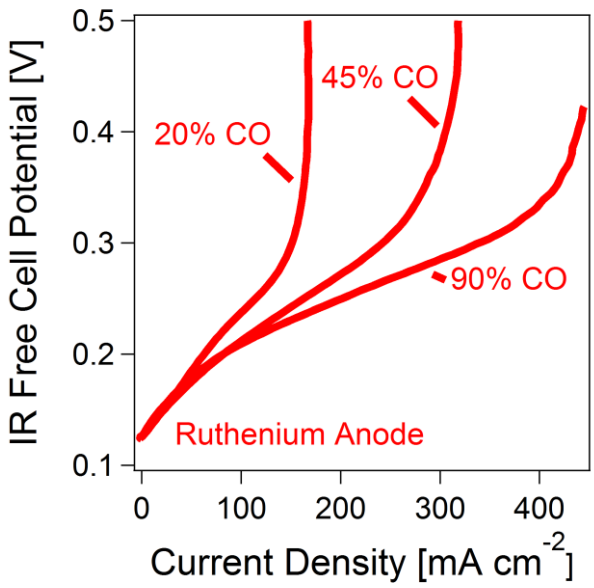

Figure 3-10 iR-free polarization curves acquired in listed percent CO balance Ar at 250 °C with 1.05mg/cm² Ru anode and 1.05mg/cm² Pt cathode

These polarization curves shows a highly mass limiting reaction. In order to investigate if the consumption rate of the CO, an in situ experiment was setup using a GCMS. Figure 3-12shows GCMS data for 90% CO for 6 different overpotentials. The current and time response is shown in Figure 3-11.

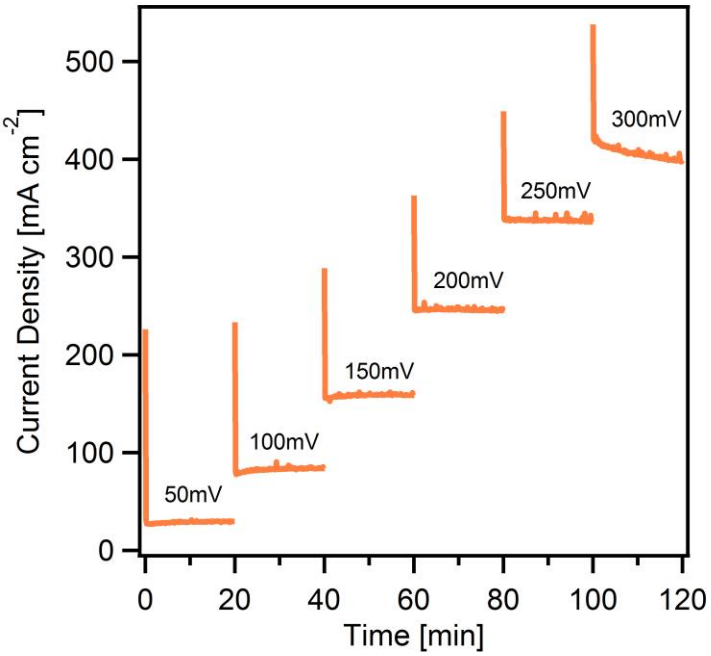

Figure 3-11 CAs collected in 90% CO balance Ar at 250 °C for GCMS analysis with 1.05mg/cm² Ru anode and 1.05mg/cm² Pt cathode

GCMS results were collected at each over potential and also at OCV. These are summarized in Table 3-1 . The anode gas stream upon entry is 90% CO with a balance of Ar. The Ar gas is used as an inert marker gas in order to verify the accuracy of the measurement and should remain 10% throughout the

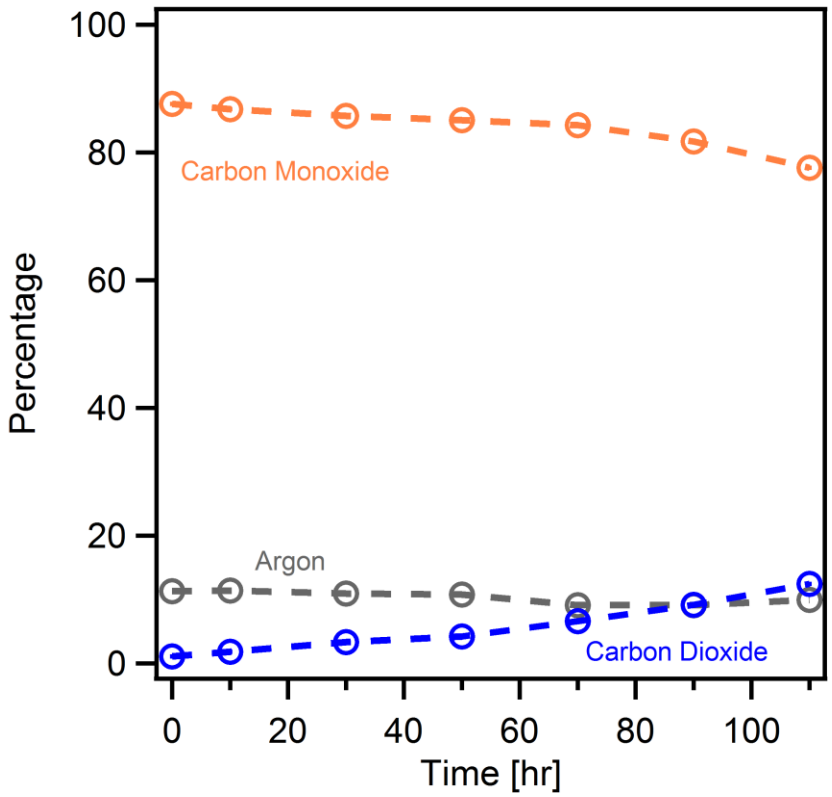

Figure 3-12 GCMS analysis collected from anode outlet with 90% CO balance Ar input after gas drying

experiment. The general trend of percentage decrease of CO to CO_2 increase is as expected for the proposed reaction.

Table 3-1 GCMS analysis collected from anode outlet with 90% CO balance Ar input after gas drying

Overpotential (mV)	Ar (Percent)	CO (Percent)	CO_2 (Percent)
0	11.3	87.59	1.11
50	11.4	86.78	1.82
100	10.94	85.72	3.33
150	10.76	85.03	4.20
200	9.12	84.28	6.60
250	9.13	81.71	9.16
300	9.94	77.58	12.47

By knowing the entry reagent flowrate for 45sccm and the exit percentages, we can use a mass balance and current integration to determine the relative efficiency. At 50mV of overpotential the current density is 29.35 mA/cm^2 and at 250mV, which is the last steady overpotential, the current density is 337.14 mA/cm^2 we can determine the amount of charge per minute by Faraday's constant. In this case we calculate 18.42C. At the same overpotentials, the change in percentage in CO is 5.08% thus leading to a mol

count of 9.2e-5. Assuming the electron number is 2 we calculate the amount of charge to be 17.73C. These calculations serve as a reasonable estimate of the CO electrooxidation but due to the system variability are not be entirely accurate.

Despite the mass transport limiting current response as shown in the polarization curve, we notice that the amount of CO remains relatively high in the outlet of our anode stream. This leads to the conclusion that water may actually be the limiting reagent in our anode reaction. With our current design, it is not possible to increase and vary the partial pressure of water above 0.35 bar. A new system designed to handle higher concentrations of water must be implemented in order to test this hypothesis.

Given the activity and stability of the CO electrooxidation reaction on our ruthenium anodes, we sought to apply this technology to a solid acid fuel cell. The cathode was fabricated using a conformal Pt particle coating on CDP as described in this paper[46]. Figure 3-13 shows fuel cell performance at 250 °C on a feed stream of 90% CO and balance Ar for the anode and air fed to the cathode. Despite the low performance, this proves an interesting design for potential applications in high CO based fuel streams such as those from coal gasification.

Due to the activity of Ru for both HOR and CO, we chose to formulate anodes for other applications in low percentage CO and higher percentage CO_2 feed streams. One prime example is the steam reformation of methanol. These methanol reformate streams contain less than 1% CO on commercial catalysts[32].

Polarization curves for both Pt and Ru based anodes are shown in Figure 3-14 for an in situ MeOH steam reformation system. This graph depicts as-recorded Ru and Pt (control) hydrogen oxidation electrodes under neat hydrogen and methanol using Pt electrode as the cathode. In both hydrogen and methanol, the Pt based anodes are marginally superior to their Ru counterparts.

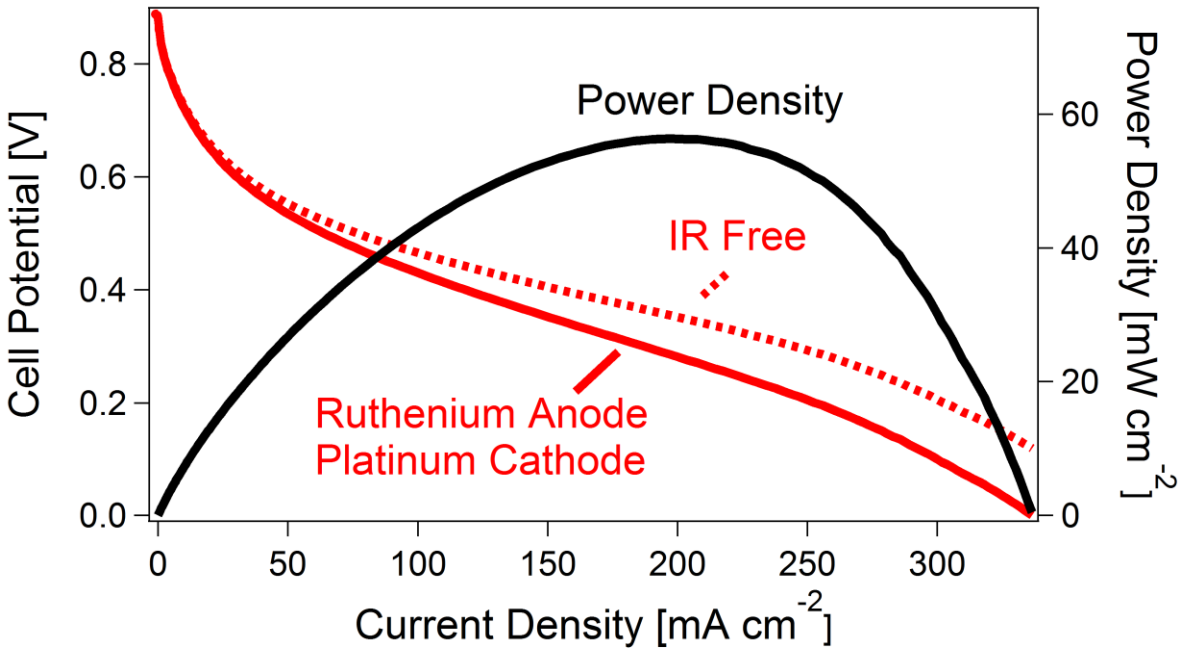

Figure 3-13 Fuel cell polarization curve collected in 90% CO balance Ar at 250 °C with 1.05mg/cm² Ru anode and 1.75mg/cm² Pt cathode

This is shown by the lower cell overpotentials required at any current density. Figure 3.14b shows the IR_{Ω}-free polarization curves for the same curves. The majority of the overpotential is dominated by the ohmic penalty of the membrane

which makes up 54.6% of the loss at -50 mA cm^{-2} in Ru anodes. Both Pt and Ru anode catalyst display a deviation of -10mV from the neat hydrogen OCV when switched over to methanol. We assign this shift to a Nernstian effect of the change in the hydrogen concentration at the anode as a result of the reforming process.

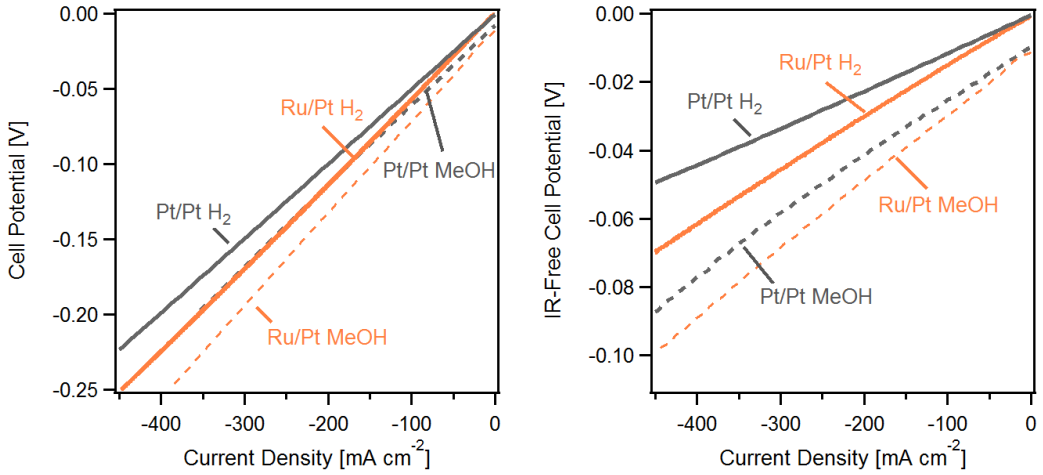

Figure 3-14 Hydrogen evolution polarization uncorrected for IR (a) and corrected for IR (b) for 1.05 mg cm-2 of Pt and Ru anodes on hydrogen and methanol at 250°C and 75°C dew point.

In order to determine the composition of the reformed methanol, in situ GCMS experiments were performed. Figure 3-15 shows the gas chromatography and mass spectrometry of an in situ cell being held at OCV under methanol. For these measurements, nitrogen was replaced with argon as the carrier gas for its molecular weight of 40.

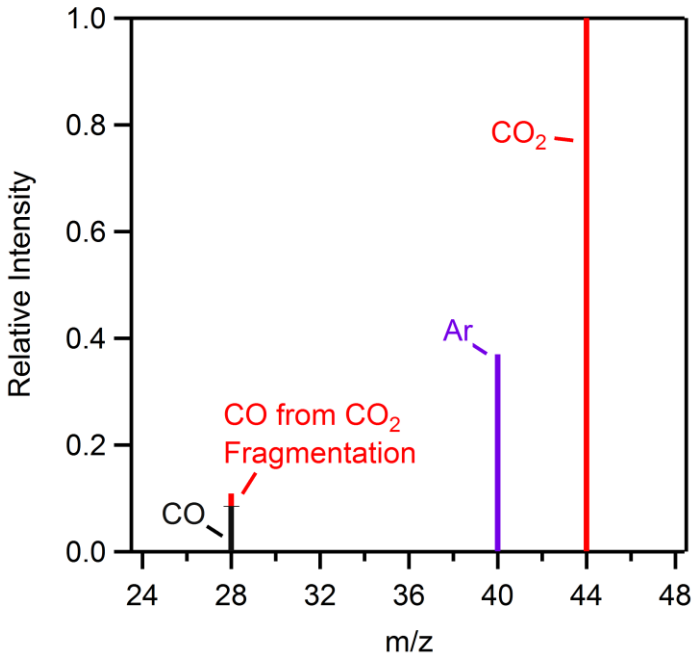

Figure 3-15 Gas chromatography and mass spectrum at OCV of methanol and water reformed in situ.

This aids in the distinction from carbon monoxide and nitrogen in the mass spectrometry results. The ratio of carbon monoxide to carbon dioxide is calculated to be 0.10. This gives similar results to ex situ HiFUEL R120 methanol reforming catalyst at 250°C. Results have been reported at having a carbon monoxide to carbon dioxide ratio of 0.07 with an overall gas composition of 82.3% H_2 16.6% CO_2 and 1.2% CO[84]. The extent of reaction can be defined by ratio of hydrogen produced to the maximum theoretical hydrogen that could be produced:

$$\delta = \frac{H_{2\,Produced}}{H_{2\,Theoretical}} \qquad (3\text{-}1)$$

Where an extent of one represents maximum potential H_2 at a given flow rate from the steam reformation defined in in equation (1-5). Using mass balance calculations for a flow rate of 10sccm of Ar and assuming the extent of reaction to be one, the ratio between argon and carbon dioxide would be 0.40. However, our ratio of argon to carbon dioxide is 0.24. This can be taken a step further to calculate the extent of reaction to 0.58. Finally, an overall mass balance is used to calculate the overall gas composition entering the cell electrode at OCV to 38% H_2, 35.1% H_2O, 12% CO_2, 8.1% MeOH, 6% Ar and >0.8% CO.

In order to determine the effects of potential catalyst poisoning from the reformer, a gas mixture of 38% H_2 and balance of Ar were fed into both a Ru and Pt hydrogen pump cell. Figure 3-16 shows R_Ω free EIS of Pt cell and Figure 3-16b shows R_Ω free Ru cell at -50mV cell potential in both MeOH as well as a 38% H_2 mixed with Ar stream. Figure 3-16a shows negligible difference in the R_{ct} from the mixed gas (0.092 Ω cm^2) to the methanol feed (0.09 Ω cm^2). The R_{ct} for the Ar mixture is slightly higher, but is attributed to the slight variance in cells between constructions. A similar story can be told for 3.16b with the R_{ct} of the mixed gas stream being slightly lower (0.12 Ω cm^2) and the direct methanol being higher at (0.13 Ω cm^2). Previous studies have shown that at higher concentrations of 10% CO, Ru out performs Pt at higher over potentials[36]. In situ methanol steam reformation shows the levels of CO are much lower, which

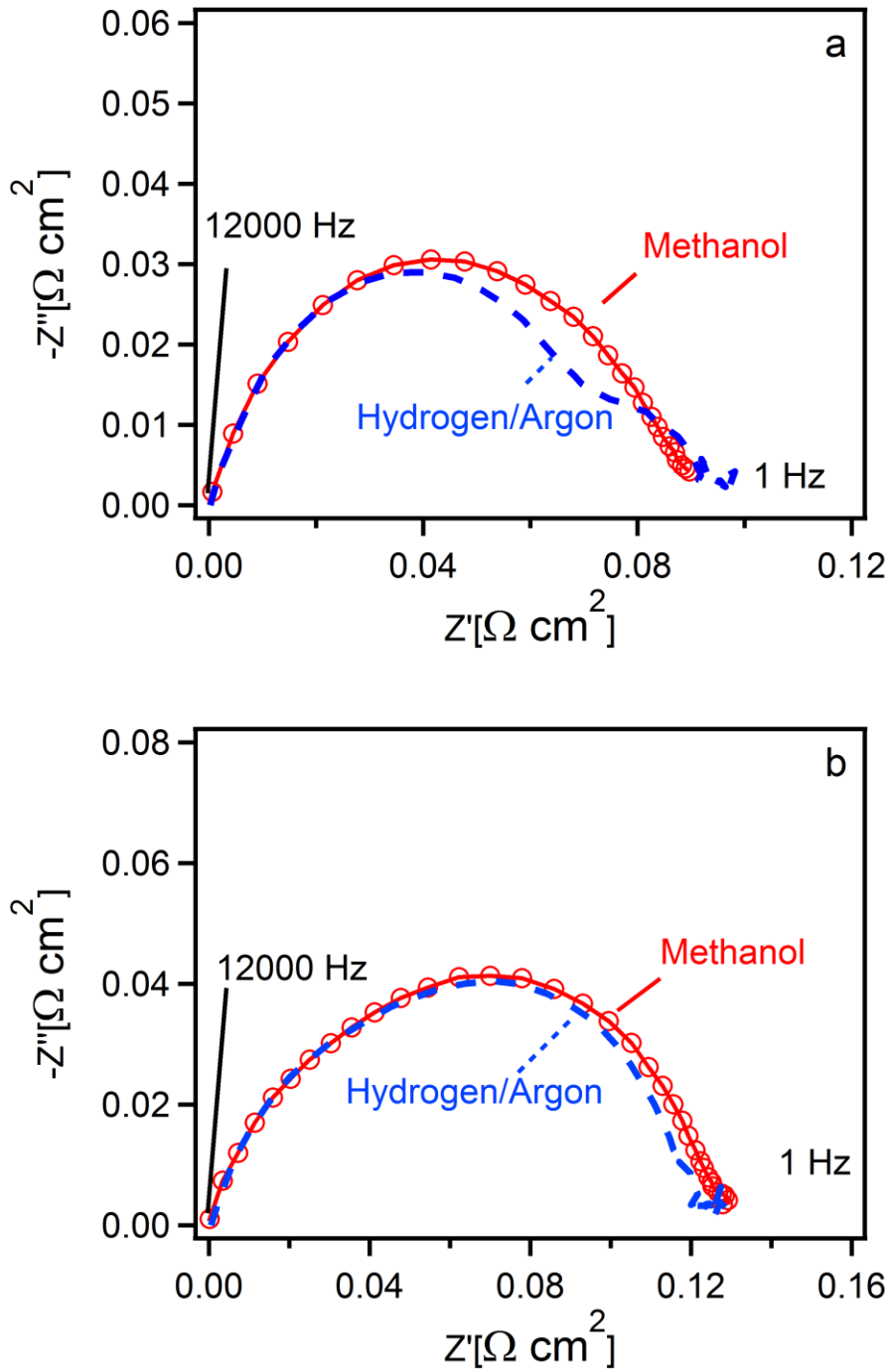

Figure 3-16 iRΩ-Free methanol and hydrogen/argon gas mixtures at 38% hydrogen at -50mV of overpotential. Cells consist 1.05 mg cm-2 of Pt (a) and Ru (b) anodes on hydrogen and methanol at 250°C and 75°C dew point.

explains why Pt is still out performing Ru as an anode catalyst. The excess methanol and CO_2 act as spectators species and do not show any signs of catalyst poisoning. This is determined from the negligible R_{ct} change between the hydrogen and argon streams to methanol. This leads to the conclusion that the performance difference between pure H_2 and the methanol is due to concentration effect. The direct methanol hydrogen pump showed excellent stability at -0.05V as shown in Figure 3-17. The initial increase in cell performance is due to the sintering of the CDP in the membrane.

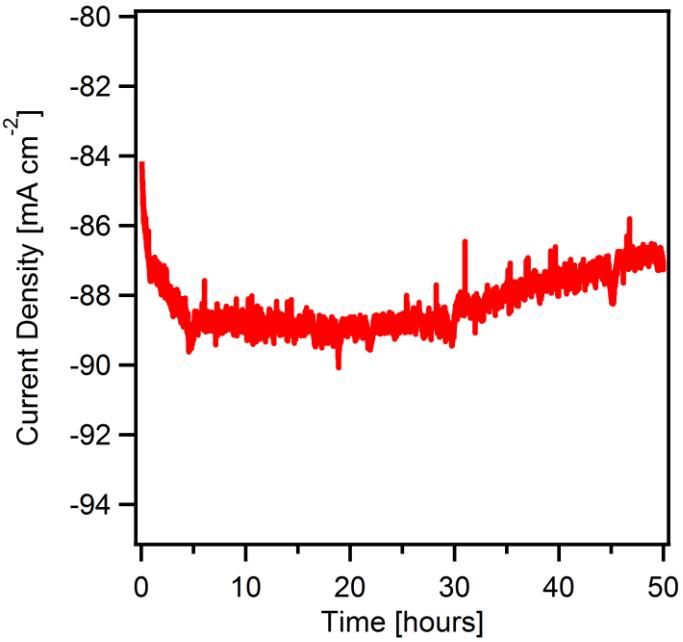

Figure 3-17 Steady state cell of 1.05 mg cm-2 Ru anodes on methanol at 250°C at -50mV of overpotential. Pt cathodes at 1.05 mg cm-2 were used as control electrodes for the hydrogen evolution reaction.

After the cell reaches steady state the cell displayed a net decline in performance of -2 mA cm^{-2} after 50 hours of operation. The decrease is most likely due to the reduction of methanol in the syringe in the syringe pump causing a concentration dilution. This is consistent in showing that the excess methanol does not poison the Ru catalyst during cell operation.

Having demonstrated the effectiveness of the Ru-based anode, we then implemented a Ni-based cathode in the cell assembly. This was in order to create a true Pt-free hydrogen separation system using in situ reformation. Figure 3-18a show as-recorded supported Ru and Ni hydrogen separation systems on both MeOH and neat hydrogen as well as a Pt-Pt control sample on neat hydrogen. Figure 3-18b shows the IR_{Ω}-free polarization curves for the same curves. As with the previous systems, methanol reformed systems have decreased performance than their neat hydrogen counterparts. This is mostly due to the dilution effect of reduced H_2 in the stream as well as the OCV shift. With the addition of the Ni cathode, the ohmic resistance no longer becomes the domination cell parameter. At -50mV of overpotential, the ohmic resistance is 27% of the overall potential loss. At -300 mA cm^{-2} the ohmic resistance is 42% of the overall loss. Despite having less performance than Pt, we must consider the advantages of the Ru/Ni system. The abundance and price of Ni are drastically less than its Pt counterpart. Ru itself is also considerably cheaper metal than Pt which could lead to larger systems built for the same price as their Pt counterparts. The combination of the Ru and Ni electrodes can decrease cell

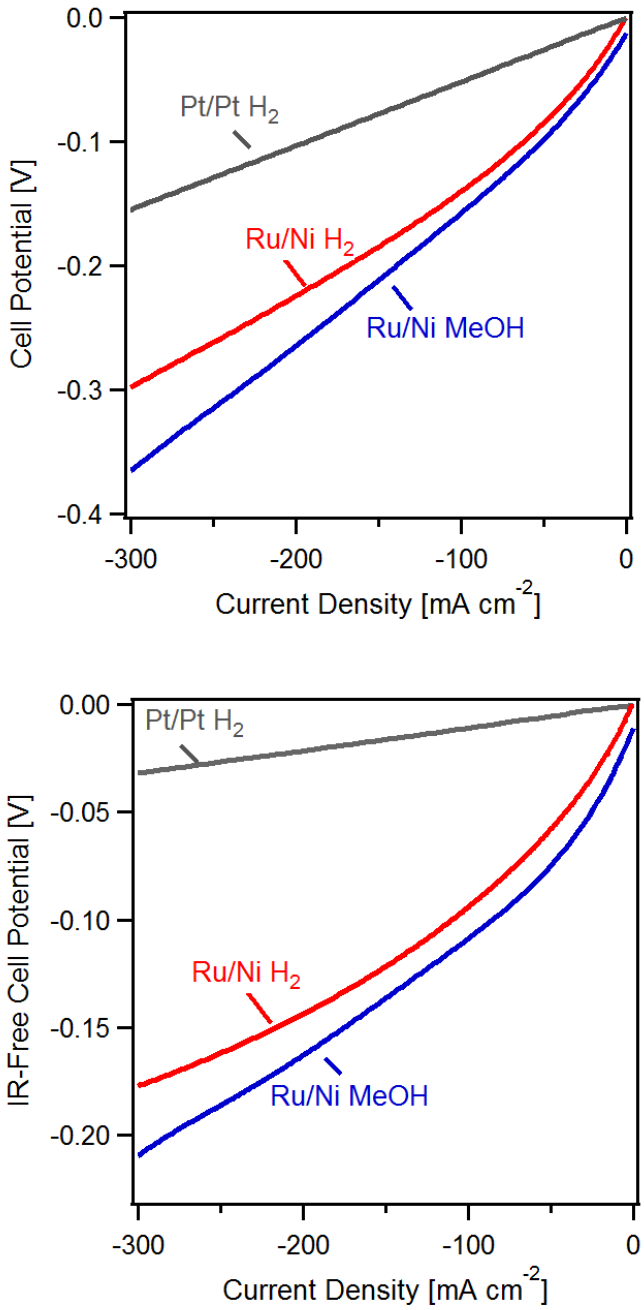

Figure 3-18 Hydrogen evolution polarization uncorrected for IR (a) and corrected for IR (b) for 1.05 mg cm-2 of Ru anodes on hydrogen and methanol at 250°C and 75°C dew point. Ni cathodes at 2.1 mg cm-2 were used as control electrodes for the HER reaction.

fabrication cost by 12. These electrodes can potentially be further optimized as well in order to increase the performance even more. Another point of optimization is the large ohmic losses from the membrane. Reducing the thickness of the membrane from 75 microns would greatly increase the overall system efficiency.

Conclusion

We have demonstrated that methanol can be steamed reformed and the hydrogen separated using an inexpensive solid acid electrolyte and zero Pt at 250°C. Although Ru is not as active as Pt, the metal is considerably less expensive and shows other advantages in the ability to electrooxidize CO. By combining commercial Cu Hi-Fuel catalyst with Ru anodes and with Ni cathodes we have demonstrated a non-Pt hydrogen separation system for CDP based devices operating at 250°C.

CHAPTER 4

MODIFYING ELECTRODE ARCHITECTURES FOR SOLID ACID ELECTROCHEMICAL HYDROGEN SEPARATION DEVICES

Abstract

The solid-state proton conductor cesium dihydrogen phosphate (CsH2PO4 or CDP) has shown potential in electrochemical devices operating on fuels such as reformed NG or methanol. In this work, functionally graded anodes are fabricated to balance CO conversion activity with hydrogen oxidation. Although Ru has shown potential as a hydrogen oxidation catalyst, Pt is still superior. A dual-phase Pt and Ru electrode has been fabricated in order to increase the energy efficiency over a single-metal anode. Various carbon supports have be used in order to increase the triple phase boundary leading to drastically reduced metal loadings. These re-engineered anodes are implemented in conjunction with Ni-based cathodes to demonstrate efficient hydrogen separation using ultra low loadings of Pt from syngas-like inputs.

Introduction

Hydrogen solid acid fuel cells (SAFCs) based on the acid salt CsH_2PO_4 are a relatively new class of devices with the potential for applications in intermediate temperatures of 250°C. These devices have proven advantageous due to zero liquid water management as well as poisoning resistance to impurities from reformed hydrocarbons. While SAFC anodes are robust with

regards to impurity tolerance, the optimization of the active catalyst surface area is still lacking. Original SAFC electrodes were based on bulk mixing of Pt-black with the electrolyte. These original cells[58] showed a peak power density of 415 mW/cm^2 but at large Pt catalyst loadings of 7.5 mg/cm^2.

In order to better optimize the Pt active area, a conformal coating technique was applied to make solid acid electrodes. These electrodes were fabricated by performing a CVD deposition from the metalorganic $Pt(acac)_2$. The electrodes were then further modified with Pd in order to increase performance. These electrodes were found to be unstable due to the reaction with Pd and the CDP electrolyte[57]. Conformally coated electrodes were able to reduce the Pt loading to 1.75 mg/cm^2 while increasing the cell performance[46].

In a recent development, CDP based devices have been applied to electrochemical hydrogen separation. These electrodes employed a carbon support system based on XC72 Vulcan carbon. These carbons were then mechanically mixed to form an electrocatalyst layer, with porosity added by using a fugitive binder, naphthalene. While effective, these electrodes still use rather large amounts of catalyst. In the case of Pt[65], Pd[65], and Ru[36] loadings of 1.05 mg/cm^2 were applied. For Ni[39] electrodes, metal loadings are even higher at 3.5 mg/cm^2.

Carbon based electrodes have also shown promise for cathode optimization. Two types of carbons, multi-walled nanotubes (MWNT) and single-walled nanohorns (SWNH), were applied to SAFC cathodes. These electrodes

showed further improvement relative to the conformal layer electrode, while reducing the Pt loading to 1.3 mg/cm^2. While these electrodes have shown promise for the cathode, we address the anode application of this technology in order to minimize the amount of Pt for the hydrogen oxidation reaction for both applications in fuel cells as well as hydrogen separation devices. We note that the use of carbon-based electrodes in the cathode is fraught with durability issues due to carbon corrosion. However, anode formulations operate a potentials at which carbon corrosion is minimized.

Experimental Methods

CsH_2PO_4 was synthesized by reaction of $CsCO_3$ (Alfa Aesar, 99%) with H_3PO_4 (Alfa Aesar, 85%) followed by precipitation in methanol and drying. The as-synthesized CDP was low-energy ball-milled to reduce its initial particle size, yielding a fine particulate powder with a BET surface area of approximately 2 m^2/g. Carbon-supported metallic nanoparticles were synthesized as hydrogen oxidation and evolution catalysts. Platinum, ruthenium, and nickel nanoparticles were deposited onto Vulcan XC-72R via a vapor-phase decomposition from their respective metal acetylacetonates $Pt(acac)_2$ (Strem Chemical), $Ru(acac)_3$ (Sigma-Aldrich), and $Ni(acac)_2$ (Alfa Aesar). These reactions were carried out using a fixed bed wherein the crystalline solid precursors were mechanically mixed with the Vulcan XC-72R carbon, in a N_2-water vapor atmosphere at

elevated temperatures via a method that we have demonstrated previously[36,46,52,56,66,67]. The ultimate deposition temperature varied for each species deposited, from 210 °C (platinum) to 240 °C (ruthenium and nickel). The carbon-supported nickel samples was further heat treated at 500°C under N_2 for 3 hours in flowing N_2. HCP Ni was synthesized by drying to $Ni(acac)_2$ and performing the same vapor deposition with a final temperature of 260°C. All Ni electrodes were fabricated by heat treatment of 50 mg of Ni nanoparticles (Sigma-Aldrich, <99% P/N 577995) at 500°C under N_2 for 3 hours in flowing N_2. Aqueous CDP was then deposited into the electrode by room temperature drying. All catalysts were characterized with using X-ray diffraction (XRD) (Philips X'Pert, l ¼ 0.1541874 nm). The position and width of diffraction peaks were obtained by fitting to Voight functions using IGOR Pro (Wavemetrics, Inc.).

Composite electrocatalyst powders were synthesized by dry-grinding the fine CDP with the various metal/carbon catalyst and naphthalene (a fugitive binder). These mixtures kept the mass ratio of CDP, naphthalene and carbon to 3: 1: 0.4 (mass) allowing for variation of the electrode catalyst mass without modifying the electrode thickness. Multiwall nanotubes were fabricated via an aqueous CDP water evaporation followed by the catalyst deposition. Hydrogen pump membrane-electrode assemblies (MEAs) were then fabricated using these electrocatalysts by lamination of active layers in a 2.85 cm^2 diameter hardened steel die. Stainless steel mesh was used for current collector and PTFE tape for a sealant. Each MEA had a membrane thickness of approximately 75 to 85

microns. The mass of a given electrode varied between 22 to 28 mg dependent on the metal loading on the carbon support. In each cell, the hydrogen evolution electrode was laminated at 125 MPa while the hydrogen oxidation electrode was laminated at 25 MPa. The cell assembly was installed in a stainless steel fixture for testing.

Prior to electrochemical testing, the cell assembly was heated to 150 °C in dry Ar. Both electrodes were then switched to a wet Ar purge at 75 °C dew point and heated to the testing temperature of 250 °C.

Electrochemical testing was conducted at 250 °C. At the start of the experiment, each electrode was supplied 30 sccm of humidified ultrahigh purity hydrogen at a 75 °C dew point. Polarization curves were recorded at 1 hour intervals with a Bio-Logic VSP potentiostat by scanning the working electrode potential at 5 mV s^{-1} from the open circuit voltage (OCV) to -0.3 V then to 0.3V. Potentiostatic electrochemical impedance spectroscopy (PEIS) spectra were also recorded at -50 mV versus OCV in a frequency range from 200 kHz to 200 mHz with a single sine perturbation amplitude of 10 mV. Polarization curves free of the ohmic losses due to membrane resistance were derived by the subtraction of the current multiplied by the high frequency resistance measured at OCV. Cells were held at -50 mV for 1 hour between testing cycles.

Imaging of electrodes and chemical analysis was conducted with a Hitachi TM3000 SEM equipped with a Bruker Quantax EDS system operating at 15 kV. High resolution SEM used LEO 1525, 3 kV accelerating voltage.

Results and Discussion

As demonstrated in our previous work, Ru has shown promise as a HOR and HER catalyst as well as a CO electrooxidation catalyst for our solid acid hydrogen separation system. The electrodes consisted of 1.05 mg/cm^2 of catalyst supported on Vulcan XC72 and mechanically mixed with CDP and a fugitive binder naphthalene. Such metal loadings are quite high for such a facile reaction as the HER. Recall that we previously showed in chapter 2 that Ru was slightly more efficient for the HER reaction than for the HOR reaction. A suite of catalysts with metal loadings varying from 0.01 to 1.05 mg/cm^2 was synthesized for determining the effect of catalyst loading in our current electrode structure. Unfortunately due to the catalytic effect of Ru on carbon in air, metal loadings above 60% on carbon will combust. This limits the maximum Ru loading on carbon to 1.05 mg/cm^2 for our XC72 mechanical mixed electrode.

As-recorded and iR-free polarization curves for the Pt-Ru MEA acquired in pure H_2 at 250 °C are shown in Figure 4-1 and Figure 4-2 for hydrogen oxidation and hydrogen evolution. The curves for the higher metal loading of 1.05 mg/cm^2 are relatively symmetric and the dominant loss channel is ohmic, accounting for over 70% of the total losses in the cell. However, as the metal loading decreases, the symmetry disappears rapidly. For the HOR, limiting current densities of 375 mA/cm^2 , 190 mA/cm^2, and 100 mA/cm^2 were found for 10%, 5% and 1% Ru metal on XC72 respectively.

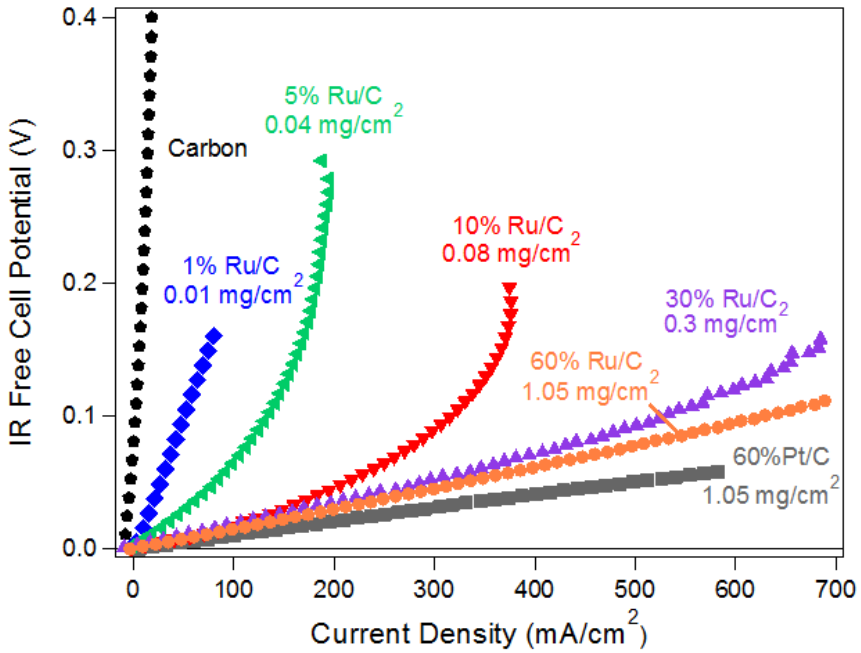

Figure 4-1 iR-free polarization curves acquired in hydrogen at 250 °C with variable Ru anode and 1.05mg/cm² Pt cathode

We must note the mass transport limiting cases in the low loadings of Ru catalyst for HOR. The mass transport of the hydrogen to the relatively dilute supported catalyst is leading to the limiting current that is observed. This is also exacerbated by the lack of electrode optimization for maximizing the three-phase interfaces.

The HER reaction, at the same metal loadings, shows a drastically different trend in Figure 4-2. We do not observe any limiting current for HER. 60% and 30% Ru have similar HER performance to that of Pt, while 10% Ru remains comparable even with a metal reduction factor of 13. The lower

loadings show a difference in performance, with a metal reduction of 2 leading to almost double the polarization required. At the lowest loading of Ru, hydrogen evolution is still maintained and even with no metal, XC72 shows some activity at higher overpotentials.

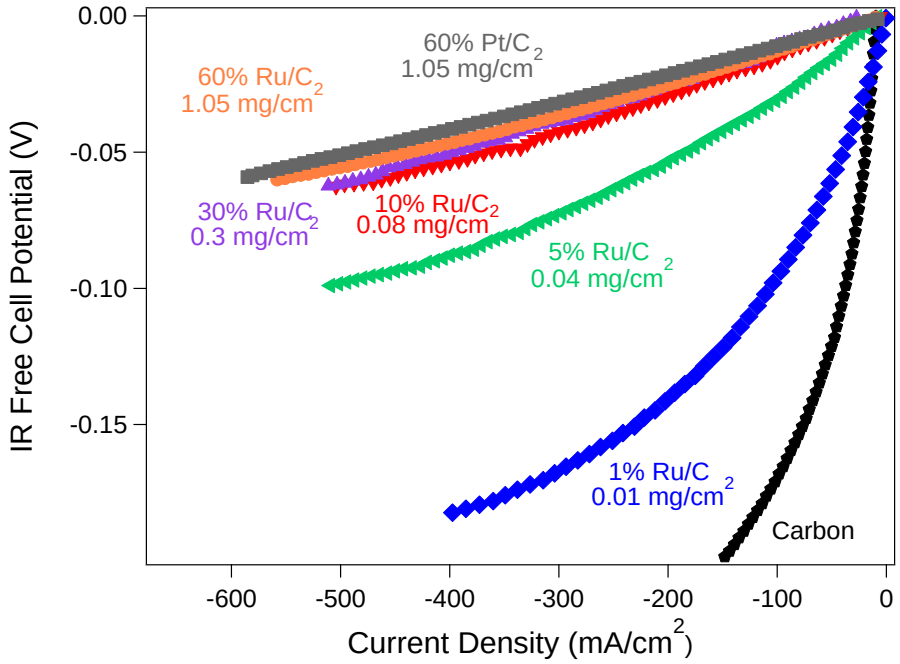

Figure 4-2 iR-free polarization curves acquired in hydrogen at 250 °C with variable Ru cathode and 1.05mg/cm² Pt anode

We know from chapter 2 that Ru is slightly a more active catalyst for HER than for HOR. While this is a contributing factor, the mass transport for a hydrogen evolution reaction is limited to two phases (proton and electron) instead

of three. This aids in reducing the loss due to mass transport thus increasing the performance.

The disparity can be better observed by picking an arbitrary potential away from OCV. In this case we chose to select 60mV and examine the two electrodes. This is shown in Figure 4-3

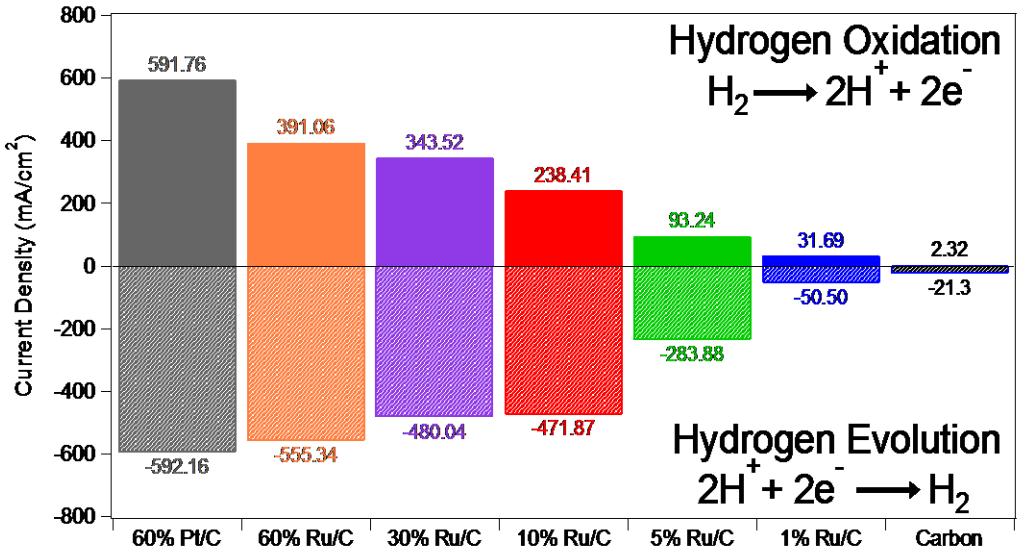

Figure 4-3 Current density taken at 60mV of overpotential at 250°C in hydrogen comparing HOR to HER for Ru electrodes

From Figure 4-3 it is clear to see that Ru metal loadings can be reduced on the cathode and maintain high performance. However the anode may need more metal in order to perform as an efficient electrode. This implies the need for thin catalyst layers with high weight percent Ru, Unfortunately, due to the

reactivity of Ru metal loadings greater than 60% in air, another electrode structure must be explored.

Conformal Pt coatings have shown success in the cathodic ORR reaction in solid acid fuel cell devices. However, the large amount of Pt required (1.75 mg/cm^2) makes it an underwhelming choice for a Pt hydrogen separation system. Ruthenium however has a much lower cost thus allows us for a reasonable electrode cost with the relatively high metal amount needed for conformal coatings. Ruthenium conformal coatings were deposited onto CDP via a vapor-phase decomposition from $Ru(acac)_3$ These reactions were carried out using a fixed bed wherein the crystalline solid precursors were mechanically mixed with the CDP, in a N_2-water vapor atmosphere at elevated temperatures via a method that we have demonstrated previously[52,56,68]. The ultimate deposition temperature was 240 °C. Figure 4-4 shows CDP with conformal coating of Ru particles as synthesized from our one step vapor deposition.

This powder was then laminated directly onto the membrane, similarly to what was done with Pt and Pd conformal coatings on CDP[57]. As-recorded and iR-free polarization curves for the Pt and Ru on CDP MEA acquired in pure H_2 at 250 °C are shown in Figure 4-5 for hydrogen oxidation and hydrogen evolution. While the first cycle seems promising, the cell rapidly decays to a non-functional cell in a matter of 2, 30 minute cycles. Ru on carbon has shown excellent stability in hydrogen environments as previously reported[36]. In order to

a)

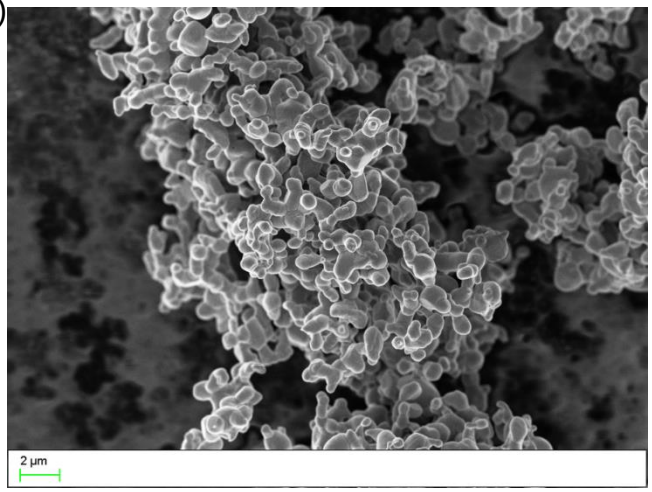

b)

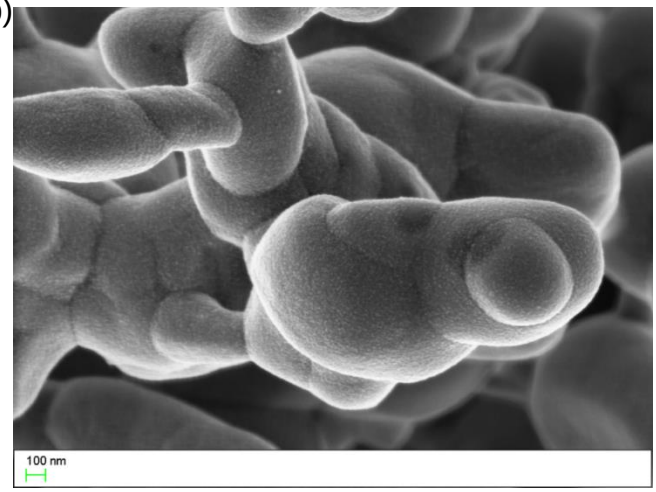

Figure 4-4 As synthesized conformal coatings for 13%Ru on CDP via single step CVD onto CDP

investigate this rapid cell degradation, we analyzed the electrode structure after cell testing.

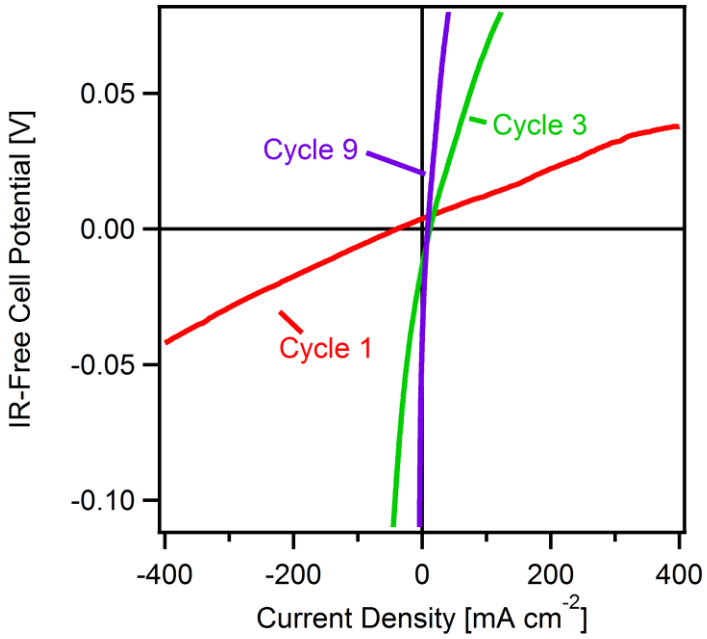

Figure 4-5 iR-free polarization curves acquired in hydrogen at 250 °C with variable conformal coatings of Ru on CDP and 1.05mg/cm² Pt anode.

SEM analysis is shown in Figure 4-6 shows the rapid rearrangement of the conformal coatings to form large particles, thus hindering conduction through the electronic network. Similar effects have been seen with conformal coatings of Pd as well[57]. These Ru particles could possibly be reacting with the CDP, but due to the nature of the electrode containing only hydrogen and water, we do not suggest this. It is possible that the Ru from the chemical vapor deposition reaction without the presence of a carbon support could form an oxide instead of

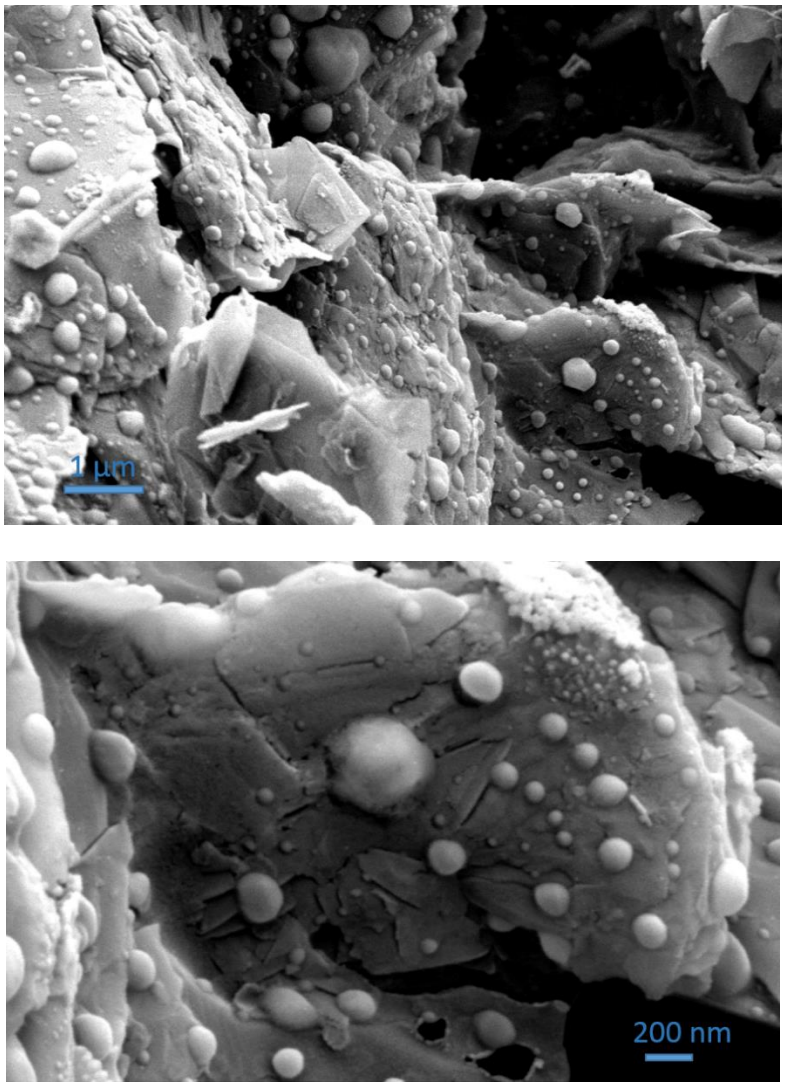

Figure 4-6 Post cell electrode for 13%Ru on CDP

the metal. Pd-O species have shown reactivity with CDP[57] so we expect Ru-O to have a similar effect. However, as noted previously, there are not any other methods of CVD that deposits uniform conformal coatings as this technique[46]. In an analogous process to our Ru loadings study, we applied the same approach to preparing and optimizing Ni electrodes. Unlike Ru, Ni does not cause combustion of carbon with metal loadings higher than 60% so were able to determine the limiting weight limit at which our electrode becomes saturated with catalyst. This amount was found to be 75% by mass Ni supported on carbon. Decreasing the amount of Ni showed a large decrease in performance. IR-free polarization curves for the Pt-Ru MEA acquired in pure H_2 at 250 °C are shown in Figure 4-7.

While we discuss more of the possible Ni mechanics in chapter 2, the asymmetry in the rate of the HOR/HER could possibly indicate a different mechanism between the two. For the HOR reaction, the charge transfer resistance increases with over potential, possibly indicating poisoning of binding sites or mass transport limitation. For the HER reaction, the charge transfer resistance decreases with overpotential. In low temperature studies, Ni reactions tend to be limited by the electrochemical desorption step of H_{ads}.[80,103]

Preferential crystal phases for electrochemical reactions have been demonstrated in the past for various electrochemical reactions. HCP Ni has also been shown to have a hydrogen storage properties in the metastable crystal

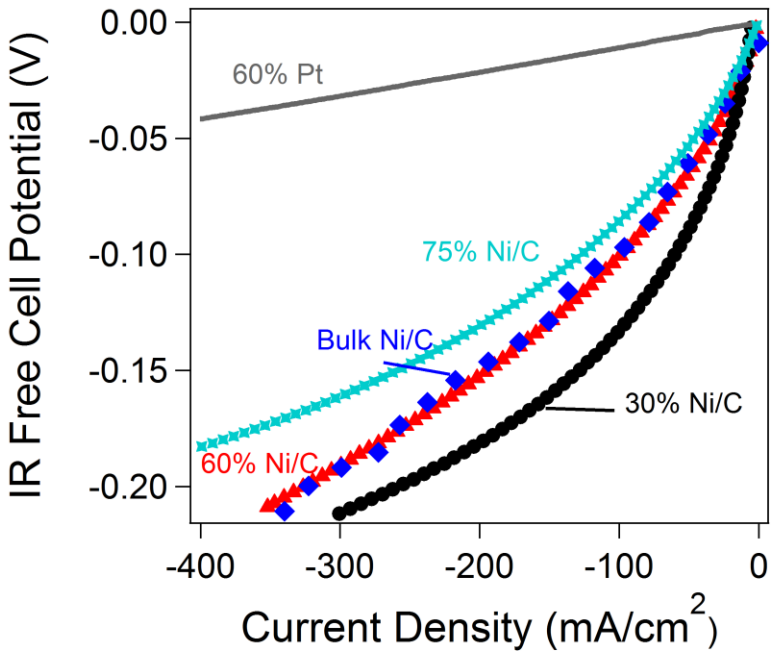

Figure 4-7 iR-free polarization curves acquired in hydrogen at 250 °C with variable Ni cathode and 1.05mg/cm² Pt anode

phase[104]. Ni nanoparticles were deposited onto Vulcan XC-72R via a vapor-phase decomposition from its respective metal acetylacetonate $Ni(acac)_2$ after drying for 48 hours in a dry box. These reactions were carried out using a fixed bed wherein the crystalline solid precursors were mechanically mixed with the Vulcan XC-72R carbon, in a N_2-water vapor atmosphere at elevated temperatures via a method that we have demonstrated previously[52,56,68]. The ultimate deposition temperature was 260 °C. These two modifications yielded HCP Ni over FCC Ni. HCP Ni is normally a very complicated synthesis[105–107], but we have found a simple one step procedure. By heat treating this supported Ni

HCP Ni at 500°C for 3 hours, we were able to revert the HCP Ni to FCC Ni. HCP Ni is known to form due to carbon or hydrogen impurities in the crystal structure, thus the heat treatment reverting to FCC Ni could result in the removal of these impurities. The XRD diffraction results for as synthesized HCP Ni and are shown in Figure 4-8.

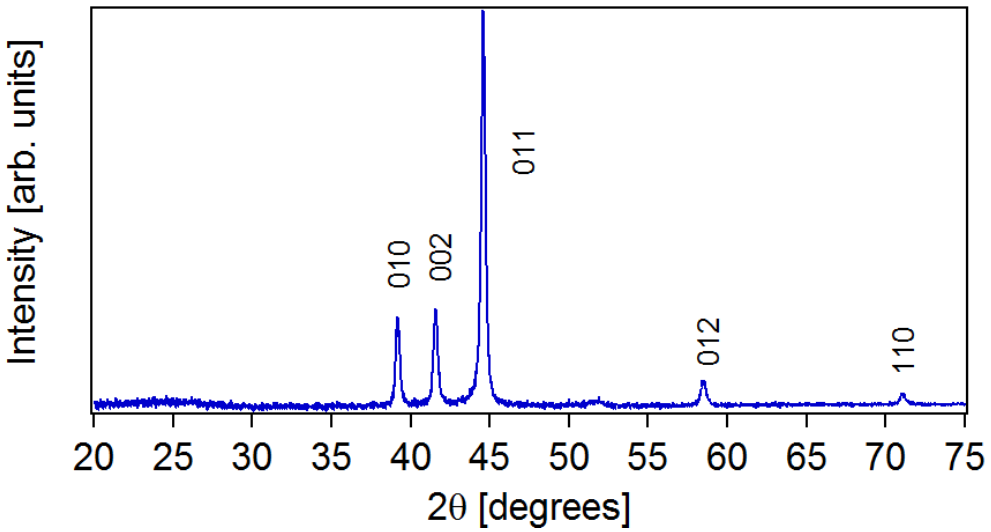

Figure 4-8 XRD with Scherrer analysis of {011} peak showing a d-spacing of 2.034 Å and mean grainsize of 34 nm.

From use of the Scherrer equation the mean particle size are found to be 34nm. While the FCC nanoparticles are slightly smaller at 31 nm, the 34nm particles show an increase in performance as shown in Figure 4-9. This could have potential implications for improved catalytics based on the HCP structure.

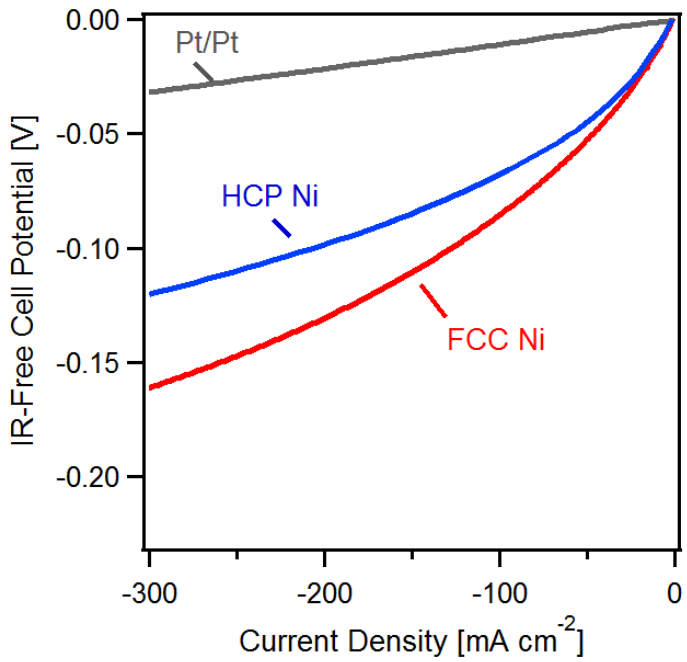

Figure 4-9 iR-free polarization curves acquired in hydrogen at 250 °C with variable 2.1 mg/cm² Ni cathode and 1.05mg/cm² Pt anode

Using the low field approximation we estimate the geometric exchange current density to be 32.0 mA/cm^2 for the HCP nickel and 27.3 mA/cm^2 for the FCC nickel. This is based off the charge transfer coefficient found at OCV. Future studies need to be conducted on HCP Ni in a more controlled environment in order to determine the true effect of the crystal effect for HER. Figure 4-10 shows an EIS spectra collected at 50mV of overpotential.

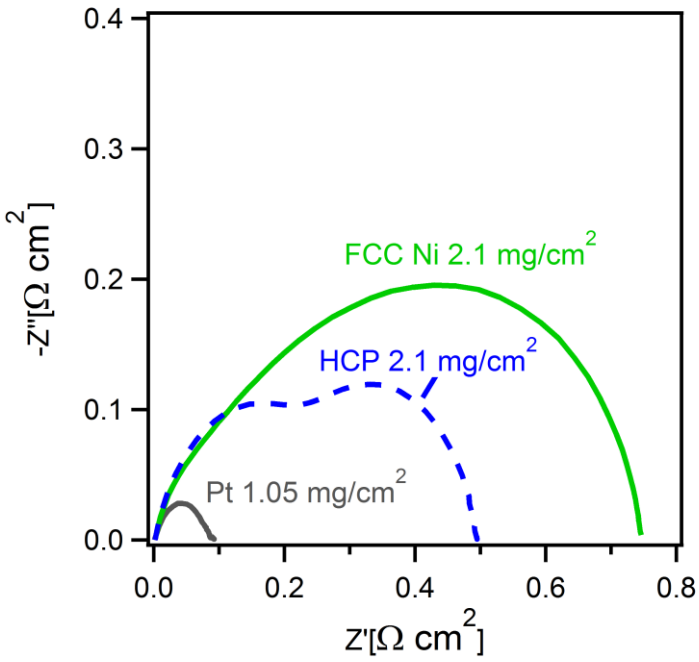

Figure 4-10 EIS spectra collected at 50mV in hydrogen at 250°C for Ni electrodes

Unfortunately interpreting this second arc for our system is complicated due to the number of variables in our experimental setup. We could speculate that due to the change in crystal phase, the activation energy for HCP Ni to accept a proton could be lower. HCP Ni has very little experimentation for catalysis for the HER reaction and a more rigorous study would need to be carried out in order to quantify the reasoning for the increased performance. Normalizing to the electrode catalyst surface area bound by the ECSA for aqueous environments and the electrolyte surface area, we find an exchange current density of 2.09-7.13 mA/cm^2.

Due to the low cost of Ni we can also consider other approaches to electrode synthesis. Due to the large size of the Ni nanoparticles, conformal coats on CDP are not achievable. However we can apply this technique of using the catalyst as an electron carrier in a different way. By using Ni FCC nanoparticles from Alfa-Aesar (Sigma-Aldrich,>99%, P/N 577995, lot MKBK8685V) at 500 °C in N_2 for 3 hours, a porous interconnected “sponge” is synthesized as seen in Figure 4-11.

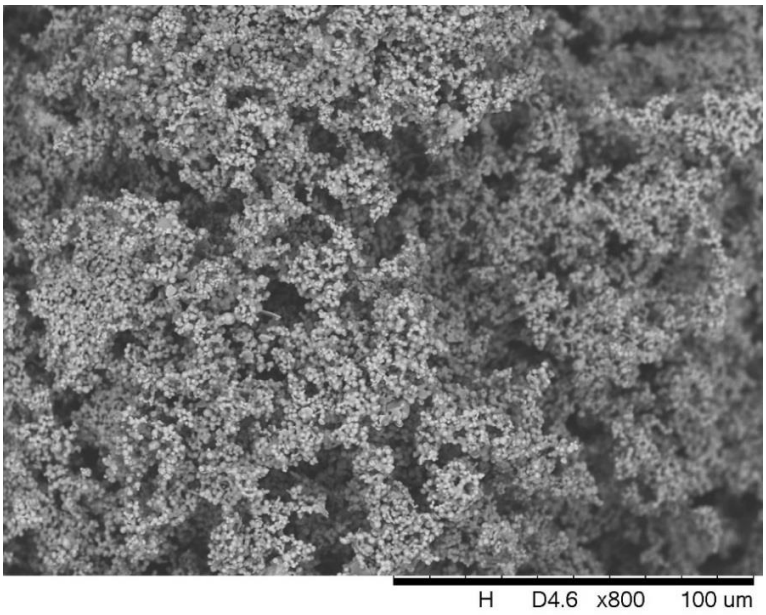

Figure 4-11 Ni sponge as synthesized via as received Ni nanoparticles at 500°C for 3 hours in nitrogen

This electrode sponge is then saturated with CDP by first dissolving CDP in water and adding this aqueous solution to the sponge. This was repeated until

excess CDP was observed on all sides of the electrode. Once saturated, this electrode was laminated directly onto the surface of the MEA as seen in Figure 4-12.

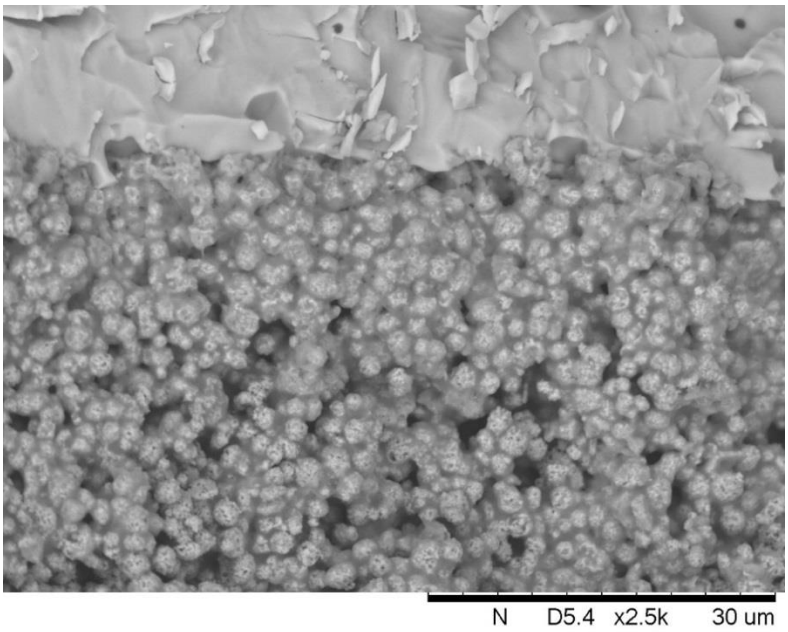

Figure 4-12 Ni sponge as synthesized via as received Ni nanoparticles at 500°C for 3 hours in nitrogen after CDP has been added and the electrode has been laminated to the membrane

These electrodes show limited activity at first (Figure 4-13) but by taking advantage of the HER reaction mechanics, a potential can be applied in order to induce porosity into the electrode. By applying a large enough potential (0.4V) we can take advantage of CDPs super plasticity to locally evolve hydrogen. This

could potentially pressurize the electrode forcing pores in the CDP, or by forcing CDP to creep, which has been shown to be quite trivial to achieve[58].

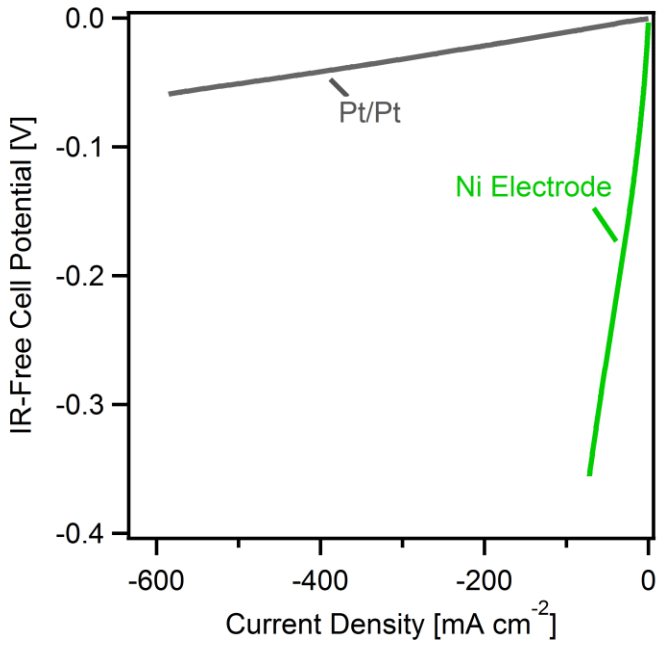

Figure 4-13 iR-free polarization curves acquired in hydrogen at 250 °C with a Ni sponge cathode and 1.05mg/cm² Pt anode at the start of the experiments.

The potential sequence applied can be seen in Figure 4-14. At lower potentials of 0.1V there is relatively little change in the current response. However, when the overpotential is increased to 0.4V, there is a rapid increase in current density, eventually flattening out after 7 minutes.

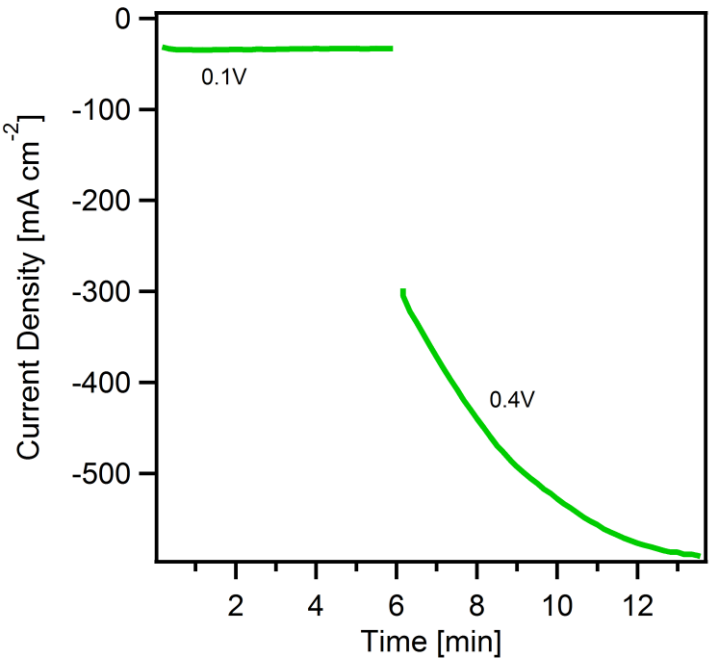

Figure 4-14 CA acquired in hydrogen at 250 °C with Ni sponge cathode and 1.05mg/cm² Pt anode. This overpotential was used to induce porosity into the cathode.

Observation of an iR-free polarization curve on the same electrode is shown in Figure 4-15. At lower overpotentials, the HCP carbon supported catalyst shows better performance. However as the potential increases the fabricated all Ni electrode shows an increase in performance. The carbon supported FCC Ni has lower performance throughout the polarization curve. This stresses the importance of increasing the tri-phase boundary of the electrode to increase the cell performance.

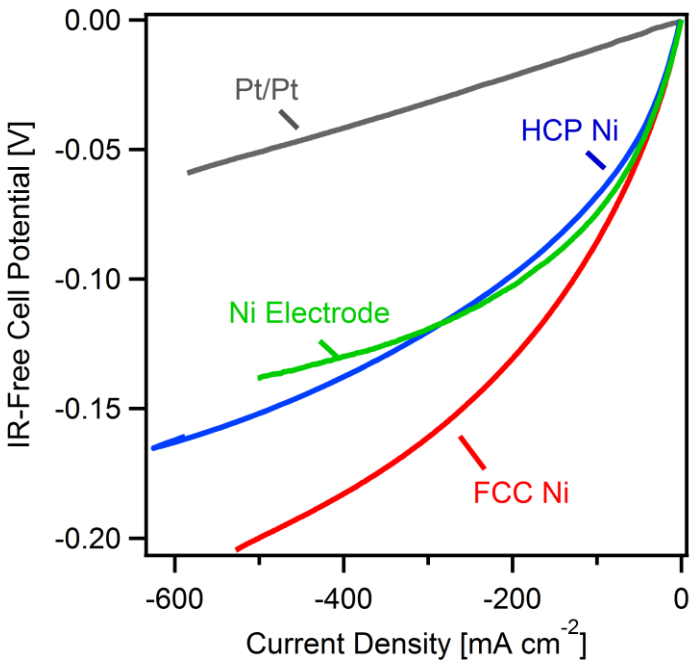

Figure 4-15 iR-free polarization curves acquired in hydrogen at 250 °C with variable Ni cathodes and 1.05mg/cm² Pt anode

While Ru and Ni have shown promise for potential catalysts for solid acid hydrogen separation systems, Pt currently is the most effective catalyst. An alternative strategy to maintaining performance and reducing overall cost is reducing the amount of Pt to low loadings. In order to increase Pt utilization, we will need to increase the amount of the three phase interface. Maximizing the catalyst-electrolyte interfacial area has been a daunting problem in solid acid electrochemical devices since implementation[58]. In order to further optimize the tri-phase boundary for HOR we will try approaching the problem with a new carbon structure different from the mechanical mixing process of using Vulcan

XC72. As a first stage of testing, symmetric cells using Vulcan-XC72 carbon and various loadings of Pt nanoparticles were tested in order to determine if a simple reduction in Pt loading could maintain performance. This is shown in Figure 4-16

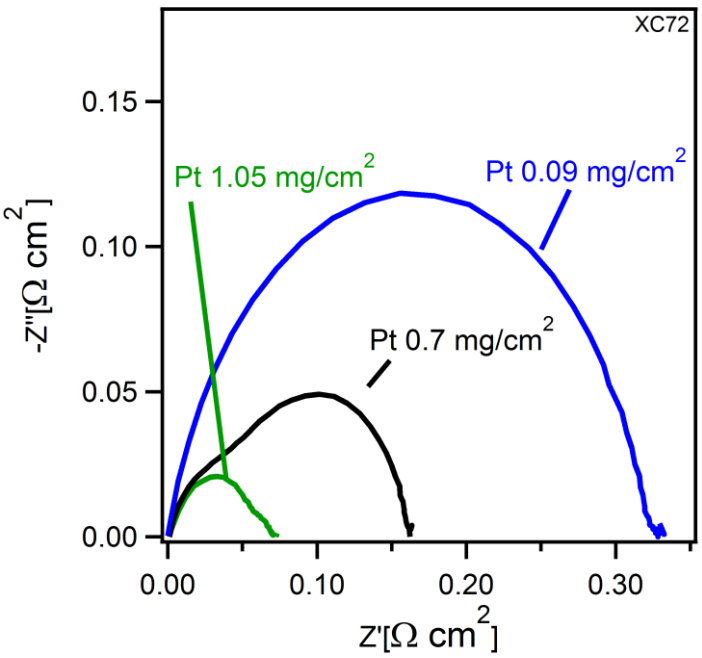

Figure 4-16 EIS at OCV of Pt loadings on XC72-Vulcan carbon

As seen in Figure 4-16, lowering the Pt loading in the electrode drastically reduces performance of the cells for this electrode construct.

In solid acid fuel cell cathodes, using higher surface area carbons such as single walled nanohorns (SWNH) can increase the performance. The SWNHs reveal a structure consisting of individual cone-shaped nanohorns with walls consisting of a single graphene layer and diameters of approximately 2 nm and

lengths of approximately 10 nm, clustered into a secondary dahlia-like aggregate structure. MWNTs also contained approximately 1 wt% encapsulated Co remnant from CVD synthesis. SAFC electrodes were then fabricated by 3:1 (by mass) mixture of carbon supported Pt nanoparticles and CDP. The electrode thicknesses remained constant at 35 microns[108]. EIS spectra was collected at OCV for the SWNH are shown in Figure 4-17.

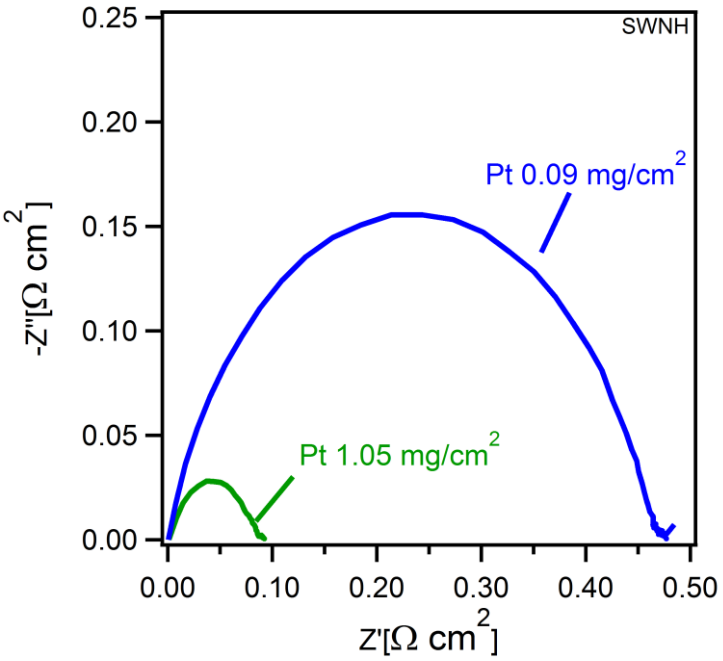

Figure 4-17 EIS at OCV of Pt loadings on carbon single walled nano horns (SWNH)

Again, lowering the Pt loading in the electrode drastically reduces performance of the cells. SWNH have showed promise for potential applications in fuel cells[108].

However, their activity drastically decreases due to the rapid oxidation of the carbon as well as the carbon corrosion reaction with water. In hydrogen separation systems, we do not expose electrodes to oxygen, and the potentials are low enough to minimize the carbon corrosion reaction. However, the performance is less than the performance on XC72 regardless. Thus higher surface area carbons do not necessarily equate to increased electrode performance.

Our next carbon nanostructure that was investigated was multiwall carbon nanotubes (MWNTs). These MWNTs show structures 10-20 nm in diameter with walls comprised of 10-20 graphene layers, closed ends, and internal herringbone nanostructure. MWNTs also contained approximately 1 wt% encapsulated Co remnant from CVD synthesis[66]. These MWNTs were further modified by an aqueous infiltration process as well as a low energy ball milling process for 15 hours. The post milled MWNTs are shown in Figure 4-18.

After ball milling, Platinum nanoparticles were deposited onto MWNT/CDP mixture via a chemical vapor-phase decomposition from its respective metal acetylacetonate, $Pt(acac)_2$ This reactions was carried out using a fixed bed wherein the crystalline solid precursors was mechanically mixed with the MWNT/CDP mixture, in a N_2-water vapor atmosphere at elevated temperatures via a method that we have demonstrated previously[52,56,68]. The ultimate deposition temperature was 210 °C. The electrodes using multi-walled

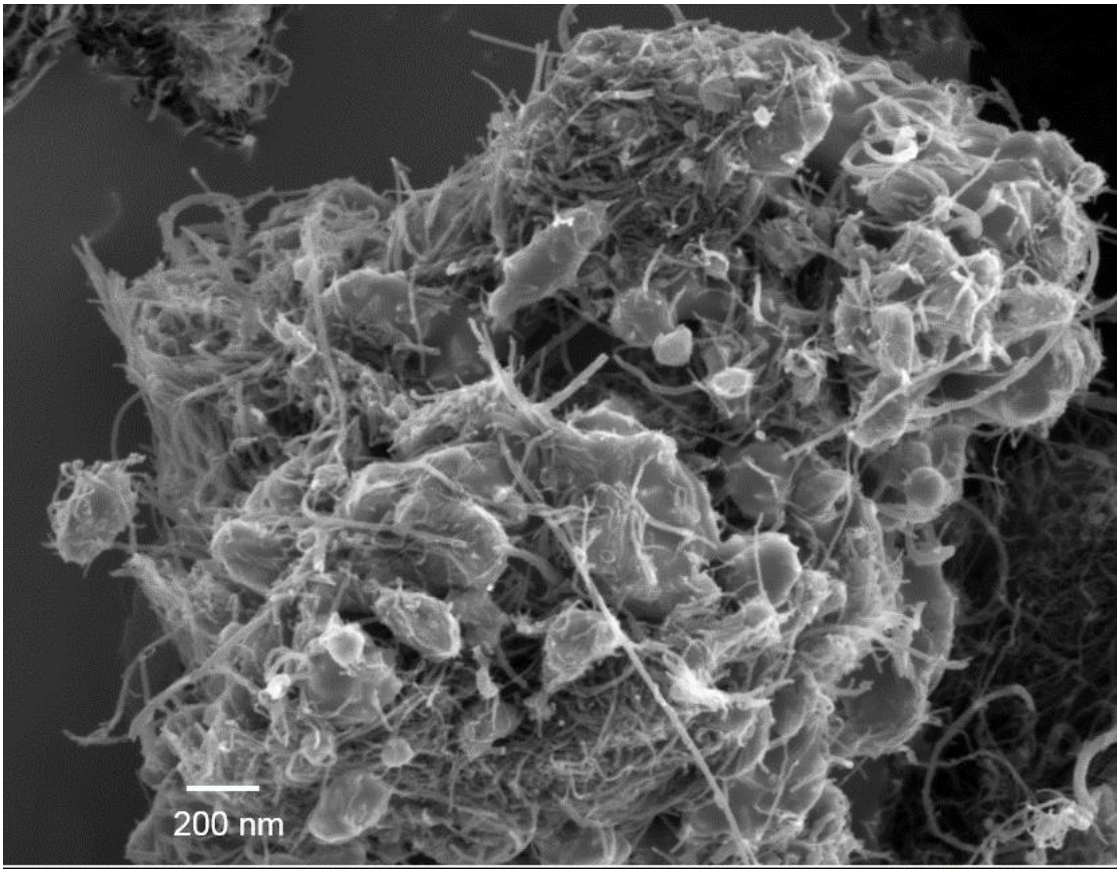

Figure 4-18 SEM micrograph of MWNTs infiltrated with CDP

nanotubes shows a large increase in electrode performance over the other carbon supports while drastically reducing the Pt loading, as observed in the EIS spectra at OCV in Figure 4-19. These electrodes have also shown promise as a more stable alternative to SWNH in cathodes for SAFCs[108].

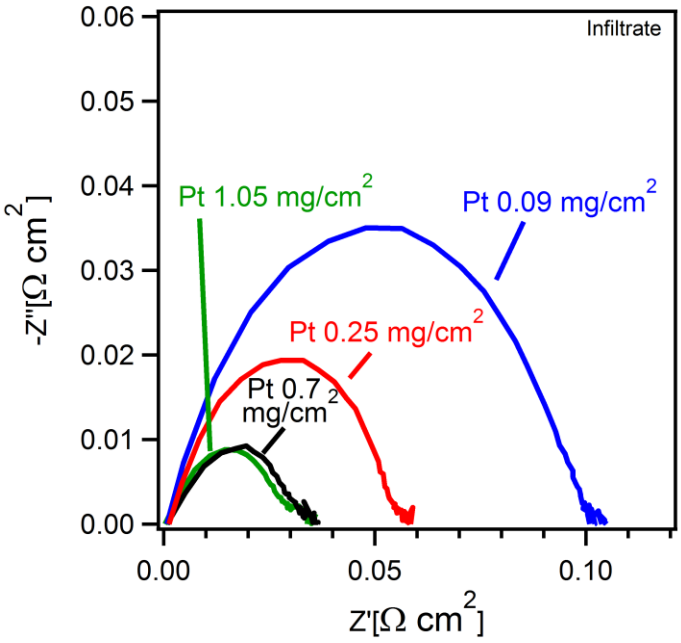

Figure 4-19 EIS at OCV of Pt loadings on carbon multi walled nano tubes

This is in contrast to the cathode performance reported previously in which the SWNHs had better performance during the first cycles. We contribute this increase in performance to the further increase of the ECSA of the MWNTs by the infiltration process. The surface area for these infiltrated materials started out as 22 m^2/g and after 16 hours at 250°C, increased to 26 m^2/g. From CO TPD measurements, there was a 96.8% Pt surface area retention. This slight Pt

surface area decrease is due to the coarsening of the Pt particles. This is consistent with previous studies using Pt nanoparticles[46]. We expect that further decreasing the Pt loading will lead to less particle coarsening and an increased Pt surface area retention rate.

Figure 4-20shows that even with a 6x reduction in Pt, performance is still better than previous generations of Pt electrodes. This increase is likely due to the increase of the ECSA, which is currently unknown for solid acid electrodes.

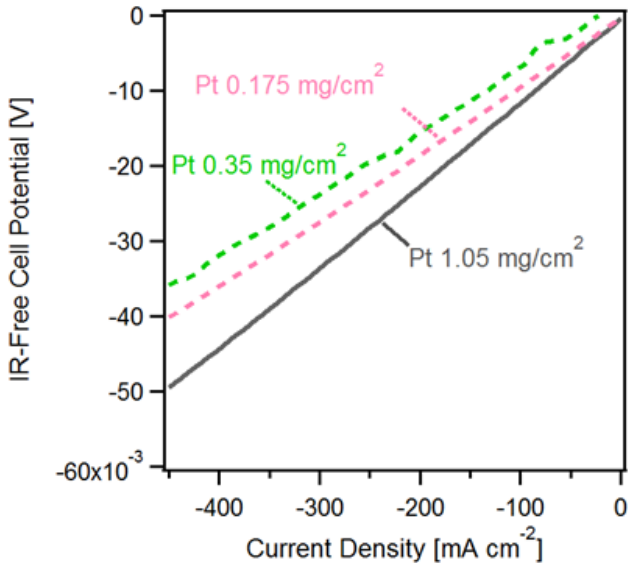

Figure 4-20 Polarization curves with the old generation Pt electrodes (solid lines) with a multistep electrode fabrication process on multi-walled carbon nanotubes

The lower loadings of Pt with the higher performance have shown that a more efficient electrode structure has been developed. While Pt is the superior

HOR catalysts, anodes for actual hydrogen separation will involve other impurities in the feed stream. While pure hydrogen streams are beneficial for laboratory experiments, in a real application separating hydrogen from hydrogen seems to be a silly endeavor. Syngas streams containing H_2, CO and CO_2 are much more probably feed streams in today's current hydrogen production scheme. Platinum has no interaction with carbon monoxide, which could potentially utilized as another source of hydrogen. Ru is a catalyst that oxidizes the CO (in the presence of water) in order to produce more protons. This is depicted in detail in chapter 3 but is also summarized in Figure 4-21

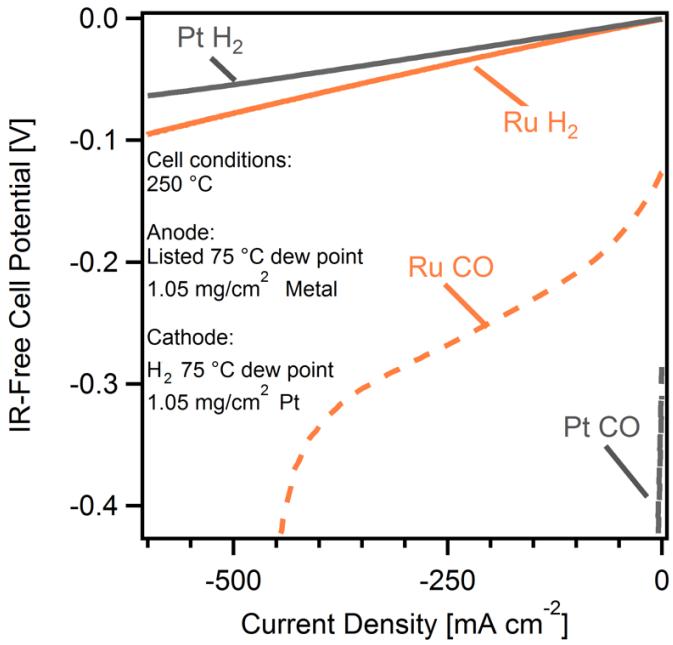

Figure 4-21 Hydrogen polarization curves for hydrogen (solid lines) and CO (dashed lines) for Pt and Ru anodes

In the infiltrated carbon nanotube support, Ru is deposited in similar fashion to Pt. . Ruthenium nanoparticles were deposited onto MWNT and CDP mixture via a chemical vapor-phase decomposition from its respective metal acetylacetonate, $Ru(acac)_3$ This reaction was carried out using a fixed bed wherein the crystalline solid precursors were mechanically mixed with the MWNT/CDP mixture, in a N_2-water vapor atmosphere at elevated temperatures via a method that we have demonstrated previously[52,56,68]. The ultimate deposition temperature was 240 °C. To examine if this new structure is suitable for use in a hydrogen pump cell, we probed the electrochemical cell performance. The iR-free polarization curves are shown Figure 4-22. While the performance decreases with the decrease of metal loading, similar to the XC72, the performance is better compared to Ru metal on Vulcan.

Based on these results, the optimal catalyst for HOR electrodes in solid acid separation devices could be a combination of Ru and Pt catalyst. A sample containing 0.89 mg/cm^2 Ru and 0.16 mg/cm^2 Pt was synthesized on infiltrated nanotubes via a simultaneous deposition at 240 °C in similar fashion to that above. Initial synthesis may form an alloy of Pt and Ru, but in operational conditions at 250°C containing hydrogen and carbon monoxide, these samples phase segregate leading to a bi-metallic catalyst of discrete Pt and Ru nanoparticles[94].

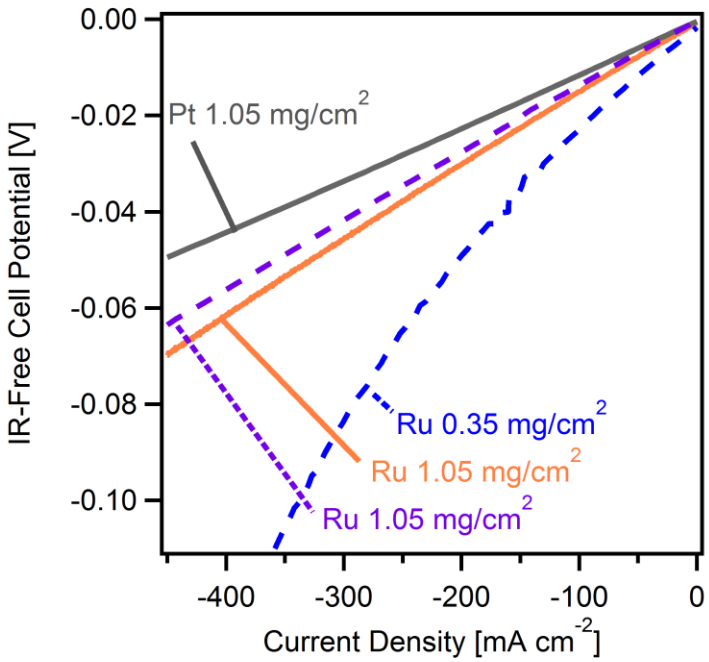

Figure 4-22 Polarization curves with the old generation XC72 electrodes (solid lines) with a multistep electrode fabrication process on multi-walled carbon nanotubes

An iR-free polarization curve obtained for a dual metallic Pt and Ru anode is shown in Figure 4-23 in pure hydrogen at 250°C.

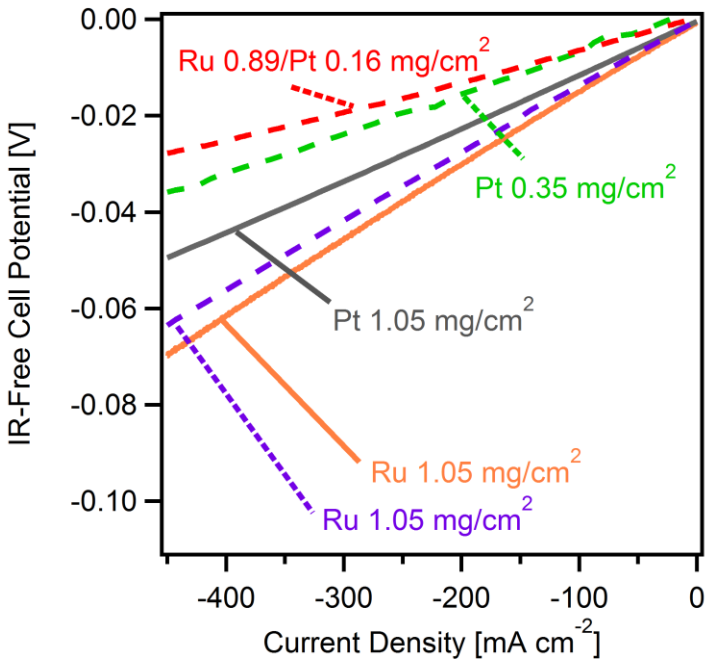

Figure 4-23 Polarization curves with the old generation Pt electrodes (solid lines) with a multistep electrode fabrication process on multi-walled carbon nanotubes

The bi-metallic catalyst out performs all infiltrates despite having less Pt. This performance increase is also shown in simulated methane reformate (10%CO 43% H_2 0.25% CH_4) as shown in Figure 4-24. The nonlinearity of the bimetallic curve at lower overpotentials has been reported before in previous

studies[36] and is attributed to the CO electrooxidation reaction as described in chapter 3.

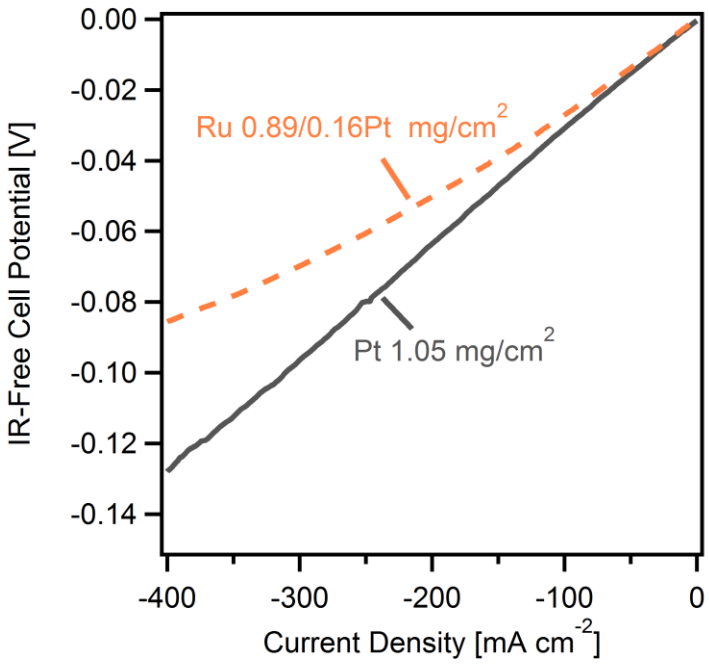

Figure 4-24 Polarization curves in simulated methane reformate with the old generation Pt electrodes (solid lines) with a multistep electrode fabrication process on multi-walled carbon nanotubes

Thus combination electrodes of Pt and Ru are the best performing electrodes for the HOR reaction in reformate streams. Further optimization can be achieved by development of more selective deposition techniques for the Pt and the Ru nanoparticles. Currently, these nanoparticles are not all deposited at interfaces where both CDP and MWNTs are present. Some are deposited on the carbon

as well as on the CDP. A more precise nanoparticle deposition technique could lead to drastic improvement in mass activity for solid acid electrodes.

Conclusion

We have shown that re-engineered anodes are superior to their previous iterations by increasing performance while simultaneously decreasing the overall Pt loading. While not as active as Pt, cathodes based off of low loadings of Ru and Ni show promise for cost effective hydrogen evolution catalysts.

CHAPTER 5

THERMAL STUDIES OF SOLID ACID FUEL CELLS USING ELECTROCHEMICAL IMPEDANCE SPECTROSCOPY

Abstract

While fuel cells are a more thermodynamically efficient system than traditional combustion processes, significant amounts of waste heat must still be rejected to regulate cell temperatures and for the case of systems based on the solid acid cesium dihydrogen phosphate (CDP), prevent undesirable phase transitions. CDP has a comparatively low thermal conductivity (0.41 $Wm^{-1}K^{-1}$), which limits its capacity for heat exchange. In order to better understand the flow of waste heat and the thermal distribution in operating cells, experiments were designed using the CDP membrane as an in situ temperature probe. Analyses included using high frequency impedance spectroscopy measurements of proton conductivity, transient plane source measurements of thermal conductivity and development of a 1-D thermal model. In order to increase the thermal conductivity of cell components, β-silicon carbide whiskers were selected for use in composites, due to a relatively high thermal conductivity of 120 $Wm^{-1}K^{-1}$. Analyses of these new composites included using high frequency impedance spectroscopy measurements for proton conductivity and transient plane source measurements for thermal conductivity.

Introduction

The hydrogen fuel cell is a promising electrical generation system. However even the most efficient automotive PEM fuel cells still generate roughly 1:1 electrical power to thermal power. Polarization curve for a mock hydrogen/air fuel cell is shown in Figure 5-1.

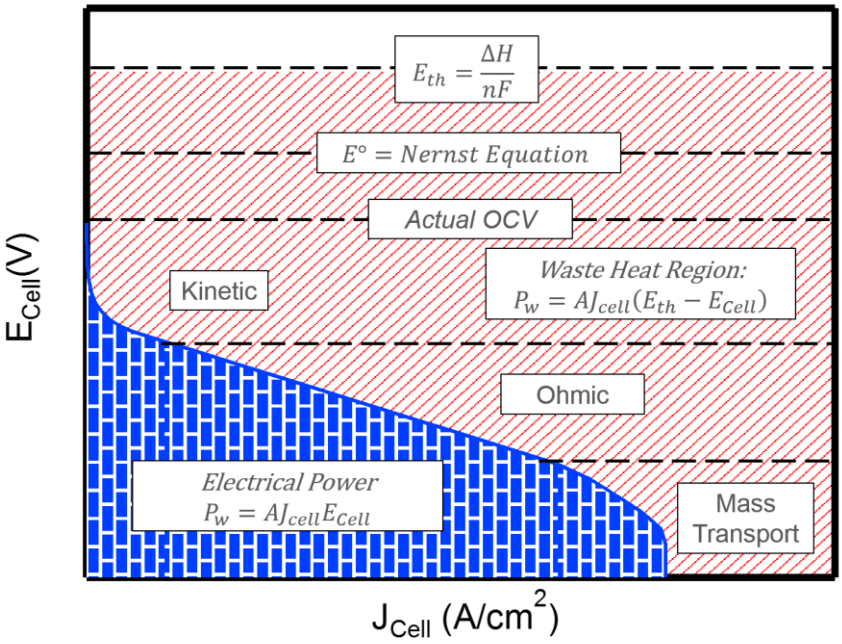

Figure 5-1 Mock hydrogen/air fuel cell polarization curve to illustrate the ratio of waste power to usable power

The electric power is shown under the curve in blue and is described by equation 5.1.

$$P_{gen} = E_{cell} * J \quad (5\text{-}1)$$

Where E_{cell} is the cell potential in V and J is the current density in A/cm^2. The "waste" power is generated at rate given in equation 5.2

$$P_{waste} = J * (E_{th} - E_{cell}) \quad (5\text{-}2)$$

Where E_{th} is the thermal voltage derived from the overall enthalpy of reaction. In order to increase the overall efficiency of the system, thermal recycling of the "waste" power is crucial. One application is to apply the heat generated to reactions required to generate hydrogen for fuel cell operation. The steam reformation of methanol, equation (1-5) is an endothermic reaction which has potential applications for consuming thermal energy generated as a byproduct of the electrochemical process.

The steam reformation reaction for methanol is optimal using commercial copper based catalyst at an intermediate temperature range of 230-260°C. A relatively new electrolyte that operates in these temperature ranges is based on the electrolyte cesium dihydrogen phosphate (CDP). These cells have already showed promise in the past using steam reformed methanol as an anode input. However, the thermal conductivity is low for CDP (0.41 W/mK) and in fuel cell operation, most of the thermal energy is generated at the cathode. With the steam reformation reaction occurring on the anode, a thermal conduction network must be implemented in order to transport the heat effectively into the reformer. Here we investigate the thermal properties of solid acid fuel cells as

well as design composites for increased thermal conductivity while minimizing the proton conductivity lost. This is achieved

Experimental Methods

CsH_2PO_4 was synthesized by reaction of $CsCO_3$ (Alfa Aesar, 99%) with H_3PO_4 (Alfa Aesar, 85%) followed by precipitation in methanol and drying. The as-synthesized CDP was low-energy ball-milled to reduce its initial particle size, yielding a fine particulate powder with a BET surface area of approximately 2 m^2/g. Carbon-supported metallic nanoparticles were synthesized as hydrogen oxidation and evolution catalysts. Platinum nanoparticles were deposited onto Vulcan XC-72R via a vapor-phase decomposition from their respective metal acetylacetonates $Pt(acac)_2$ (Strem Chemical). These reactions were carried out using a fixed bed wherein the crystalline solid precursors were mechanically mixed with the Vulcan XC-72R carbon, in a N_2-water vapor atmosphere at elevated temperatures (210°C) via a method that we have demonstrated previously.

Composite electrocatalyst powders were synthesized by dry-grinding the fine CDP with the various metal/carbon catalyst and naphthalene (a fugitive binder). These mixtures kept the mass ratio of CDP, naphthalene and carbon to 3: 1: 0.4 (mass) allowing for variation of the electrode catalyst mass without modifying the electrode thickness. Solid acid membrane-electrode assemblies (MEAs) were

then fabricated using these electrocatalysts by lamination of active layers in a 2.85 cm^2 diameter hardened steel die. Stainless steel mesh was used for current collector and PTFE tape for a sealant. Each MEA had a membrane thickness of approximately 40, 80 and 170 microns. The mass of a given electrode varied between 22 to 28 mg dependent on the metal loading on the carbon support. In each cell, the hydrogen evolution electrode was laminated at 125 MPa while the hydrogen oxidation electrode was laminated at 25 MPa.

Prior to electrochemical testing, the cell assembly was heated to 150 °C in dry Ar. Both electrodes were then switched to a wet Ar purge at 75 °C dew point and heated to the testing temperature of 250 °C. Electrochemical testing was conducted at 250 °C. At the start of the experiment, the anode was supplied 30 sccm of humidified ultrahigh purity hydrogen at a 75 °C dew point and the cathode was supplied air at 70 sccm at a 75°C dew point. Polarization curves were recorded at 30 minute intervals with a Bio-Logic VSP potentiostat by scanning the working electrode potential at 5 mV s^{-1} from the open circuit voltage (OCV) to 0 V. Potentiostatic electrochemical impedance spectroscopy (PEIS) spectra were also recorded at 0.8 V in a frequency range from 200 kHz to 200 mHz with a single sine perturbation amplitude of 10 mV. Polarization curves free of the ohmic losses due to membrane resistance were derived by the subtraction of the current multiplied by the high frequency resistance measured at OCV. Cells were held at 0.6 for 30 minutes between testing cycles. After 15 hours the

solid acid electrochemical device will be run as a hydrogen/air fuel cell at 250 °C using the protocol shown in Figure 5-2.

In order to measure the proton conductivity of composites, a 4-probe conductivity probe was built using a quartz tube furnace. A 4 bore alumna tube was used to separate the Inconel wire and the sample was attached using silver paint and silver paste. Silver paint was first applied unto the surface of the sample in order to ensure that a uniform silver coat was applied to the electrode surface.

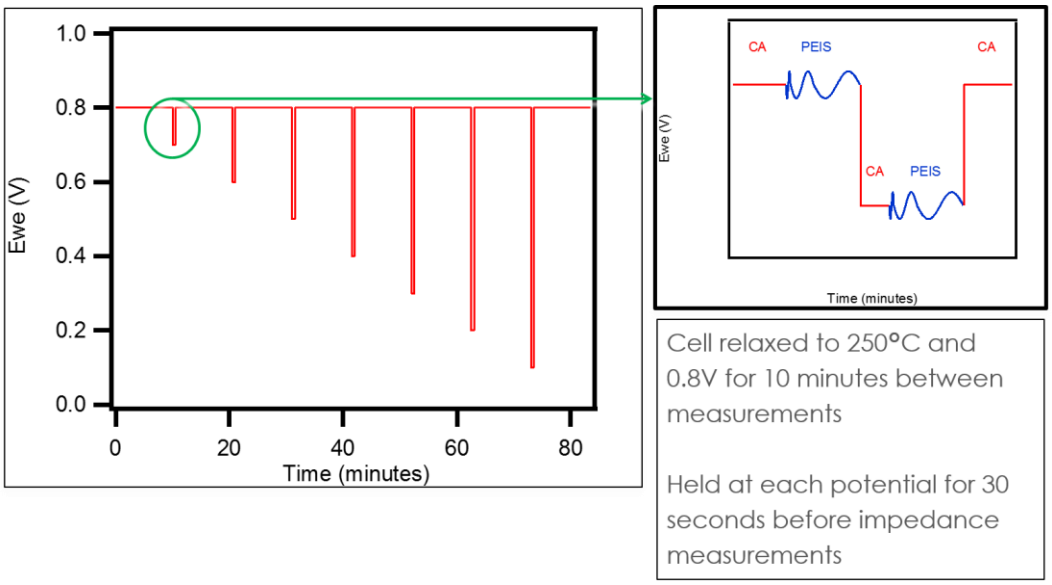

Figure 5-2 Experimental procedure for measuring the average membrane temperature change based on conductivity.

The painting a paste technique is shown in Figure 5-3. Composites were synthesized by low-energy ball milling CDP with the respective material for 15

hours in methanol. These solutions were then sieved in a 53 micron sieve in order to remove the milling media. These materials were then dried in toluene overnight at 120°C in order to remove the methanol and any residual water. Pellets were fabricated by laminating powders using a 6.03mm dye and 125 MPa pressure for 5 minutes.

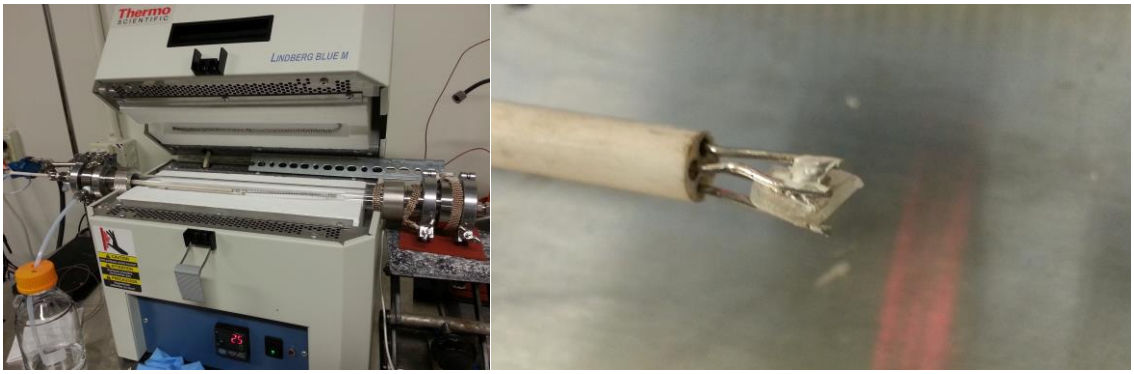

Figure 5-3 System built for measuring the proton conductivity of CDP and the solid acid composites.

TPS measurements were gathered using a Hot Disk thermal constants analyzer TPS 1500. Symmetric measurements were carried utilizing samples of similar dimensions. This setup was used in order to minimize the experimental drift error and help ensure accurate measurements. In order to create consistent contact pressure, stainless steel weights were placed on top of the sample to increase the pressure to the sensor.

Results and Discussion

The process of electrochemical hydrogen separation produces heat as a by-product of the reaction. In CDP based devices using endothermic steam reformation as a hydrogen producing technique, proper heat management can lead to an increase in system efficiency. Modeling such a system will allow for the determination of the optimal operational voltage, as well as the amount of thermal energy that is not being utilized. A model to describe the polarization losses must be used in order to define the amount of heat generated in a hydrogen separation system. A zero-dimensional model equation to define the cell potential as a departure from ideal voltage is described by equation (1-10). These inefficiencies lead to the generation of heat at a rate defined by equation (5-2). By taking advantage of the Arrhenius relationship, equation (1-23), of the super-protonic conductivity, a relationship can be derived to describe the average change in electrolyte temperature based on conductivity changes. Conductivity in relationship to resistance is described by equation 5.3.

$$\mathrm{R} = \frac{1}{\sigma} \tag{5-3}$$

Where R is the resistance and σ is the conductance. Intermediate temperature CDP has a conductivity defined by an Arrhenius relationship with the temperature. Thus a ratio of two

$$\frac{\sigma(T_1)}{\sigma(T_2)} = \frac{R_2}{R_1} = \frac{\mathrm{e}^{-\left(\frac{\mathrm{E_a}}{\mathrm{k}T_1}\right)}}{\mathrm{e}^{-\left(\frac{\mathrm{E_a}}{\mathrm{k}T_2}\right)}}$$

$$\frac{\sigma(T_1)}{\sigma(T_2)} = \exp\left[-\frac{E_a(T_2-T_1)}{k*T_2*T_1}\right] \rightarrow \exp\left[-\frac{E_a\Delta T}{k*T_2*T_1}\right]$$

Let

$$\alpha = \frac{E_a}{k}$$

Therefore

$$\frac{R_2}{R_1} = \exp\left[-\frac{\alpha\Delta T}{T_2 * T_1}\right]$$

$$ln\left[\frac{R_2}{R_1}\right] =$$

$$-\frac{\alpha\Delta T}{T_2 * T_1} \rightarrow \frac{\alpha T_1 - \alpha T_2}{T_2 * T_1} \rightarrow \frac{\alpha}{T_2} - \frac{\alpha}{T_1}$$

Solving for T_2

$$\frac{\alpha}{T_1} + ln\left[\frac{R_2}{R_1}\right] = \frac{\alpha}{T_2}$$

$$T_2 = \frac{\alpha * T_1}{\alpha + T_1 * ln\left[\frac{R_2}{R_1}\right]} \qquad (5\text{-}4)$$

Remembering that

$$\alpha = \frac{E_a}{k}$$

Where E_a = 0.42eV for CDP.

A base-line overpotential was applied for a fixed amount of time to allow the system to equilibrate to the operational temperature of 250 °C followed by an EIS measurement to determine R_1. Next an increased overpotential will be applied to the cell followed by an EIS measurement to determine R_2. The

difference in these resistances correlate to a difference in the average temperature in the electrolyte. Three different membrane thicknesses were used to test the model.(40, 80 and 170 µm).

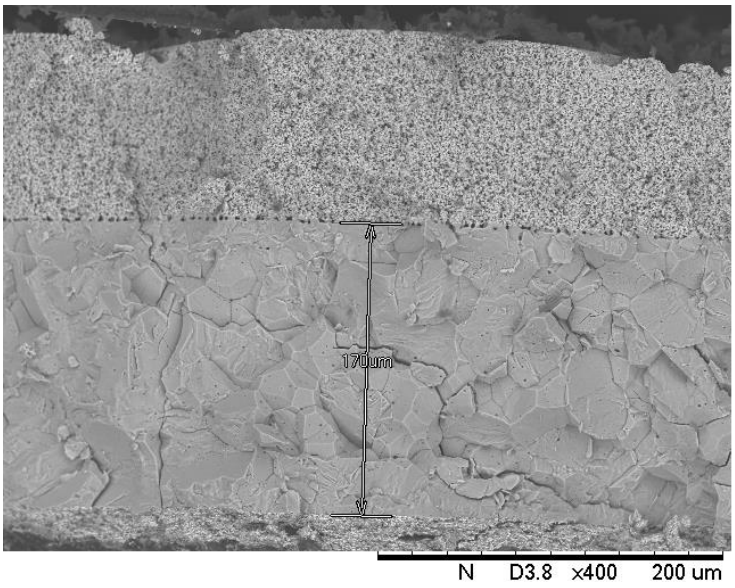

Figure 5-4 Cross section of the 170 micron fuel cell used for testing the thermal model. The cathode is at the top, with the anode at the bottom.

The measured high frequency resistances for the procedure are shown in Figure 5-5 using the technique described in Figure 5-2. The insert shows a measured resistance as well as a depiction of R1 and R2 for 0.1V of cell potential. For the 170 and 80 micron membranes, the baseline remained consistent throughout testing. The 40 micron membrane showed an increase in baseline resistance. This is most likely due to creep of the CDP or possibly dehydration.

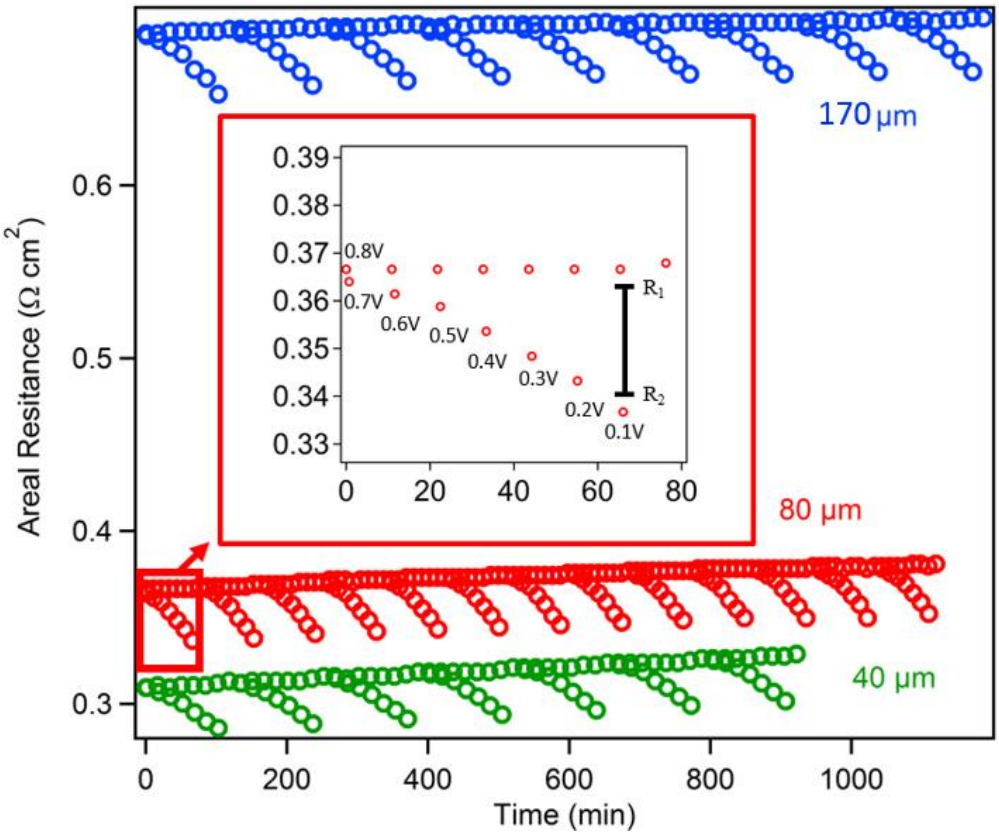

Figure 5-5 High frequency resistance of three cells with variable membrane thickness used to determine the average membrane temperature.

Transient plane source (TPS) measurements were performed under room temperature conditions to determine the thermal conductivities of materials used in solid acid electrochemical devices. TPS data is shown for CDP and GDL in Figure 5-6. In order to determine the thermal conductivity, the TPS data is fit to (1-30). The average membrane temperature was calculated using the equation (5-4). Summary of TPS acquired thermal conductivity results are shown in Table 5-1.

Table 5-1 Thermal conductivities of solid acid fuel cell's MEA

Sample	Thermal Conductivity (W/(m*K))	Length (microns)
Stainless Steel support	0.17	6300000
Micro Porous layer	0.35	90
Anode	0.44	35
Membrane	0.41	(40,80,170)
Cathode	0.46	160
Carbon Paper	0.17	190

In order to investigate the effect of the solid-solid phase transition, cesium hydrogen sulfate (CHS) was used a substitute solid acid. Cesium hydrogen

sulfate does not have the humidity requirements of CDP and undergoes the superprotonic phase transition at 140°C. Cesium hydrogen sulfate was used previously as a solid acid electrolyte, however it undergoes a reaction in the presence of Pt and hydrogen to form hydrogen sulfide. This leads to a breakdown of the proton conducting network in the electrode.

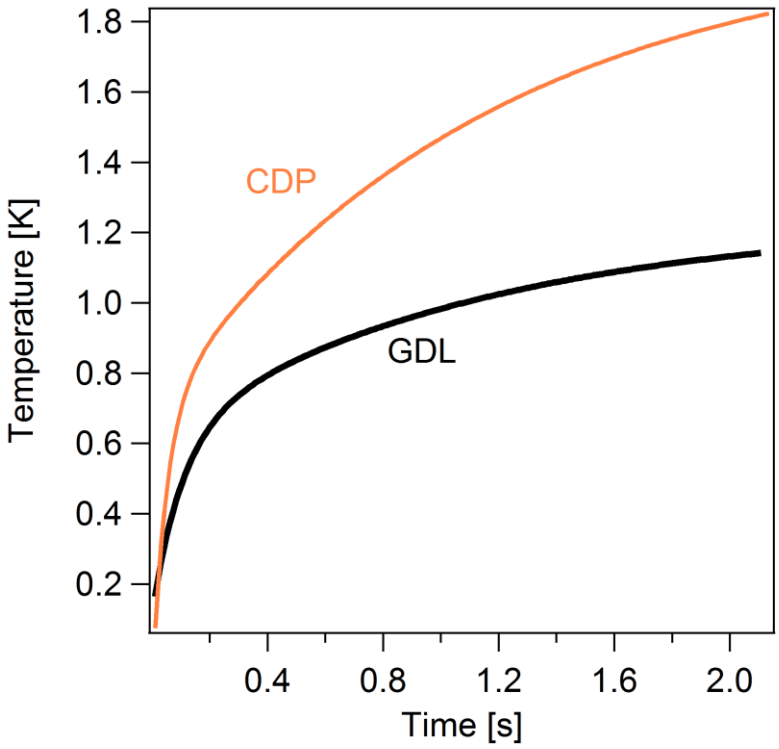

Figure 5-6 TPS measurements for CDP and the 35AA carbon paper

The proton conductivity of CHS can be seen in Figure 5-7. Where the thermal conductivity was measured to be slightly lower than CDP at 0.3 W/(m K)

at 25°C and 0.32 W/(m K) at 150°C. From these results, we assume that CDP has a minimal increase to thermal conductivity due to the phase transition.

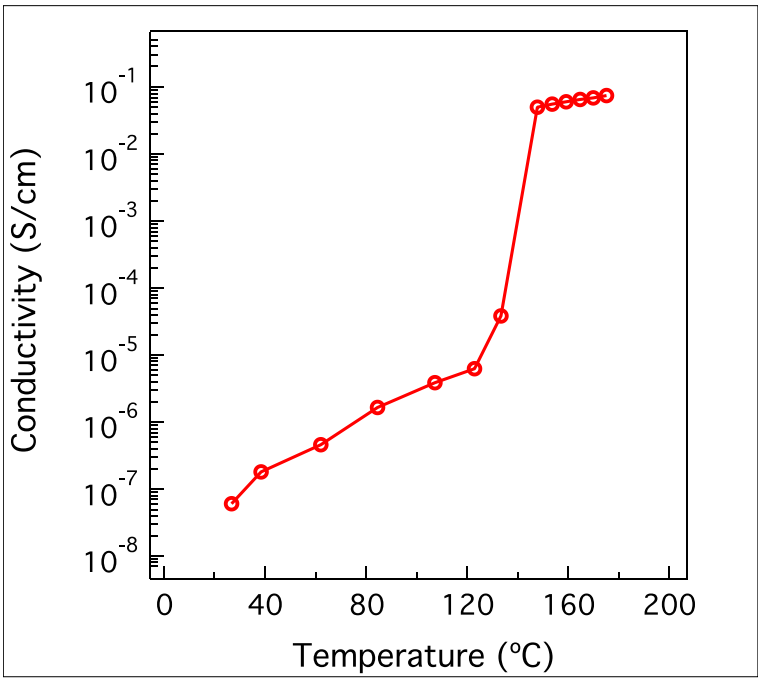

Figure 5-7 Cesium hydrogen sulfate proton conductivity versus temperature.

A fuel cell thermal model is created making the assumption that the heat generation is isolated to an infinitely small plane between the membrane and the cathode. This model also assumes that the heat is transferred by conduction only. A temperature profile based on the overpotential using this model is shown in Figure 5-8. The 40 micron model shows the largest variation and deviation from the experimental results. The higher temperatures generated in the cell

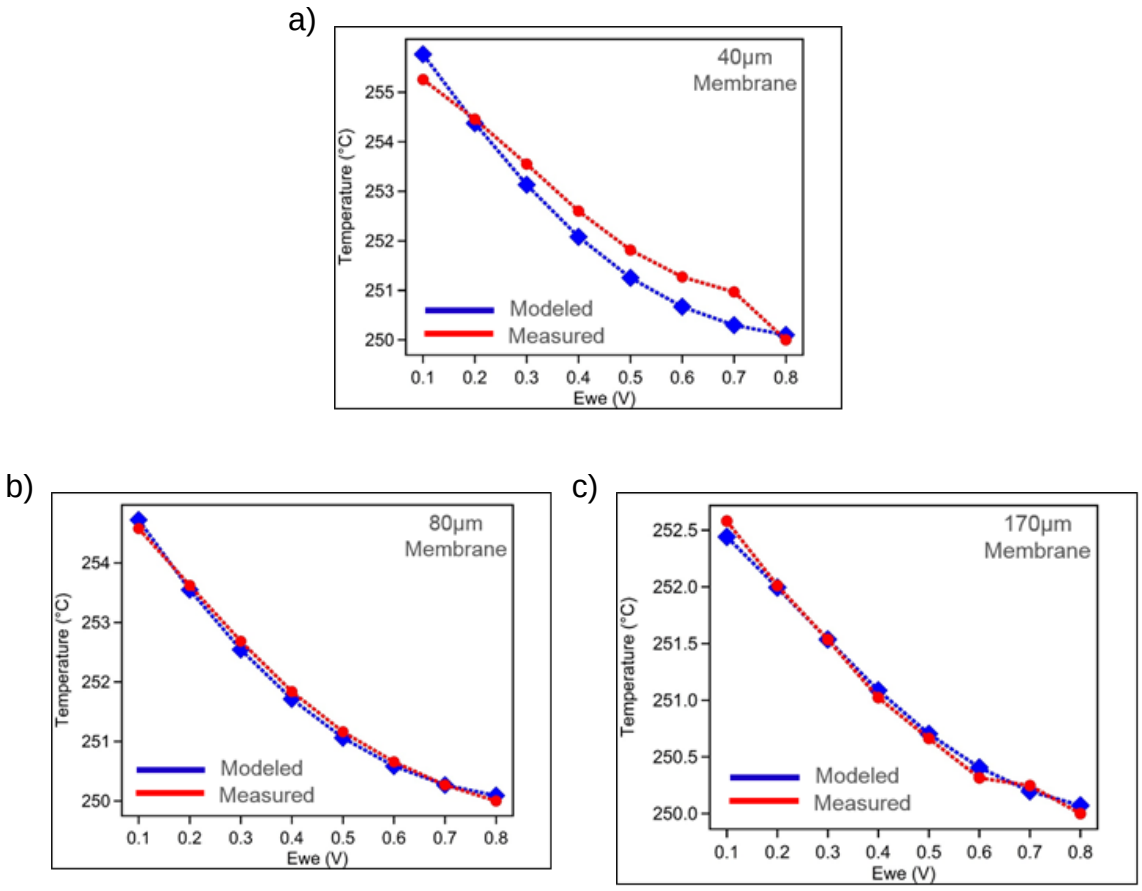

Figure 5-8 Average membrane temperature of the model compared to experimental temperature calculated from the high frequency resistance differential

lead to cell degradaton. This degradation can also be seen in Figure 5-5 with the 40 micron membrane showing a baseline resistance increase of over 30%. We contribute this decrease to the changes in the cathode microstructure related to the properties of the CDP electrolyte. CDP is a superplastic in its superprotonic phase, leading to large enhancement of the sintering rate of the individual Pt particles, which effectively reduces the overal catalystic activity and impairing gas diffusion. This is in contrast with the 80 micron and 170 micron cells which stayed relatively constant throughout the experiment. A cell temperature profile is generated in Figure 5-9 for a viewing distibution of the temperatures while a cell is held at 0.1V The majority of heat is conducted through the cathode of the cell. This is due to the low thermal conductivity of CDP leading to poor heat transfer across the membrane. Also while stainless steel has a bulk thermal conductivity of 11 W/mK, we have measured a much lower value of 0.17 W/mK. This is due to the porosity of the stainless steel GDL. Also the thickness of the stainless steel GDL leads to a very low overall thermal conductance. This leads to our stainless steel support act as an insulator. This could be used advantageously in order to sink thermal energy into one electrode. In our case, we are interested in sinking thremal energy into the anode in order to support endothermic steam reformation reactions. Thus a redesign of cell archetecture would need to be achieved. However, due to the confrmal coatings of Pt on the CDP, we can not currently fabricate such a design. This is due to

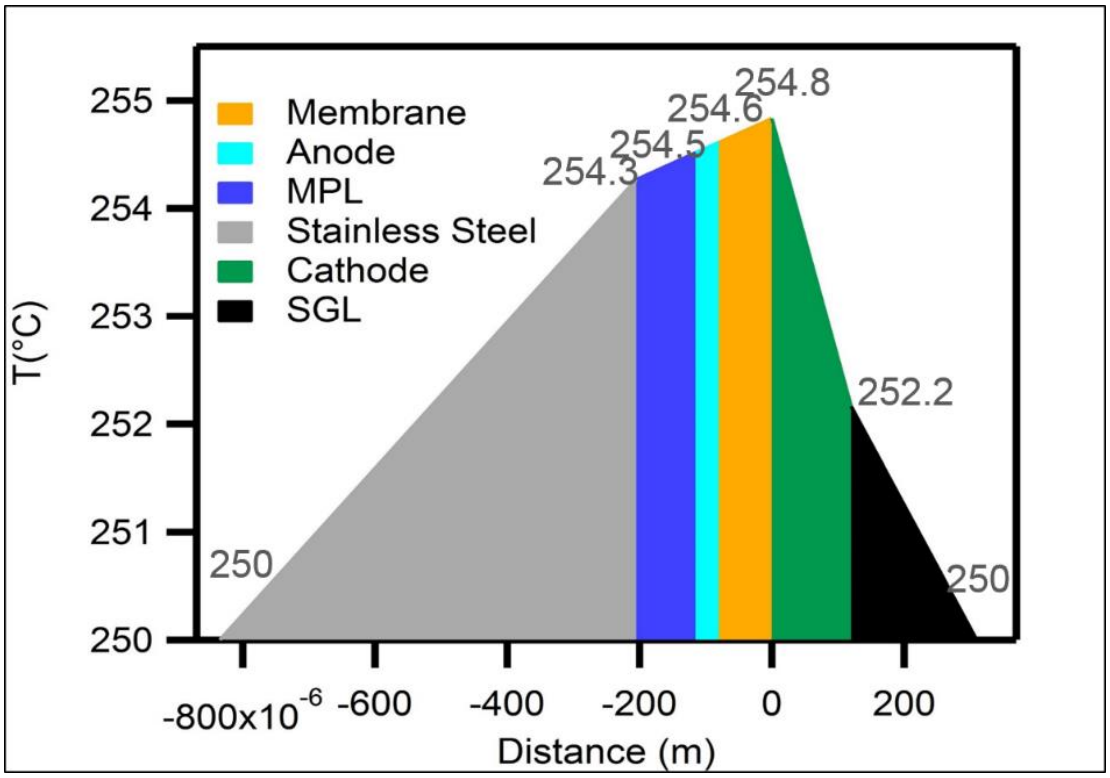

Figure 5-9 1d temperature profile of the 80 micron solid acid fuel cell at 0.1V

our lamination procedure for the membrane. Due to the high pressure required, we would remove the porosity of our cathode if we tried to laminate it first. For the anode, we induce porosity by use of a fugitive binder. However this leads micron size voids in the electrode. This would greatly reduce the electron network in the cathode leading to lower performance.

In order to address the issue of CDP's low thermal conductivity, SiC was selected as an additive agent for composites. In order to achieve desired dispersion, a mixing and milling technique was developed by first mixing the SiC and CDP mechanical then by a low energy ball milling technique in methanol. The effects of the low energy ball milling technique can be observed in Figure 5-10. The darker areas are group of SiC particles. Ball milling and mixing leads to a greatly enhanced dispersion with no noticeable groups of SiC.

While we note that we have achieved effective dispersion, this does not create the desired single connected thermal network. With our current procedure, we are unable to laminate SiC into a solid like we do with CDP. This leads to dispersed SiC particles throughout the composite but not a network. In order to greatly increase the thermal conductivity, a single network that leads directly to the heat sink (or in our ideal case a steam reformer) would be desirable. Our current work is designed as a proof of concept for potential materials for this network.

a)

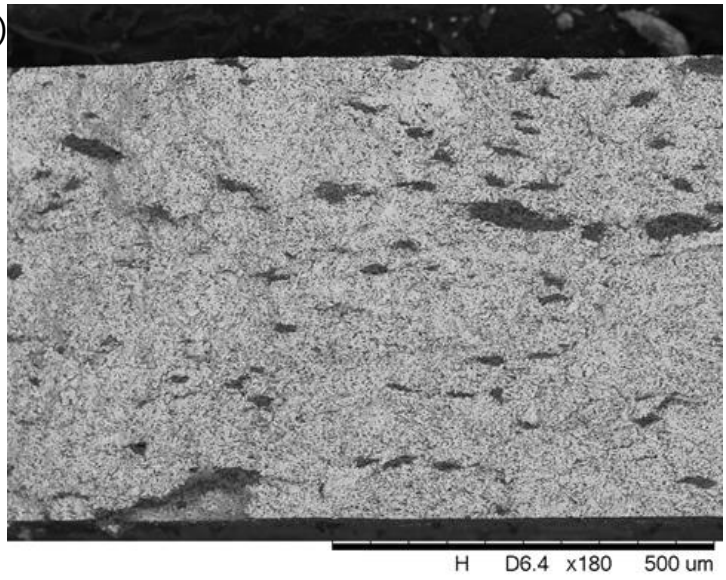

b)

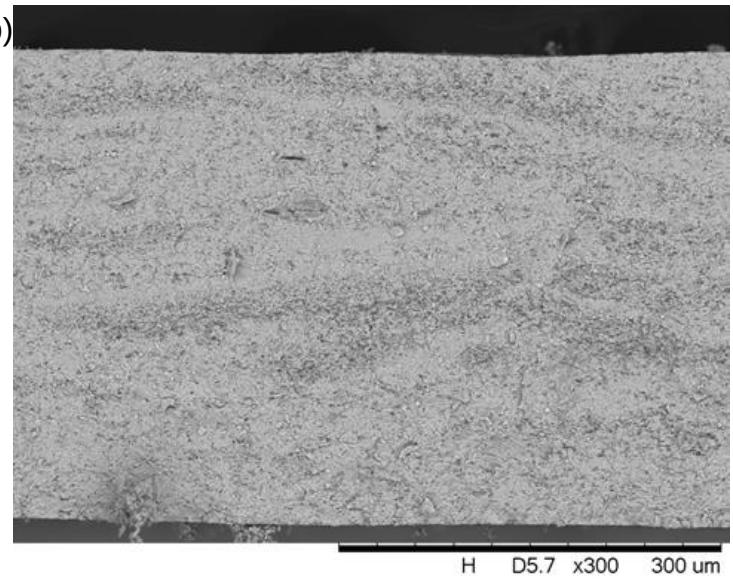

Figure 5-10 Mixing procedure effect on 10%SiC/CDP composites. a) No mixing b) After mixing

Figure 5-11 depicts the proton conductivity of three different mass percentages (5%, 10% and 15%) of SiC mixed with CDP. When temperatures are below the solid-solid phase transition of 228°C, the SiC composites show an increase in the proton conductivity. This is most likely due to residual silica and other impurities that lead to a different manor of proton conductivity similar to what was reported for silica and CDP composites[35].

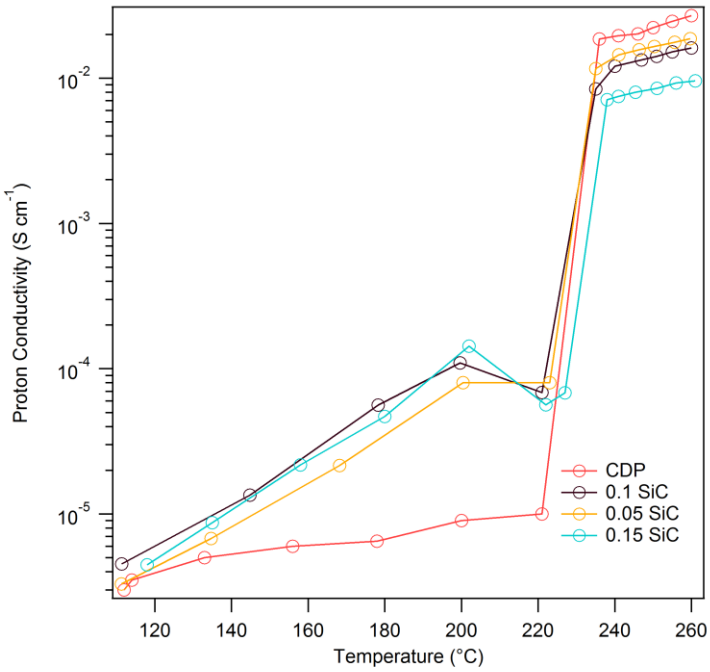

Figure 5-11 Proton conductivity of various weight percentages of SiC and CDP.

Post 228°C, the proton conductivities show a trend that is not represented by a volumetric decrease. At 250°C, the proton conductivities are 0.022, 0.017,

0.014, and 0.009 (S cm^{-2}) for CDP, 5%, 10% and 15% SiC. Based off the trend seen in the lower temperature conductivities, we contribute this non volumetric decrease to residual impurities.

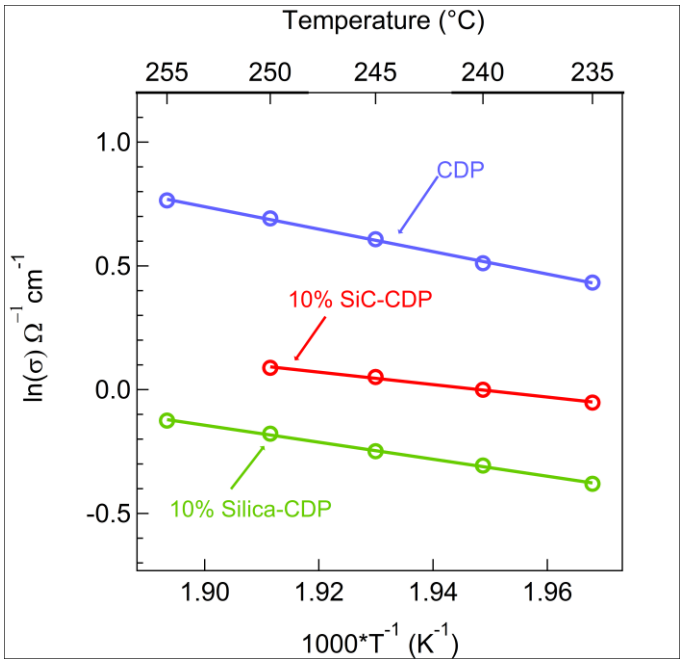

Figure 5-12 Intermediate temperature proton conductivities for 10%SiC/CDP and 10%Silica/CDP.

The effects of silica to the high temperature proton conductivity of CDP are detrimental. At 250°C and 10wt% silica the proton conductivity is 0.007 S cm^{-2}. This reduction of proton conductivity is due to the hydrogen bonds that form between the solid acid and the silica. These hydrogen bonds inhibit the phosphate tetrahedron which is responsible for the high temperature proton conduction mechanism in CDP. This trend can also be seen in the activation

energy with CDP being 0.413eV, 5%SiC being 0.4eV, 10%SiC being 0.34eV, 15%SiC being 0.31eV 10% silica being 0.197eV.

In order to minimize the loss of proton conductivity to impurities, various other SiC were tested with different synthesis methods from vendors. These can be seen in Figure 5-13.

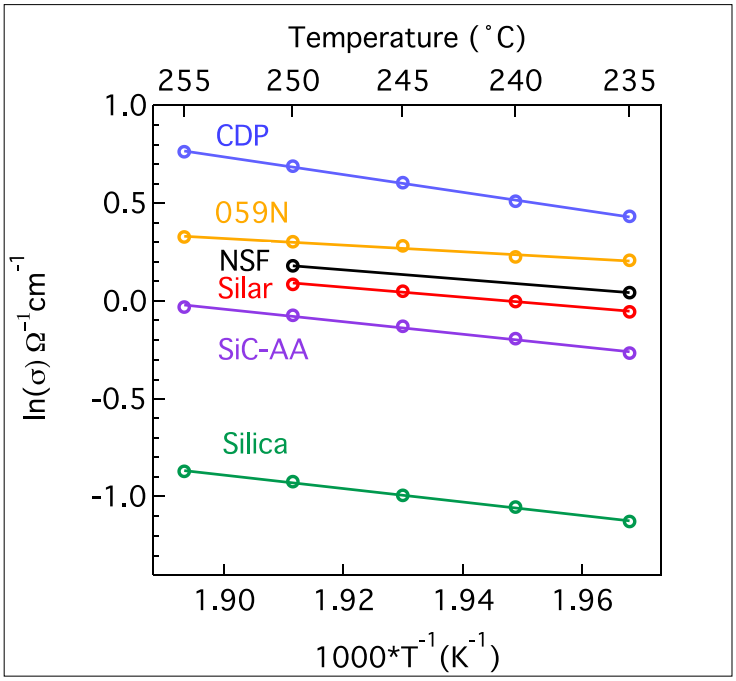

Figure 5-13 SiC from various vendors and CDP composites with weight percentages 10% and 90% respectively.

A concentrated base wash of KOH was applied to the 059N SiC powder in order to further purify the sample from impurities. A control composite sample was

created using micron diamond particles of similar size to the 059N SiC sample. The proton conductivities of these composites can be seen in Figure 5-14

The pre transition proton conductivity has changed with our washed sample to the similar form of CDP. The post transition proton conductivity at 250°C is 0.016 (S cm^{-2}) for 10%SiC and 0.0197 (S cm^{-2}) for 10% diamond. The activation energy is 0.38eV for 10%SiC based washed samples and 0.410eV for 10% diamond samples. These results are summarized in Table 5-2. Composite thermal conductivities for SiC showed little variation based off of vendor or base washing. Composite thermal conductivities corrected for the volume fraction for

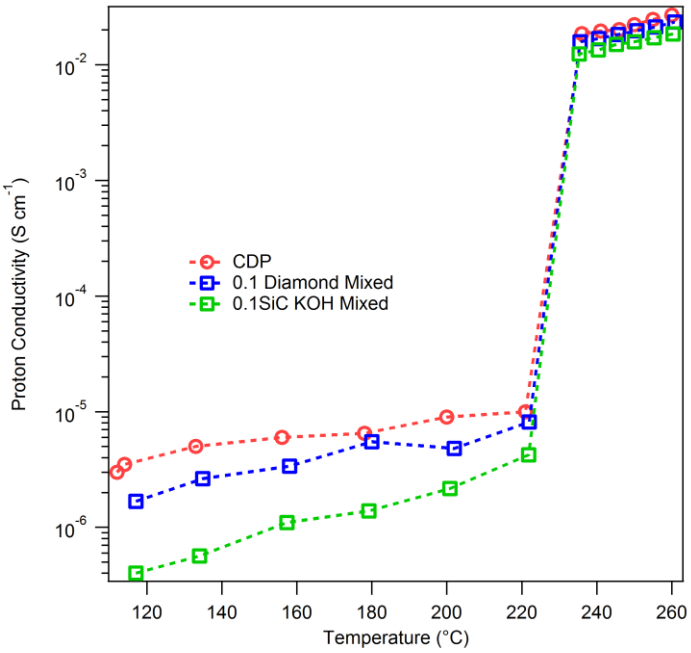

Figure 5-14 Proton conductivity of CDP mixed with 10% diamond and 10% SiC after base washing.

Table 5-2 Proton conductivity of CDP mixed with 10% diamond and 10% SiC after base washing.

Sample	Activation Energy (eV)	Proton Conductivity at 250°C (S cm^{-2})	Volume Corrected Proton Conductivity at 250°C (S cm^{-2})
CDP	0.413	0.0223	0.0223
10% Diamond	0.41	0.0197	0.0217
10% SiC Washed	0.38	0.0159	0.0181
5% SiC	0.4	0.0165	0.018
10% SiC	0.33	0.0138	0.014
15% SiC	0.31	0.00853	0.012
10% Silica	0.197	0.007	0.01

SiC samples showed little variation based off of vendor or base washing. Combining the 10% KOH was SiC with CDP has led to an increase of 221% in thermal conductivity while maintaining 77% proton conductivity. A more careful and controlled synthesis method of SiC would likely lead to a further increase in proton conductivity while maintaining or increasing the thermal conductivity.

Figure 5-15 depicts a summary of overall conductivities for the highest CDP/SiC thermal conducting species. While the overall proton conductivity of the composite has decreased by 23%, we must also consider the possibilities for

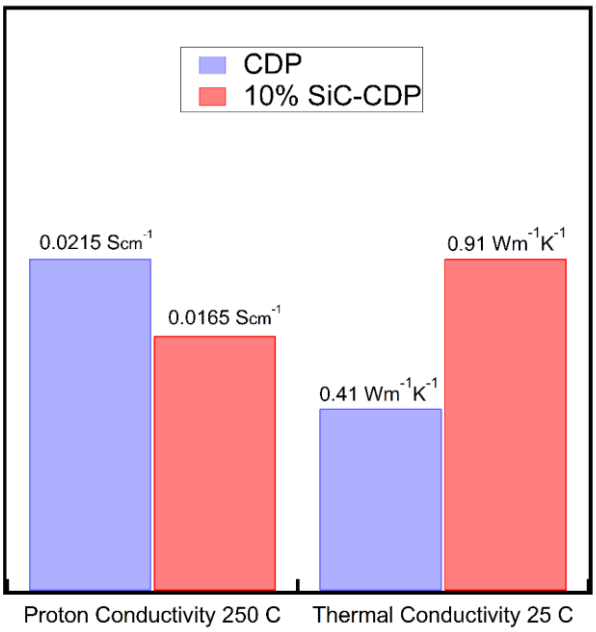

Figure 5-15 Best performing proton conductivity and thermal conductivity of CDP and 10%SiC/CDP composites.

an increase in conductance by decreasing the thickness of the membrane itself.

While low temperature fuel cells based off of polymer membranes must consider membrane thickness in order to minimize crossover, this is not the case with a solid membrane. However, little has been invested into fabrication of thinner membranes in solid acid systems. One reason for this is the mechanical properties of solid acids are not well known. Some research has been done to analyze the properties of cesium hydrogen sulfate, but measuring the mechanical properties of CDP remains even more difficult due to the humidity requirements. From the CHS research, we have learned that the creep for solid acids is relatively high. This has also been observed in CDP based systems. In order to make a truly stable membrane, composite materials seem advantageous. This has been demonstrated in the CHS[109].

Another consideration is the effect of local heat generation with the effect on the CDP electrolyte. By observing the phase diagram, the acceptable temperature range for our operating humidity (0.3 atm) the temperature should not exceed 260°C[35]. However, even in our own experiments and a 40 micron membrane, we approach 256°C for the average membrane temperature. The interfacial temperature can be calculated to slightly higher than that at 258°C. We can easily extrapolate to making a thinner membrane leading to a larger increase in interfacial temperature which approaches the dehydration temperature. Multiple optimizations solutions exist and should be considered to address this problem. Two potentials are increasing the amount of water,

however this will decrease the overall cell performance due to lower concentrations of reactants. Another is decreasing the temperature of operation which decreases the reaction kinetics as well as the membrane conductivity. Thus the only viable solution to increasing the cell performance while maintaining stability is development of a composite membrane based on a SiC thermal network. One possible technique for this network development is to use electrospinning for SiC mats and impregnating with CDP via aqueous solution.

Conclusion

Using high frequency impedance spectroscopy measurements of proton conductivity and transient plane source measurements of thermal conductivity we developed a 1-D model for heat conduction in an operational solid acid fuel cell at 250°C. In order to increase the thermal conductivity of cell components, β-silicon carbide whiskers were selected for use in composites, due to a relatively high thermal conductivity of 120 $Wm^{-1}K^{-1}$. Composites of 10% SiC by volume increased the thermal conductivity by 221% while maintaining 77% of the proton conductivity. We expect further optimization can be achieved by development of a SiC mats and aqueous impregnation with CDP.

CHAPTER 6

CONCLUSION

We have investigated the solid acid electrolyte cesium dihydrogen phosphate for an electrochemical hydrogen separation system. We first demonstrated a suite of carbon-supported catalysts (Pt, Pd, Ru, Ni and Cu) on XC72 for implementation in electrodes at a metal loading of 1.05 mg/cm^2 for both the anode and the cathode. Pt showed the highest performance with a current of 591 mA/cm^2 at a cell overpotential of 300mV. When comparing the total cell performance to other Pt hydrogen separation systems, we note that at 600 mA/cm^2 the over potential for a PFSA system operating at 80°C is 20mV at a metal loading of 0.4 mg/cm^2 per electrode[92] and for PBI based systems is 125mV for 1 mg/cm^2 at 160°C[25]. The large difference in performance stems from the large ohmic resistance in our current solid acid hydrogen pump design. 80% of the cell overpotential was due to the ohmic losses. While the conductivity of CDP is lower than that of PFSA and PBI, we can decrease the overall resistance by utilizing thinner membranes. Our average high frequency resistance is 0.4 Ω-cm^2 for membranes that are 80 microns thick. For the PFSA system, the HFR was measured as 0.044 Ω-cm^2. Thus, in order to obtain comparative results, we must reduce our membrane thickness by 10, to 8 microns. For the PBI system, the measured HFR was 0.1 Ω cm^2. Thus we need to decrease our membrane by a factor of 4 in order to obtain similar ohmic loses. From an electrode standpoint, our measured charge transfer resistances, 0.07 Ω cm^2, were notably higher than the reported values of 0.02 Ω cm^2 and 0.015 Ω cm^2 for PFSA and PBI respectively. This is likely due to the poor electrode optimization in our SAHP

systems. The mechanical mixing of CDP with supported carbon nanoparticles electrode design leads to less utilization of the catalyst surface area. However, we note the diversity of catalyst in our current study leads to other potential catalyst for our solid acid systems.

We prepared electrodes from several metals, using the 'PMCVD' technique to synthesize metallic nanoparticles on carbon supports. Ru shows promise as a catalyst for both the hydrogen oxidation reaction as well as the evolution reaction despite not being as active as Pt. In order to compare catalysts, we will remove the voltage lost to the ohmic resistances. We use performance at 60 mV of IR-free (300 mV for total cell potential in a symmetric Pt system) as a comparison point. At 60 mV of IR free overpotential for a 1.05 mg/cm^2 Ru anode and a 1.05 mg/cm^2Pt cathode, the current density obtained is 391 mA/cm^2. At 60 mV of IR free overpotential for a 1.05 mg/cm^2 Pt anode and a 1.05 mg/cm^2 Ru cathode, the current density is 555 mA/cm^2, an increase of 25%. The non-PGM catalysts tested in this study, nickel and copper, showed negligible HOR performance. Copper was not as active as nickel for hydrogen evolution, but showed a drastic increase in performance from previously reported values. Ni based cathodes with Pt anodes showed current values of 50 mA/cm^2 at 60 mV of IR-free cell potential at 1.05 mg/cm^2.

We then demonstrated that methanol can be steamed reformed and the hydrogen purified by 'hydrogen pumping' using an inexpensive solid acid electrolyte and zero Pt at 250°C. This exploits the excellent ability of CDP to

tolerate impurities in the anode feed. Although Ru is not as active as Pt for the HOR reaction, the metal is considerably less expensive and shows other advantages in the ability to electrooxidize CO. At 60mV of overpotential, the CO electrooxidation was 60mA/cm^2 for 90% CO balance of Ar with an anode of 1.05 mg/cm^2 Ru and a cathode of 1.05 mg/cm^2 Pt. We also demonstrated a pure CO fuel and air fuel cell design using our Ru anode with a Pt cathode. This showed a peak power density of 60mW/cm^2 with 90%CO balance Ar anode feed on a 1.05 mg/cm^2 Ru electrode and an air cathode feed on a 1.75 mg/cm^2 Pt electrode. In situ methanol steam reformation and hydrogen separation was then achieved by combining commercial Cu Hi-Fuel catalyst with Ru anodes. Ni cathodes were also implemented in order to demonstrate a non-Pt hydrogen separation system. At 60mV of IR-Free overpotential at for 1.05 mg/cm^2 Ru anode and Ni cathode operating at 250°C, we recorded a performance of 50 mA/cm^2.

In order to further optimize our SAHP system, we turned our focus to maximizing the tri-phase interface in the electrodes. Switching to a carbon nanotube infiltrate, we were able to reduce the Pt loading by a factor of 11 from 1.05 mg/cm^2 using our mechanical mixed XC72 design, to 0.09 mg/cm^2 while still maintaining a similar charge transfer resistance of 0.09 Ω cm^2. These re-engineered anodes are superior to their previous iterations by maintaining performance while simultaneously decreasing the overall Pt loading.

From all of these studies, we conclude that there is a substantial flexibility in our choice of catalyst enabling us to optimize our electrodes for a variety of fuel inputs. By observing only current response, streams that involve low amounts of CO (like reformed methanol at 1% CO), Pt remains the superior catalyst for all measured values. For higher concentrations of CO (reformed methane at 10%), Ru becomes the better option due to the CO electrooxidation in synergy with the HOR at current densities higher than 500 mA/cm^2. However for a systems applications, materials and operational cost must be considered. For materials cost, Pt is about 14 times more expensive than Ru. From the operational stand point, at 60 mV of IR free cell potential, Pt is 51% better than Ru for HOR and 6.5% better for HER. If cell size is a concern, a dual metal electrode using both Pt and Ru may be implemented to take advantages of Pt's intrinsically higher HOR kinetics and Ru's CO and HOR oxidation ability. If size is not a concern, a larger cell area may be implemented in order to maintain an overall current, but operate at a similar system voltage. The relatively low cost of the electrolyte is also beneficial to a larger cell design. Larger cells operating at lower overvoltages are key to achieving the combination of sufficient production rates and higher efficiencies for electrochemical hydrogen separation systems. When size is not a concern, Ru currently has all the characteristics that make it a suitable catalyst choice for anodes in both solid acid hydrogen pumps and for solid acid fuel cells.

After reducing the required electrode catalyst required, we turned our focus to determine the thermal energy generated in our solid acid electrochemical systems. By recycling the thermal energy generated as a byproduct of the electrochemical process into an endothermic steam reformation reaction (such a methanol steam reformation), an overall higher system efficiency can be achieved. Also, due to the phase requirements of CDP, careful management of the cell temperature must be maintained in order to achieve stable proton conduction. By taking advantage of the Arrhenius dependence of the intermediate temperature proton conductivity, we derived a relationship in order to determine the average membrane temperature based off of the resistance. We then applied this to experiments by using high frequency impedance spectroscopy measurements at various overpotentials. Transient plane source measurements were performed in order to determine the thermal conductivity of solid acid fuel cell components. These were subsequently used in to generate a 1-D model for heat conduction in an operational solid acid fuel cell at 250°C. In order to increase the thermal conductivity of the cell membrane, β-silicon carbide whiskers were selected for use in composites, due to a relatively high thermal conductivity of 120 $Wm^{-1}K^{-1}$. Composites of 10% SiC by volume increased the thermal conductivity by 221% while maintaining 77% of the proton conductivity. We expect further optimization can be achieved by development of a SiC mats and aqueous impregnation with CDP. These advancements could also enable drastically decreased membrane thickness allowing for a lower

ohmic resistance. This would greatly increase the electrochemical hydrogen separation efficiency considering that the ohmic losses are 80% of the voltage loss in the system.

REFERENCES

1. C. Perkins and A. W. Weimer, *Int. J. Hydrogen Energy*, **29**, 1587–1599 (2004).

2. J. Sedlak, J. Austin, and a Laconti, *Int. J. Hydrogen Energy*, **6**, 45–51 (1981).

3. K. Zeng and D. Zhang, *Prog. Energy Combust. Sci.*, **36**, 307–326 (2010) http://dx.doi.org/10.1016/j.pecs.2009.11.002.

4. A. Brisse, J. Schefold, and M. Zahid, *Int. J. Hydrogen Energy*, **33**, 5375–5382 (2008) http://dx.doi.org/10.1016/j.ijhydene.2008.07.120.

5. M. Carmo, D. L. Fritz, J. Mergel, and D. Stolten, *Int. J. Hydrogen Energy*, **38**, 4901–4934 (2013).

6. H. Takenaka, E. Torikai, Y. Kawami, and N. Wakabayashi, *Int. J. Hydrogen Energy*, **7**, 397–403 (1982).

7. S. Z. Baykara, *Int. J. Hydrogen Energy*, **29**, 1459–1469 (2004).

8. D. J. Edlund and W. A. Pledger, *J. Memb. Sci.*, **77**, 255–264 (1993).

9. a Adesina, *Int. J. Hydrogen Energy*, **20**, 777–783 (1995).

10. W. S. Harvey, J. H. Davidson, and E. A. Fletcher, *Ind. Eng. Chem. Res.*, **37**, 2323–2332 (1998) http://dx.doi.org/10.1021/ie980056q.

11. U. B. Demirci, S. Bernard, R. Chiriac, F. Toche, and P. Miele, *J. Power Sources*, **196**, 279–286 (2011) http://dx.doi.org/10.1016/j.jpowsour.2010.06.031.

12. D. Wang, S. Czernik, D. Montane, M. Mann, and E. Chornet, *Abstr. Pap. Am. Chem. Soc.*, **36**, 1507–1518 (1997).

13. Y. Kalinci, A. Hepbasli, and I. Dincer, *Int. J. Hydrogen Energy*, **34**, 8799–8817 (2009) http://dx.doi.org/10.1016/j.ijhydene.2009.08.078.

14. M. Ni, D. Y. C. Leung, M. K. H. Leung, and K. Sumathy, *Fuel Process. Technol.*, **87**, 461–472 (2006).

15. G. W. Crabtree, M. S. Dresselhaus, and M. V Buchanan, *Phys. Today*, 39–45 (2004).

16. Q. Wang, X. Chen, A. N. Jha, and H. Rogers, *Renew. Sustain. Energy Rev.*, **30**, 1–28 (2014) http://dx.doi.org/10.1016/j.rser.2013.08.065.

17. N. W. Ockwig and T. M. Nenoff, **107**, 4078–4110 (2007).

18. S. Sircar and T. C. Golden, *Sep. Sci. Technol.*, **35**, 667–687 (2000).

19. X. L. Pan, G. X. Xiong, S. S. Sheng, N. Stroh, and H. Brunner, *Chem.*

Commun., 2536–2537 (2001).

20. Y. H. Ma, E. E. Engwall, and I. P. Mardilovich, *ACS Div. Fuel Chem. Prepr.*, **48**, 333–334 (2003).

21. H. Amandusson, L. G. Ekedahl, and H. Dannetun, *J. Memb. Sci.*, **193**, 35–47 (2001).

22. H. Li, A. Goldbach, W. Li, and H. Xu, *J. Memb. Sci.*, **299**, 130–137 (2007).

23. H. K. Lee, H. Y. Choi, K. H. Choi, J. H. Park, and T. H. Lee, *J. Power Sources*, **132**, 92–98 (2004) http://www.sciencedirect.com/science/article/pii/S0378775304001247.

24. S. J. Kim et al., *Int. J. Hydrogen Energy*, **38**, 14816–14823 (2013) http://linkinghub.elsevier.com/retrieve/pii/S0360319913021897.

25. K. a. Perry, G. a. Eisman, and B. C. Benicewicz, *J. Power Sources*, **177**, 478–484 (2008).

26. K. D. Kreuer, *Annu. Rev. Mater. Res.*, **33**, 333–359 (2003) http://www.annualreviews.org/doi/abs/10.1146/annurev.matsci.33.022802.091825.

27. W. Vogel, L. Lundquist, P. Ross, and P. Stonehart, *Electrochim. Acta*, **20**, 79–93 (1975) http://www.sciencedirect.com/science/article/pii/0013468675850481.

28. H. Igarashi, T. Fujino, Y. Zhu, H. Uchida, and M. Watanabe, *Phys. Chem. Chem. Phys.*, **3**, 306–314 (2001).

29. T. E. Springer, T. Rockward, Zawodzinski T. A., and S. Gottesfeld, *J. Electrochem. Soc.*, **148**, A11–A23 (2001).

30. Q. Li, R. He, J.-A. Gao, J. O. Jensen, and N. J. Bjerrum, *J. Electrochem. Soc.*, **150**, A1599 (2003).

31. R. Chein, C. YC, Y. Lin, and H. JN, *Int. J. energy Res.*, **31**, 135–147 (2007).

32. Á. Mastalir et al., *Catal. Commun.*, **8**, 1684–1690 (2007).

33. S. M. Haile, C. R. I. Chisholm, K. Sasaki, D. a Boysen, and T. Uda, *Faraday Discuss.*, **134**, 17–39; discussion 103–118, 415–419 (2007).

34. Y. Taninouchi, T. Uda, Y. Awakura, A. Ikeda, and S. M. Haile, *J. Mater. Chem.*, **17**, 3182 (2007).

35. A. Ikeda and S. M. Haile, *Solid State Ionics*, **213**, 63–71 (2012) http://dx.doi.org/10.1016/j.ssi.2011.09.018.

36. A. B. Papandrew, R. W. Atkinson III, R. R. Unocic, and T. a. Zawodzinski, *J. Mater. Chem. A*, **3**, 3984–3987 (2015) http://xlink.rsc.org/?DOI=C4TA06451H.

37. T. Uda, D. a. Boysen, C. R. I. Chisholm, and S. M. Haile, *Electrochem. Solid-State Lett.*, **9**, A261 (2006) http://esl.ecsdl.org/cgi/doi/10.1149/1.2188069.

38. A. B. Papandrew et al., *J. Electrochem. Soc.*, **161**, F679–F685 (2014) http://jes.ecsdl.org/cgi/doi/10.1149/2.078405jes.

39. A. B. Papandrew and T. a. Zawodzinski, *J. Power Sources*, **245**, 171–184 (2014) http://linkinghub.elsevier.com/retrieve/pii/S0378775313011488.

40. M. Womes et al., *Appl. Catal. A Gen.*, **283**, 9–22 (2005) http://linkinghub.elsevier.com/retrieve/pii/S0926860X04010166.

41. C. Mercado-Zúñiga et al., *J. Alloys Compd.*, **615**, S538–S541 (2015) http://dx.doi.org/10.1016/j.jallcom.2014.02.106.

42. J. Arndt et al., *J. Phys. IV* (1995).

43. S. Saita and S. Maenosono, *Society*, 3705–3710 (2005).

44. I. K. Igumenov et al., *Desalination*, **136**, 273–280 (2001).

45. M. J. Rand, *Electrochem. Soc.*, **120**, 686–693 (1973).

46. A. B. Papandrew, C. R. I. Chisholm, R. a. Elgammal, M. M. Özer, and S. K. Zecevic, *Chem. Mater.*, **23**, 1659–1667 (2011).

47. G. A. Battiston, R. Gerbasi, and A. Rodriguez, *Chem. Vap. Depos.*, **11**, 130–135 (2005).

48. S. Barison et al., *Thin Solid Films*, **405**, 81–86 (2002).

49. A. B. Papandrew, C. R. I. Chisholm, S. K. Zecevic, G. M. Veith, and T. A. Zawodzinski, *J. Electrochem. Soc.*, **160**, 175–182 (2013).

50. R. Vargas, T. Goto, W. Zhang, and T. Hirai, *Appl. Phys. Lett.*, **65**, 1094–1096 (1994).

51. P. Sivakumar and V. Tricoli, *Electrochim. Acta*, **51**, 1235–1243 (2006).

52. A. B. Papandrew et al., *J. Electrochem. Soc.*, **160**, F848–F852 (2013) http://jes.ecsdl.org/content/160/8/F848\nhttp://jes.ecsdl.org/content/160/8/F848.fu

ll.pdf.

53. R. W. Atkinson et al., *ACS Appl. Mater. Interfaces*, **7**, 10115–10124 (2015) http://dx.doi.org/10.1021/am508228b.

54. R. W. Atkinson et al., *ACS Catal.*, **5**, 5154–5163 (2015).

55. S. St. John et al., *Chem. Commun.*, **51**, 16633–16636 (2015) http://dx.doi.org/10.1039/C5CC05706J.

56. S. St. John et al., *ACS Catal.*, **5**, 7015–7023 (2015).

57. A. B. Papandrew et al., *J. Electrochem. Soc.* , **163** , F464–F469 (2016) http://jes.ecsdl.org/content/163/6/F464.abstract.

58. C. R. I. Chisholm, D. A. Boysen, A. B. Papandrew, S. Zecevic, and S. Cha, 53–59.

59. W. Sheng, H. A. Gasteiger, and Y. Shao-Horn, *J. Electrochem. Soc.*, **157**, B1529 (2010).

60. J. Durst et al., *Energy Environ. Sci.*, **7**, 2255–2260 (2014) http://xlink.rsc.org/?DOI=c4ee00440j.

61. W. Sheng et al., *Nat. Commun.*, **6**, 5848 (2015) http://www.nature.com/ncomms/2015/150108/ncomms6848/abs/ncomms6848.html.

62. J. Durst, C. Simon, F. Hasche, and H. a. Gasteiger, *J. Electrochem. Soc.*, **162**, F190–F203 (2014) http://jes.ecsdl.org/cgi/doi/10.1149/2.0981501jes.

63. H. A. Gasteiger, N. M. Markovic, and P. N. Ross Jr., *J. Phys. Chem.*, **99**, 8290–8301 (1995).

64. S. Trasatti, *J. Electroanal. Chem.*, **39**, 163–184 (1972).

65. a. B. Papandrew et al., *J. Electrochem. Soc.*, **161**, F679–F685 (2014) http://jes.ecsdl.org/cgi/doi/10.1149/2.078405jes.

66. A. B. Papandrew et al., *J. Power Sources*, **337**, 145–151 (2017) http://dx.doi.org/10.1016/j.jpowsour.2016.10.093.

67. a. B. Papandrew et al., *J. Electrochem. Soc.*, **161**, F679–F685 (2014) http://jes.ecsdl.org/cgi/doi/10.1149/2.078405jes.

68. R. W. Atkinson et al., *ACS Appl. Mater. Interfaces*, 150423103811008 (2015)

http://pubs.acs.org/doi/abs/10.1021/am508228b.

69. B. N. Grgur, N. M. Marković, and P. N. Ross, *Can. J. Chem.*, **75**, 1465–1471 (1997) http://www.nrcresearchpress.com/doi/abs/10.1139/v97-176.

70. R. Of, T. H. E. Rate, and O. F. Transformation, **2**, 1–5 (1997).

71. K. Seto, A. Iannelli, B. Love, and J. Lipkowski, *J. Electroanal. Chem.*, **226**, 351–360 (1987).

72. S. Chen and A. Kucernak, *J. Phys. Chem. B*, **108**, 3262–3276 (2004) http://dx.doi.org/10.1021/jp036831j.

73. J. X. Wang, S. R. Brankovic, Y. Zhu, J. C. Hanson, and R. R. Adžić, *J. Electrochem. Soc.*, **150**, A1108 (2003).

74. E. Antolini, *Energy Environ. Sci.*, **2**, 915 (2009) http://xlink.rsc.org/?DOI=b820837a.

75. M. Shao, *J. Power Sources*, **196**, 2433–2444 (2011) http://dx.doi.org/10.1016/j.jpowsour.2010.10.093.

76. A. T. Kuhn and P. M. Wright, *J. Electroanal. Chem.*, **27**, 319–323 (1970).

77. E. Skulason et al., *J. Phys. Chem. C*, **114**, 18182–18197 (2010) <Go to ISI>://WOS:000285236800067.

78. J. O. Bockris and S. Srinivasan, *Electrochim. Acta*, **9**, 31–44 (1964) http://dx.doi.org/10.1016/0013-4686(64)80003-7\nhttp://linkinghub.elsevier.com/retrieve/pii/0013468664800037.

79. N. Pentland, J. O. Bockris, and E. Sheldon, *J. Electrochem. Soc.*, **104**, 182 (1957) http://jes.ecsdl.org/cgi/doi/10.1149/1.2428530.

80. A. K. M. S. Huq and A. J. Rosenberg, *J. Electrochem. Soc.*, **111**, 270–278 (1964).

81. A. Iulianelli, P. Ribeirinha, A. Mendes, and A. Basile, *Renew. Sustain. Energy Rev.*, **29**, 355–368 (2014).

82. J. Agrell, H. Birgersson, and M. Boutonnet, *J. Power Sources*, **106**, 249–257 (2002) http://www.sciencedirect.com/science/article/pii/S0378775301010278.

83. M. Turco et al., *Appl. Catal. B Environ.*, **77**, 46–57 (2007).

84. M. Khzouz, J. Wood, B. Pollet, and W. Bujalski, *Int. J. Hydrogen Energy*, **38**,

1664–1675 (2013) http://linkinghub.elsevier.com/retrieve/pii/S0360319912016035.

85. T. Conant et al., *J. Catal.*, **257**, 64–70 (2008).

86. M. D. Foster, *Wabash River Coal Gasification Repowering Project*, p. 1-42, (2002) http://www.scopus.com/inward/record.url?eid=2-s2.0-0028014870&partnerID=40&md5=1f24d7ba686bac63bf6158ad7fc2a954.

87. T. Utaka, K. Sekizawa, and K. Eguchi, *Appl. Catal. A Gen.*, **194**, 21–26 (2000).

88. T. Utaka, T. Okanishi, T. Takeguchi, R. Kikuchi, and K. Eguchi, *Appl. Catal. A Gen.*, **245**, 343–351 (2003).

89. B. L. Gustafson and J. H. Lunsford, *J. Catal.*, **74**, 393–404 (1982).

90. R. L. Keiski, O. Desponds, Y. F. Chang, and G. A. Somorjai, *Appl. Catal. A, Gen.*, **101**, 317–338 (1993).

91. H. Uchida, K. Izumi, K. Aoki, and M. Watanabe, *Phys. Chem. Chem. Phys.*, **11**, 1771–1779 (2009).

92. K. C. Neyerlin, W. Gu, J. Jorne, and H. A. Gasteiger, *J. Electrochem. Soc.*, **154**, B631 (2007).

93. E. S. Steigerwalt, G. A. Deluga, and C. M. Lukehart, 760–766 (2002).

94. F. Richarz, B. Wohlmann, U. Vogel, H. Hoffschulz, and K. Wandelt, *Surf. Sci.*, **335**, 361–371 (1995).

95. B. D. McNicol and R. T. Short, *J. Electroanal. Chem.*, **81**, 249–260 (1977).

96. W. F. Lin, T. Iwasita, and W. Vielstich, *J. Phys. Chem. B*, **103**, 3250–3257 (1999) http://pubs.acs.org/doi/abs/10.1021/jp984491+.

97. M. Watanabe and S. Motoo, *J. Electroanal. Chem. Interfacial Electrochem.*, **60**, 275–283 (1975) http://www.sciencedirect.com/science/article/pii/S0022072875802622.

98. Y. Ishikawa, M. S. Liao, and C. R. Cabrera, *Surf. Sci.*, **463**, 66–80 (2000).

99. N. M. Markovic and P. N. Ross Jr., *Surf. Sci. Rep.*, **45**, 117–229 (2002).

100. E. V. Spinacé, A. O. Neto, and M. Linardi, *J. Power Sources*, **129**, 121–126 (2004).

101. B. Smith and R. White, *A.I.Chem.E*, 46–54 (1956).

102. S. E. Ziemniak and M. Hanson, *Corros. Sci.*, **44**, 2209–2230 (2002) http://www.sciencedirect.com/science/article/pii/S0010938X02000045.

103. A. G. Nasibulin, A. Moisala, D. P. Brown, and E. I. Kauppinen, *Carbon N. Y.*, **41**, 2711–2724 (2003).

104. A. Lahiri, R. Das, and R. G. Reddy, *J. Power Sources*, **195**, 1688–1690 (2010).

105. a. S. Bolokang and M. J. Phasha, *Mater. Lett.*, **65**, 59–60 (2011) http://dx.doi.org/10.1016/j.matlet.2010.09.045.

106. A. Lahiri and Z. Tadisina, *Mater. Chem. Phys.*, **124**, 41–43 (2010) http://dx.doi.org/10.1016/j.matchemphys.2010.07.019.

107. N. Bahlawane et al., *Chem. Mater.*, **22**, 92–100 (2010).

108. A. B. Papandrew et al., *J. Power Sources*, **337**, 145–151 (2017).

109. R. S. Ginder and G. M. Pharr, *Scr. Mater.*, **139**, 119–121 (2017) http://www.sciencedirect.com/science/article/pii/S1359646217303329?dgcid=raven_sd_via_email.

VITA

David L. Wilson III grew up in Strawberry Plains, Tennessee. He enrolled at the University of Tennessee in Knoxville, Tennessee in 2007. As an undergraduate student, David conducted research with Dr. Zawodzinski before graduating with a Bachelor's degree in Chemical and Biomolecular Engineering in 2012. That year David joined the Department of Chemical and Biomolecular Engineering at the University of Tennessee, Knoxville as a graduate student working in Dr. Zawodzinski's research group in pursuit of his PhD.